HZG REPORT 2015-2 // ISSN 2191-7833

# Region of interest synchrotron nanotomography and nanodiffraction with FIB/SEM characterisation on engineering materials

(Vom Department Physik der Universität Hamburg als Dissertation angenommene Arbeit)

D. Laipple

wissen
schafft
nutzen

Helmholtz-Zentrum
Geesthacht
Zentrum für Material- und Küstenforschung

# Region of interest synchrotron nanotomography and nanodiffraction with FIB/SEM characterisation on engineering materials

(Vom Department Physik der Universität Hamburg als Dissertation angenommene Arbeit)

D. Laipple

Helmholtz-Zentrum Geesthacht
Zentrum für Material- und Küstenforschung GmbH | Geesthacht | 2015

Die HZG Reporte werden kostenlos abgegeben.
HZG Reports are available free of charge.

Anforderungen/Requests:

Helmholtz-Zentrum Geesthacht
Zentrum für Material- und Küstenforschung GmbH
Bibliothek/Library
Max-Planck-Straße 1
21502 Geesthacht
Germany
Tel.: +49 4152 87-1690
Fax.: +49 4152 87-1717
E-Mail: bibliothek@hzg.de

*Druck: HZG-Hausdruckerei*

Als Manuskript vervielfältigt.


ISSN 2191-7833

Helmholtz-Zentrum Geesthacht
Zentrum für Material- und Küstenforschung GmbH
Max-Planck-Straße 1
21502 Geesthacht

www.hzg.de

HZG REPORT 2015-2

# Region of interest synchrotron nanotomography and nanodiffraction with FIB/SEM characterisation on engineering materials

*(Vom Department Physik der Universität Hamburg als Dissertation angenommene Arbeit)*

Daniel Laipple

*169 pages with 80 figures and 5 tables*

Abstract

The new Beam Lines of the Helmholtz-Zentrum Geesthacht (HZG, Germany) at the PETRA III storage ring at the Deutsche Elektronen Synchrotron (DESY, Hamburg, Germany) for imaging (IBL/P05) and nanofocus X-ray scattering (MiNaXS/P03 endstation) are providing non-destructive insight on the nm scale to most kinds of materials by synchrotron radiation using computed nanotomography (SRnCT) and nanofocus X-ray Scattering (NaXS) respectively. To obtain the high-resolution μm scaled samples are required, e.g. for the imaging beam line (IBL) of about 50μm. Therefore, in the present work a FIB based region of interest specimen processing method was developed matching primarily the requirements of IBL. It was complemented with SEM characterisation techniques using the *cross beam* device Auriga from *Zeiss* (Oberkochen, Germany). The Auriga stage holder had to be slightly modified to fit the IBL sample holders which can be used similarly at the MiNaXS endstation. Several sample types proposed for SRnCT were characterised by FIB/SEM and X-ray techniques during development and first application of this new sample preparation method. By laboratory-CT measurements of a sintered $Ti$-6$Al$-4$V$ alloy an ideal porosity for cell ingrowth of 30% was detected while surface and internal cell colonisation was confirmed by using SEM. Different FIB/SEM techniques were applied to study the corrosion of $Mg$ alloys developed as implant material for medical purposes. A homogeneous dispersion of $MgH_2$ and $LiBH_4$ inside of a carbon aerogel scaffold dedicated to hydrogen storage could be characterised by FIB/SEM cross sectioning. The phase composition of a spherical gas-atomised $Ti$-45$Al$-5 and 10$Nb$ powder alloy, which was produced by the PIGA technique at HZG, was determined by X-ray scattering at the HEMS side station (beamline P07b, PETRA III) as well as by successful 2D and FIB based 3D electron back scatter diffraction (EBSD) measurements. Different wood lamellae were precisely prepared with perpendicular orientation of the tracheids for the subsequent nanodiffraction at the MiNaXS endstation. Finally a FIB processed specimen pillar from a photonic glass sample composed of $ZrO_2$ spheres was investigated for the first time by SRnCT at IBL. Additionally a FIB tomography was performed of this specimen pillar. It was found that this technique is less reliable to arbitrary sample geometries compared to SRnCT while its resolution is definitely higher. In the future the techniques established within this work by combining FIB/SEM with SRnCT and NaXS will provide the basis for sample preparation and investigation on the nm scale for a wide range of materials.

# Bereichsselektive Synchrotron Nanotomographie und Nanodiffraktion mit FIB/SEM Charakterisierung von Werkstoffen

Zusammenfassung

Die neuen Synchrotron-Strahlungs-Messplätze des Helmholtz-Zentrums Geesthacht (HZG, Deutschland) am Speicherring der dritten Generation PETRA III des Deutschen Elektronen Synchrotrons (DESY, Hamburg, Deutschland) für Bildgebung (IBL/P05) und Nano-Röntgenstreuung (MiNaXS/P03 Endmessplatz) ermöglichen die zerstörungsfreie Untersuchung fast aller Materialien durch Synchrotron-Strahlung, unter Verwendung von Computer Nanotomographie (SRnCT) einerseits und nanofokaler Röntgenstreuung (NaXS) andererseits. Um dabei Hochauflösung im Nanometer-Bereich zu ermöglichen müssen die zu untersuchenden Proben in der Größenordnung von μm vorliegen, für den Bildgebungs-Messplatz IBL ist beispielsweise eine Probengröße von 50μm erforderlich.

Um insbesondere die Vorgaben des IBL Messplatzes zu erfüllen wurde in dieser Arbeit mit der Auriga *cross beam* Anlage von *Zeiss* (Oberkochen, Deutschland) eine Ionenfeinstrahlanlage (FIB) basierte probenbereichsselektive Herstellungsmethode entwickelt und mit Analysetechniken der Rasterelektronenmikroskopie (SEM) komplementiert. Um die Adaption der IBL Probenhalter zu ermöglichen, welche gleichermaßen am MiNaXS Endmessplatz verwendet werden können, wurde der Auriga Probenhalter leicht modifiziert. Diverse Probenkategorien für SRnCT wurden bei der Methodenentwicklung und ersten Anwendungen der Kombination dieser Probenpräparationsmethode mit der FIB/SEM Einheit und den Röntgentechniken untersucht. Durch Messungen mit einem Labor-Computertomographen an einer gesinterten $Ti$-6$Al$-4$V$ Legierung konnte eine für Zelleinwachstum ideale Porosität von 30% festgestellt werden, während mittels SEM oberflächliche und interne Zellpopulationen nachgewiesen werden konnten. Verschiedene FIB/SEM Untersuchungen bezüglich der Korrosion von $Mg$ Legierungen, die für den Einsatz als Biomaterialien für medizinische Zwecke entwickelt wurden, wurden durchgeführt. Eine homogene Verteilung von $MgH_2$ und $LiBH_4$ in einem Kohlenstoff-Aerogel-Gerüst für Wasserstoffspeicher konnte mit FIB/SEM Querschnitten bestimmt werden. Die Phasenzusammensetzung einer sphärisch pulververdüsten $Ti$-45$Al$-5 and 10$Nb$ Legierung, die mit der PIGA Technik im HZG produziert wurde, konnte durch Röntgendiffraktion an der HEMS-Seitenstation (P07b, PETRA III) genauso wie durch 2D und FIB basierte 3D Elektronenrückstreudiffraktion (EBSD) Messungen bestimmt werden. Mehrere Holzlamellen konnten mit rechtwinkliger Ausrichtung der Tracheiden präzise für die nachfolgende nanofokale Diffraktion an dem MiNaXS Endmessplatz präpariert werden. Letztendlich konnte ein mit FIB hergestellter Probenzylinder aus einer Photonischen-Glas-Probe, welche aus $ZrO_2$ Kugeln besteht, erstmals mit SRnCT an IBL untersucht werden. Hiernach wurde eine FIB Tomographie an diesem Probenzylinder durchgeführt. Dabei zeigte sich, dass diese Methode für beliebige Probengeometrien weniger verlässlich ist als SRnCT. In Zukunft bereiten die in dieser Arbeit durch Kombination von FIB/SEM mit SRnCT und NaXS entwickelten Techniken die Basis für Probenpräperation und Untersuchungen im nm Bereich vieler verschiedener Materialklassen.

*Manuscript received / Manuskripteingang in Druckerei: 23. Juni 2015*

# Contents

# List of acronyms and symbols

| | |
|---|---|
| BSD | back scattered electrons detector |
| CBP | convoluted back projection |
| CRL | compound refractive lens |
| CT | computed tomography |
| DCM | double crystal monochromator |
| EBSD | electron back scatter diffraction |
| EDX | energy dispersive x-ray spectroscopy |
| EsB | energy selective back scatter detector (in lens position, Auriga) |
| FBP | filtered back projection |
| FIB | focused ion beam |
| GIS | gas injection system (Auriga) |
| IBL | imaging beamline P05 at PETRA III |
| InLens | secondary electrons detector at in lens position (Auriga) |
| LMIS | liquid metal ion source |
| MIM | metal injection moulding |
| MiNaXS | micro- and nanofocus X-ray scattering (beam line) P03 at PETRA III |
| NaXS | nanofocus X-ray scattering |
| POPE | 1-palmitoyl-2-oleoyl-sn-glycero-3-phosphoethanolamine |
| RMS | root mean square |
| Saos-2 | sarcoma osteogenic, a non-transformed cell line derived from primary osteosarcoma |
| PE | primary electrons coming from the SEM gun |
| SE, BSE | secondary electrons, back scattered electrons |
| SEM | scanning electron microscopy |
| SE2 | secondary electrons (Auriga) |
| STEM | scanning transmission electron microscopy |
| SR$\mu$CT | synchrotron radiation based computed microtomography |
| SRnCT | synchrotron radiation based computed nanotomography |
| TEM | transmission electron microscopy |
| UHV | ultra high vacuum |
| WD | working distance |

| | |
|---|---|
| $Au, C, P...$ | element symbols |
| $d\sigma, d\Omega$ | cross section and opening angle of elastic scattering |
| $e$ | elemental charge |
| $f(x, y, )$ | representation of the tomographic slice, in our case also $\mu$(x,y) |
| $F(u, v)$ | two dimensional Fourier transform of $f(x, y)$ |
| $I, I_0$ | quantitative attenuation |
| $m_e c^2$ | rest energy of the electron |

| | |
|---|---|
| $\mu$ | attenuation coefficient |
| $p$ | projected attenuation |
| $P_\theta(w)$ | one dimensional Fourier transform of $p_\theta(t)$ |
| $\theta$ | deflection angle of scattered electrons by SEM |
| $t, z, \theta$ | horizontal, vertical coordinates and projection angle on the x-ray detector plane; $t$ is also used for stage tilt of the Auriga |
| $U_{EHT}$ | electronic high tension in [kV] |
| $x, y$ | coordinates on a tomographic slice; horizontal stage coordinates of the Auriga |

# Chapter 1

# Introduction

The development of modern innovative engineering materials and the progress in medicine makes the exploration of nano structures necessary determining the characteristic properties of the material. Computed tomography (CT) using X-rays is a suitable technique to achieve a non-destructive three-dimensional insight into most kinds of materials, devices and also living beings. This is the reason for the high availability of laboratory X-ray CT instruments. X-ray scattering (XS) or diffraction enables in a similar way statistical material composition and characteristics.
Starting as side product of particle accelerators, synchrotron-radiation is the most brilliant X-ray radiation in the world, providing fascinating new possibilities to all kinds of X-ray experiments.

Synchrotron-radiation based computed microtomography (SR$\mu$CT) was developed to achieve three-dimensional images of objects, resolving features with sizes of a few $\mu$m [14].
For improving the resolution of this technique additional X-ray optics are required. Since it is possible to achieve a resolution on the nm scale the method is named Synchrotron-radiation-based Computed nanotomography (SRnCT). Optical and geometric considerations demand a smaller sample size of about 50$\mu$m to obtain a high-resolution of down to 50 nm.
The Imaging Beam Line (IBL) P05 of the Helmholtz-Zentrum Geesthacht[1] (HZG) at the PETRA III[2] storage ring at DESY[3] was designed to provide a small beam with a high brilliance which is necessary for SR$\mu$CT and SRnCT experiments [52]. Tomographic investigations with a larger field of view can be performed with SR$\mu$CT, while SRnCT offers the possibility to perform tomography in a region of interest of a previously selected sample region, featuring highest resolution. Together with the beam lines 26-ID-C & 32-ID-C of the *Advanced Photon Source* (Argonne National Laboratory, Illinois, USA) [141; 108; 86], ID22 of the *European*

[1] former GKSS, renamed in October 2010
[2] Positron-Elektron-Tandem-Ring-Anlage providing 3$^{rd}$ generation synchrotron-radiation
[3] Deutsches Elektronen-Synchrotron

*Synchrotron Radiation Facility* (ESRF, Grenoble, France) [15; 12] and U41-TXM[4] of the *Berliner Elektronenspeicherring für Synchrotronstrahlung* (BESSY, Berlin, Germany) [115; 54], *IBL at Petra III* is one of the four facilities in the world providing SRnCT.
To prepare a small sample out of the material according to the requirements of SRnCT, the Focussed Ion Beam (FIB) technique, once developed in the field of semi-conductors industry, is most suited. The Auriga crossbeam workstation from *Zeiss* (Oberkochen, Germany) situated at HZG as a part of the German Engineering Materials Science Centre (GEMS) is designed for sample preparation for SRnCT and for additional analysis. It is providing both related techniques, scanning electron microscopy (SEM) and FIB. The Auriga is equipped with several different SEM detectors, enabling the imaging of the sample surface, energy dispersive X-ray spectroscopy and electron backscatter diffraction.

To perform the X-ray scattering technique at highest resolution a nanofocus X-ray beam is mandatory. This technique is then called nanodiffraction.
Regarding synchrotron X-ray scattering the endstations of the beam lines ID13 of the *European Synchrotron Radiation Facility* (ESRF, Grenoble, France) and of the Micro- and Nanofocus X-ray Scattering (MiNaXS) beam line (P03) of the HZG and the Kiel University at PETRA III (DESY) are providing this highly resolving technique.
Nanodiffraction requires the preparation of small specimen similar to SRnCT, in particular sample lamellae with some $\mu$m thickness.

The aim of this thesis is the method development from complementary preanalysis and sample processing that fits the criteria for X-ray nanotomography and nanodiffraction by selective FIB-milling around a region of interest to the characterisation of the 3D-nanostructure by performing first experiments at IBL and MiNaXS (P03) endstation (PETRA III, DESY).
The related thesis of M. Ogurreck [104] was created in parallel and deals with the construction of IBL from scratch. To accomplish first experiments was similarly the main target. IBL (P05) was still under construction until completion of this thesis, therefore not all experiments which were considered to be available in the future could be performed entirely.
During this work different samples with scientific questions were investigated and analysed by SEM and FIB techniques.
For highly resolving X-ray tomography a region of interest was selected to be cut out by FIB, and was processed to a $\mu$m ranged specimen. The final step is the three dimensional characterisation by SRnCT with an ideal resolution of below 100 nm.
In parallel, nanodiffraction at MiNaXS was accomplished by a slightly modified FIB/SEM sample processing procedure.

[4] providing full-field Transmission soft X-ray Microscopy (TXM), biological samples

# Chapter 2

# Instruments and methods: synchrotron experiments

In 1894 P. Lenard developed a gas discharge tube from which a cathode ray could penetrate through a 2,65 $\mu$m thick aluminium window [77]. Hardly one year later W. C. Röntgen detected the existence of the so far unknown electromagnetic radiation by experiments with this cathode rays. He named this radiation X-rays. Since then X-rays became essential in many fields of research as well as in medical treatment. Since the development of computers, tomography images can be calculated out of many radiographic projections, which are taken of one object from different angles. Today computed tomography is well known, especially from the widespread medical applications.

For this work not only classically generated X-rays by tubes emitting bremsstrahlung were used. Mainly X-rays emitted from a new generation source given by storage rings such as PETRA III[1] were utilised to perform highly resolving tomographic experiments on engineering materials.

## 2.1 Development of the storage rings

The first attempts to describe orbiting charges and its radiation were already done before the invention of Bohr's atom model, by the classical treatment of electromagnetic radiation by accelerated charged point sources [76; 83], and the attempts to model the atomic spectra by circular orbits [116]. The revival on this physical effect came when the first linear, circular and electrostatic particle accelerators were built in the end of the 1920s, motivated by a strong connection to the evolution of nuclear physics. After World War II, step by step higher acceleration energies could be realised, enabled by new technical achievements like the synchro-cyclotron and finally superconductive magnets, HF-resonators

[1] Positron-Elektron-Tandem-Ring-Anlage at the Deutsches Elektronen-Synchrotron (DESY), Germany

as well as computer-controlling and computer based calculating of accelerator devices.

To gain the whole accessible energy for the collision of particles in their centre of mass system, storage rings or colliders were developed, in which particle bunches contrarily circulate and collide in special interaction points. With establishing the (LEP)[2] at CERN[3] the so far biggest storage ring was built with a circumference of 27 km, dedicated to prove the existence of the Higgs-Boson [58].
For more details on the history of accelerators, a review can be e.g. found in [59].

## 2.2 X-ray generation by synchrotrons

In synchrotrons charged particles, e.g. electrons, are accelerated almost to the speed of light by an high-frequent electromagnetic field which is synchronised to the acceleration trajectory of the particles. These particles are stabilised in bunches by strong magnetic fields in a tube system in ultra-high vacuum (UHV). Even though the name *synchrotron* is derived by the *synchro-cyclotron*, it is now used for all kind of particle accelerators or storage rings.

Due to lower costs and feasibility reasons, these synchrotrons were normally constructed in ring and not linear shape, with large radius of curvature, i.e. quantum effects are negligible. To make the charged particle bunches orbiting, deflecting magnetic fields, so called bending magnets, are used. Hence, this bunches are permanently accelerated perpendicular to their flight direction, and as any charged particles forced to loose energy by emitting electromagnetic radiation. Because of this significant energy loss the achievable energy is limited in circular synchrotrons [66]. The power of this so called *synchrotron radiation* per particle with elementary charge e is

$$P \simeq \frac{2e^2c}{3\rho^2} \cdot \beta^4 \cdot \gamma^4, \qquad \text{while} \quad \rho = 3,34 \frac{E[GeV]}{B[T]} \tag{2.1}$$

is the orbit radius. Further the relativistic dilatation factor $\gamma = 1/\sqrt{1-\beta^2}$ and the velocity of the particle is used with respect to the speed of light $\beta = v/c$ [112]. Obviously the loss of energy is negligible for proton synchrotron accelerators, due to their much higher mass to charge ratio compared to electrons or positrons.

This energy loss, a disadvantage to the particle physicists, found usage by material and fundamental researchers of any kind, due to the unique properties of the emitted synchrotron radiation. The wavelength $\lambda$ of this radiation has a range of $10^3$ to $< 10^{-1}$ Å. This is similar to chemical bond lengths, and the associated photon energies are similar to the binding energies of core and valence electrons, as shown in Figure 2.1. The wavelength and the energy $E$ are connected via the

[2]Large Electron-Positron Collider
[3]Conseil Européen pour la Recherche Nucléaire, Switzerland

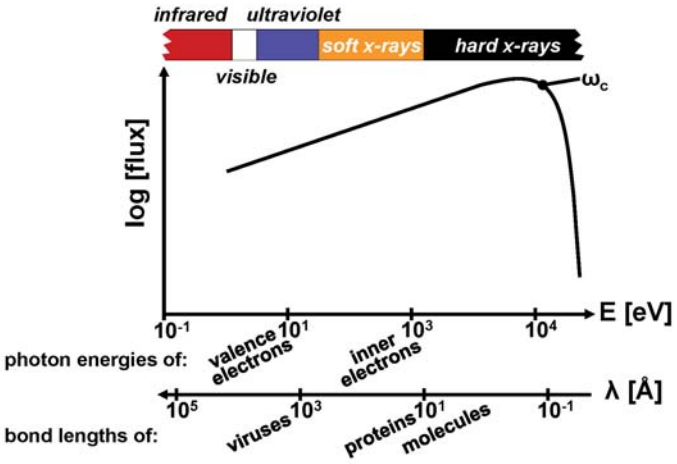


**Figure 2.1:** Distribution of photon density by synchrotron radiation compared to energies and distances on molecular level [87]; the characterising average frequency is $\omega_c$.

de Broglie wavelength of a particle with rest mass zero as $\lambda = h \cdot c/E$, where $h$ is Planck's constant.

The average or critical frequency $\omega_c$ of a charged particle passing a curvature (marked in Figure 2.1) is defined by

$$\omega_c = \frac{3c\gamma^3}{2R}, \tag{2.2}$$

whereat $\gamma$ is again the relativistic dilatation factor, $c$ the speed of light and $R$ the radius of curvature [137]. $\omega_c$ characterises the radiation by the variables of the synchrotron experiment $v$ and $R$.

In its system the accelerated particle emits radiation as usual, but due to the relativistic speed it appears in our system that the synchrotron radiation is directed in flight direction of the particle. This is causal for the typical alignment of the experimental hutches of synchrotron beam lines, linked to storage rings in tangential direction.

For relativistic reasons, the angle between a photon, emitted perpendicular to the flight direction of a charged particle, and the flight direction itself[4] is given by

$$\Theta_{(rad)} \approx \frac{1}{\gamma}. \tag{2.3}$$

For an electron with an energy of 2 GeV, i.e. $\gamma = 3914$, the opening angle of the radiation cone is $2\Theta_{(rad)} = 0,5mrad \approx 0,03°$. The wide spectra, which also can be adapted to the requirements of the experiment, the high intensity and the strongly forwarded emission makes the synchrotron radiation a very powerful tool to all

[4] i.e. the maximum deviation of the photon from the flight direction.

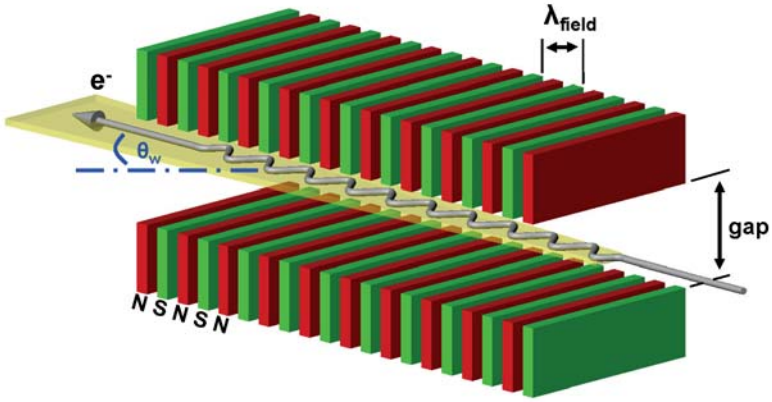


**Figure 2.2:** Schematic operating principle of wigglers and undulators: the $e^-$ wiggles along the orbit due to the periodic magnetic forces. The maximum deviation of the orbit is given by $\theta_w$ and is tunable by the gap distance. The x-ray photons are emitted in a narrow light cone (Equation 2.3).

kinds of applied research. Though so far the synchrotron radiation flash of a particle bunch passing a bending magnet is quite short timed, and its energy is distributed over the whole curvature.

By installing periodic magnetic structures called wigglers or undulators, which makes the electron 'wiggle' on its trajectory, the radiation flux is increased for the specific place of the experiment, since the radiation is not emitted on a curvature of the orbit but on many swings around it (Figure 2.2). Passing such a device the maximum angular deviation $\Theta_w$ between the electron orbit and its flight direction during this oscillation is

$$\Theta_w = \frac{1}{\gamma} \cdot K \qquad \text{with} \quad K = \frac{\lambda_{field} B_{max} e}{2\pi m_e c}, \tag{2.4}$$

with $\lambda_{field}$ is the period of the magnet array and $B_{max}$ is the amplitude of the magnetic field. Now one can distinct between wigglers and undulators by $K$: For an instrument with $K \leq 1$ it is named undulator, and for $K > 1$ it is named wiggler. The bending in undulators is weak and the emission happens quasi parallel, therefore the radiation is mainly monochromatic. The brightness follows the square of the number of undulator periods due to this coherent interaction. The undulator gap can be adjusted to gain desired photon wavelengths and energy.

Wigglers on the contrary emit a broad and very intense spectrum, like bending magnets do. The flux of a wiggler is commonly about $10^3$ magnitudes higher than that one of a X-ray tube! Needless to say that there are no characteristic peaks in the spectrum like the fluorescence lines of an X-ray tube anode overlapping the bremsstrahlung.

To provide a synchrotron X-ray experiment one energy band is selected by single


**(a)** Bragg reflection

**(b)** Monochromator in Bragg geometry

**Figure 2.3:** (a) Parameters of Bragg's law: $d$ is the interplanar distance, $\theta_B$ the diffraction angle and $\lambda$ the photon wavelength. (b) Si(111) DCM in Bragg geometry, selecting one wavelength.

crystals in Bragg or Laue geometry. The formula of Bragg's law is, regarding the content, equivalent to the Laue condition. Bragg's law

$$2dsin\theta_B = n\lambda \tag{2.5}$$

describes constructive interference of elastic scattered radiation on families of lattice planes in a crystal, while $d$ is the interplanar distance, $\lambda < d$ and $n$ is integer (Figure 2.3a). For one specific $\lambda$ only the first order $n = 1$ and higher chromatic wavelengths $n > 1$ fit to the condition, so a mainly monochromatic beam is obtained. For a parallel passing and a secondary monochromatisation of the X-ray beam, commonly two of these monochromator crystals are arranged in Bragg geometry (Figure 2.3b), and are located in the optics hutch at the very beginning part of a beamline. By changing the reflection angle of this double crystal monochromators (DCM) the energy of the resulting monochromatic beam is adjusted.

### 2.2.1 Petra III of DESY

Although synchrotrons were once established to boost particle energies and perform experiments in particle physics, e.g. to discover new particles which are predicted by the theory of the standard model, many of them are now designed to produce merely synchrotron radiation. The storage ring PETRA[5] was built between 1975 and 1978 for high energy physics collision experiments at DESY[6] in Hamburg. The particle of the strong interaction, the gluon, was detected at PETRA in 1979 [31]. From 1987 until July 2007 it was used as pre-accelerator for HERA[7] named by the acronym PETRA II. Since then approximately one eighth of the storage ring was completely refurbished by installing 14 beamlines, to start in November 2009 as PETRA III, which is the most brilliant light source in the world. Brilliance, being a degree of quality for X-rays, is defined by

[5]Positron-Elektron-Tandem-Ring-Anlage
[6]Deutsches Elektronen-Synchrotron
[7]Hadron-Elektron-Ring-Anlage

$$B = \frac{N/t}{d\Omega \cdot dF \cdot (d\lambda/\lambda)} \tag{2.6}$$

with $N/t$, the number of emitted photons passing in the time of $t$, in relation to the area of the source $dF$, the solid angle $d\Omega$, in which the radiation is emitted, and the relative wavelength bandwidth $d\lambda/\lambda$. In common, synchrotron sources have a $\sim 10^{12}$ times higher Brilliance than X-ray tubes [9]. For $3^{rd}$ generation synchrotron sources the Brilliance is again significantly increased. The photon flux on one $mm^2$ of the $3^{rd}$ generation source PETRA III is the same as at the $2^{nd}$ generation source DORIS III[8] on some $cm^2$.

To date PETRA III is using electrons, starting their acceleration with 450 MeV by passing a linear pre-accelerator. Afterwards the electron beam is bunched by an intensity accumulator, that is affecting the electrons with a high frequent field. Now these bunches are inserted to the DESY ring, which is the only real synchrotron left on this compound, and are accelerated to their final energy of 6 GeV. Subsequently they are transferred to the 2304 m long PETRA ring to constitute a 100 mA strong electron current. To compensate the loss of energy by the synchrotron radiation at every turn on the orbit, as well as by the insertion devices, radio frequent cavities are applied to boost the electron's energy.

Due to the fact that focussing optics generate always some kind of source image, the electron beam source size and the synchrotron beam divergence should be as small as possible to provide a nanofocused X-ray beam at the experiment. The quality of the created nanofocused beam is limited by the source and the horizontal and vertical emittance:

$$\epsilon_x = \sigma_x \cdot \sigma_{x'} \quad \epsilon_y = \sigma_y \cdot \sigma_{y'}$$

using the horizontal source size $\sigma_x$, its vertical pendant $\sigma_y$ and the source divergence $\sigma_{x'}$ and $\sigma_{y'}$ respectively. The source parameters of PETRA III at IBL using the standard undulator are presented in Table 2.1.

| | |
|---|---|
| horizontal source size [RMS][9] | 37 $\mu$m |
| horizontal divergence [RMS] | 27 $\mu$rad |
| vertical source size [RMS] | 5.7 $\mu$m |
| vertical divergence [RMS] | 5.4 $\mu$rad |
| horizontal emittance x | 1 nmrad |
| vertical emittance y | 0.01 nmrad |

**Table 2.1:** Source parameters of the PETRA III storage ring for a 2m undulator in low emittance -$\beta$ mode as applied at IBL [18].

[8]DORIS (acronym for Doppel-Ring Speicher) was the first storage ring at DESY, and is thus the older and smaller sister of PETRA, who also started as high energy physics experiment storage ring in 1974 and served since 1993 as synchrotron radiation source til its shut down in January 2013.

## 2.3 Synchrotron-radiation-based computed tomography

The word *tomography* is composed out of the Greek words *tome*(cut) or *tomos*(part or section) and *graphein*(write). Computed tomography (CT) means inspecting an object in order to obtain a three dimensional image of it, including the internal structure. This is done by taking a series of one or two dimensional radiographic projection images of the object from several directions by a detector camera around a single axis of rotation. In case of one dimensional projection only one detector row would be computed for reconstruction of an object's slice, in the two dimensional case this has to be done for any detector or pixel row respectively. Thereby, in the two dimensional case, one gains a stack of two dimensional reconstruction slices of the object in parallel, and thus a three dimensional image in terms of a pack of slices at once (see Figure 2.4).

CT was originally established by the work of A. M. Cormack in the 1960s, who developed the mathematic procedures for reconstruction without knowing that J. Radon had already developed them in 1917 [109; 24]. In that former time, J. Radon invented the Radon transform which is necessary to calculate a 3D object by the so called filtered back projection. Based on this, the tomographic procedure became applicable in the 1970s. The first tomography was published by Hounsfield in 1973 who presented a medical tomography of a human head [63].

Synchrotron radiation based computed microtomography (SR$\mu$CT) was developed from the conventional CT, based on X-ray tubes, in the 1980s by Bonse *et al.* [14] and Flannery *et al.* [35]. X-rays are in general not the only probe to perform radiographies or tomographies, e.g. neutrons are well suited too. Neutrons provide less resolution but a higher penetration depth to materials with high atomic number z. However, due to the comparably easy generation of X-rays, nonhazardous handling and versatility X-rays are commonly used.

Computed tomographic methods complemented the two dimensional radiographies which are known and widely used especially in medicine since the time of W. C. Röntgen. 3D X-ray imaging evolved to a scientific standard tool for fundamental research as well as for medical and industrial applications.

### 2.3.1 X-ray imaging

To obtain an image by raying a specimen requires interaction between the radiation and the penetrated media of the specimen, to yield contrast on the detector screen. Absorption imaging is the most direct method to obtain an radiographic image, i.e. the projection of the X-ray attenuation of an object. The quantitative attenuation for a beam penetrating an object is given by Beer's law:

[9][Root Mean Square]

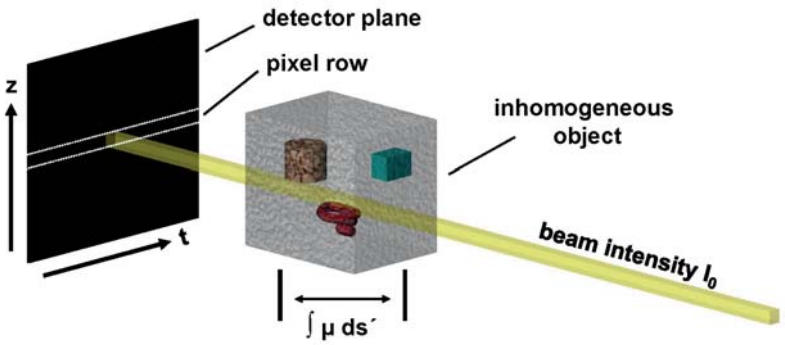


**Figure 2.4:** The integrated attenuation along the beam path $s$ through an inhomogeneous object determines the value for every pixel in every row on the detector plane, described by a $tz\theta$-coordinate system. Out of this a stack of projected object slices is obtained.

$$I(d) = I_0 \cdot e^{-\mu d}, \tag{2.7}$$

$I(d)$ describes the remaining photon flux of a monochromatic electromagnetic beam after travelling distance $d$ through a homogeneous medium, while $I_0$ is the incident photon flux and $\mu$ the attenuation coefficient of the medium.

For any inhomogeneous objects the local absorption coefficient has to be integrated along the beam path $s$, regarding the varying attenuation coefficient as shown in Figure 2.4. By installing a detector downstream the beam path, a projected absorption image of the object can be obtained.

X-rays obey the same laws for waves and optics as any other electromagnetic wave or photon does. The main interactions occur always to electrons, due to their sensitivity to electromagnetic fields. A short overview is given here on the interactions of electromagnetic waves with matter, for detailed information please refer to a textbook, as e.g. from Als-Nielsen [1]. The four main effects are itemised as follows:

- Elastic scattering (*el*)
  ➢ The electron is affected by the field of the electromagnetic wave, oscillating and radiating on the same frequency, like a dipole in classical description. Known as Thomson-scattering for quasi-free electrons and Rayleigh-scattering for the sum in the case of atoms. This interaction is important while it is roughly $\lambda$>Atom diameter, i.e. in the range of soft X-rays and up to hard X-rays.

- Inelastic scattering (*inel*)
  ➢ The incoming photon transfers energy to the electron, and thus propagates with a lower frequency. This so called Compton-effect or scattering is dominating for higher X-ray energies and increases with the specimen size.

- Photoelectric effect (*pe*)
  ➢ An electron absorbs a photon with minimum binding energy of the electron's state. By ionising the atom, the electron is released and dissipates the energy by inelastic collision. This effect is dominant but decreases at higher energy.

- Pair production (*pp*)
  ➢ For energies higher than 1.022 MeV, photons can split in a electron-positron pair: $\nu \rightarrow e^- + e^+$. Due to the conservation of momentum this is impossible in vacuum.

The atomic interaction cross sections $\sigma$ of the four attenuation effects can be calculated as a sum. It is

$$\mu_{total} = \sigma_{total} \cdot n \qquad \text{with} \quad \sigma_{total} = \sigma_{el} + \sigma_{inel} + \sigma_{pe} + \sigma_{pp} \tag{2.8}$$

the total attenuation coefficient, where $n$ is the atom density. The contributions of the single attenuation coefficients are strongly energy and material dependent, as shown by Figure 2.5. For best statistics by attenuation imaging it was found that the minimal transmission $\frac{I(d)}{I} I_0$ should be ideally $e^{-2}$ [49]. Using Equation 2.7 the ideal sample thickness is determined to $d = 2/\mu$.
After [28] the photoelectric effect is highly dominating and no other interaction process significantly affects the absorption imaging[10] while the sample diameter is 1 cm or less, the X-ray energy 10 - 30 keV[11] and by neglecting multiple hits. Thus the attenuation coefficient can be treated as $\mu_{total} \approx \sigma_{pe} \cdot n = \mu_{pe}$.

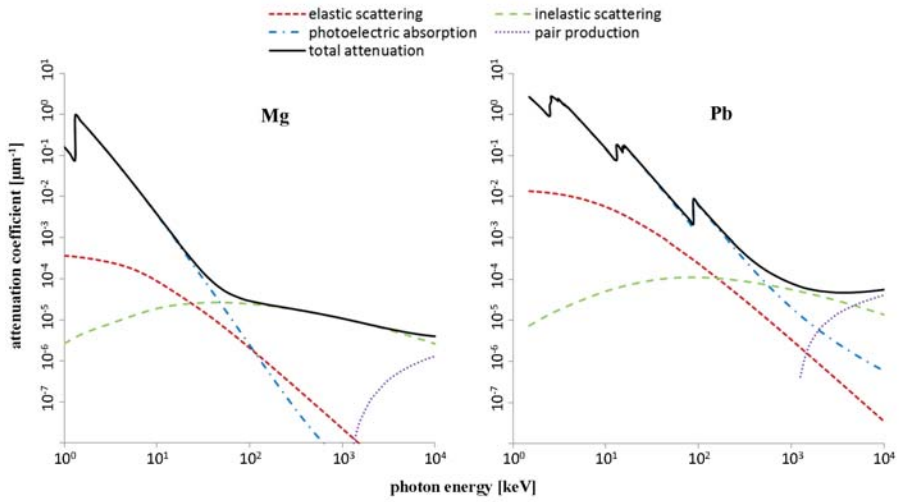


**Figure 2.5:** Exemplary light and heavy element interaction cross sections by magnesium and lead respectively. Calculated by [103].

[10] Crystalline materials do affect this by scattering.
[11] The exact value depends on the individual material.

Experimentally derived, for the energy range from 10 to 100 keV, and apart from absorption edges, the photoelectric attenuation coefficient $\mu_{pe}$ is approximately determined by

$$\mu_{pe} \approx k\frac{n \cdot Z^4}{E^3}. \tag{2.9}$$

With $E$ being the photon energy, $n$ the density in atoms, $Z$ the material's atomic number and a constant $k$ which is depending on the atomic shell [6]. Again, the individual attenuation varies strongly with energy and the elementary composition of the investigated objects.

Furthermore it can be useful for imaging to exploit the photoelectric absorption edge of an element within the sample to obtain increased contrast on the density allocation of this element. The element dependent absorption edges are defined by the energy of the electron shells, resulting in a suddenly increased attenuation when exceeding the individual energy threshold.

Despite the method of imaging by attenuation effects, phase contrast imaging is an important method too. Phase contrast imaging can be especially used for specimen which material composition has quite similar attenuation coefficients, for its sensitivity on different refractive indexes. A short introduction is given in Appendix A.

**The desired resolution** of a specimen by radiography is basically determined by the number of detector pixels. The maximum possible resolution in one dimension is given by $\frac{sample\ size}{pixel\ number}$. For example, to achieve a resolution of 50 nm with a 4096 $\times$ 4096 pixel CCD detector, a theoretical sample size of approximately 200 $\mu$m is needed.
Practically, as a common rule of thumb, 2-3 detector pixels correlate to $\frac{1}{1000}$ of the sample size, which defines the realistic achievable resolution. Out of this follows a sample size of about 50 $\mu$m to obtain a 50 nm resolution.

### 2.3.2 The tomographic method

A tomography is a 3D image of an object, reconstructed out of X-ray projections taken from different angles of an object, as introduced in section 2.3. The presented reconstruction theory in the following is based on the most usual case of parallel X-ray illumination and, as for the exemplarily described projection images, attenuation imaging. Besides this it is also possible and common to use other geometries as e.g. cone beam.

Based on Beer's law (Equation 2.7) the attenuation of the specimen along the beam path $s$ is integrated and defines the projected attenuation $p$:

$$I = I_0 \cdot e^{-p} \qquad \text{with} \quad p = \int_s \mu(s')ds', \tag{2.10}$$

while $I$ is again the intensity of the beam. Now one can calculate the projected attenuation by

$$p = -ln\frac{I}{I_0} \tag{2.11}$$

for each pixel of the X-ray detector camera. Practically this is realised by recording radiographic projection images of the specimen $i$, reference images of the beam $r$ and dark images $d$ during absence of radiation. Out of this $p$ is calculated as

$$p = -ln\frac{i-d}{r-d}, \tag{2.12}$$

with the same camera exposure time for all images $i$ and $r$.

Further on, the spatial system response of the whole X-ray camera in terms of the point spread function has to be considered for the projected attenuation $p$ by measuring the so called edge spread function. The latter is practically obtained by imaging an object which covers half of the viewing field of the camera. The calculation procedure is described in [28].

**Tomographic reconstruction**

The taken radiographic projection images have to be transferred in mathematically projected images in order to reconstruct them to a tomography image. The mathematical basics for this are well known, and e.g. described by Natterer [97] and Kak [69]. The used nomenclature in the following has been adopted from Kak [69]. For cone beam geometry a three dimensional calculation would be needed, as e.g. described by Feldkamp *et al.* [33] and Wang *et al.* [134].

In a $xyz$-coordinate system let the physical properties on a tomographic slice of an object be described by $f(x, y)$, that is in our case determined by the attenuation coefficient $\mu$(x,y) (see subsection 2.3.1). As introduced in Figure 2.4, a related $tz\theta$-coordinate[12] system is used to determine the position on the detector camera screen while images are taken at different angles $\theta$ regarding the object. For X-rays penetrating the object perpendicular to the detector plane (Figure 2.6) one can define the projection along one line $s$ of the penetrating beam on an object slice as

$$p_\theta(t) = \int_{line(t)} f(x(s,t), y(s,t))ds \qquad \text{while} \quad t = constant = x\,cos\theta + y\,sin\theta. \tag{2.13}$$

The integral is thus evaluated for projections along lines of constant $t$, which means parallel lines along the beam ray.

By using the Dirac $\delta$ function, Equation 2.13 for $p_\theta(t)$ can be rewritten as

[12] $z$ is identical in both coordinate systems and constant while considering one individual slice.

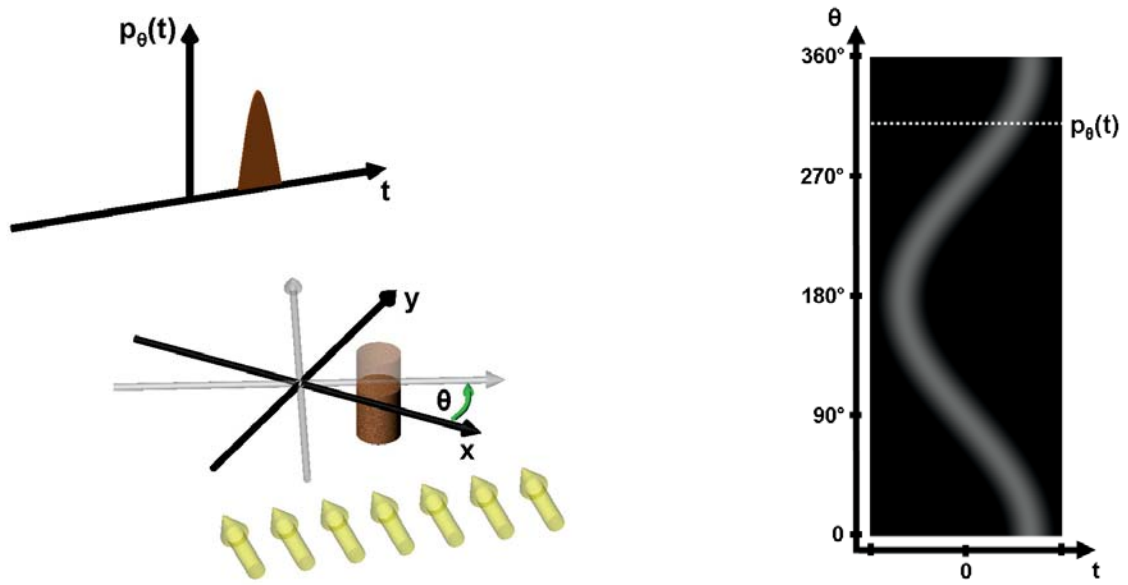


**(a)** real space **(b)** projection space

**Figure 2.6:** (a): The indicated slice of the object (brown coloured) is defined by a $xy$-coordinate system, which is fixed to the object. The object is penetrated by radiation and turned by $\theta$ around the rotation axis in real space $f(x, y)$ while projection images are taken from it. (b): The respective sinogram in projection space $p_\theta(t)$.

$$p_\theta(t) = \int_{-\infty}^{+\infty} \int_{-\infty}^{+\infty} f(x, y)\delta(x\, cos\theta + y\, sin\theta - t)dxdy. \tag{2.14}$$

This is known as the **Radon transform** of $f(x, y)$. Plotted in a $t, \theta$-diagram $p_\theta(t)$ is also called sinogram, due to the fact that every point in $(x, y)$ space is projected onto a sinusoidal line in the $(\theta, t)$ space, as shown in Figure 2.6b.
The one and two dimensional Fourier transforms of $p_\theta(t)$ and $f(x, y)$, as

$$P_\theta(w) = \int_{-\infty}^{+\infty} p_\theta(t)e^{-i2\pi wt}dt \qquad \text{and} \tag{2.15}$$

$$F(u, v) = \int_{-\infty}^{+\infty} \int_{-\infty}^{+\infty} f(x, y)e^{-i2\pi(ux+vy)}dxdy, \tag{2.16}$$

are needed in the following for reconstruction. The **Fourier slice theorem** connects the function $f(x, y)$ and its projection $p_\theta(t)$ in Fourier space by

$$P_\theta(w) = F(w\, cos\theta, w\, sin\theta). \tag{2.17}$$

The Fourier transform $P_\theta(w)$ relates to the values of $F(u, v)$ in the polar coordinate system of $(w, \theta)$ along a radial line through the origin, which is rotated in the Cartesian coordinate system $(u, v)$ by the angle $\theta$ (Figure 2.7) [28].

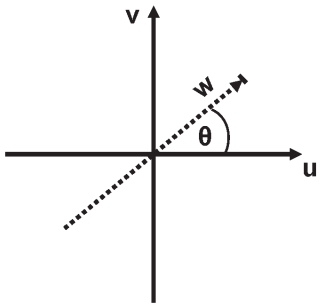


**Figure 2.7:** Scheme of the frequency space with the line of $F(u, v)$ and $P_\theta(w)$, determined by Cartesian and polar coordinates respectively.

When the entire two dimensional Fourier space is covered by the radials of $F(u, v)$, it is possible to recover $f(x, y)$ from the taken projection data $p_\theta(t)$ by Fourier transformation and the Fourier slice theorem. Hence the full information for reconstruction is given when the angles $\theta$ cover the radian range $[0, \pi]$ or another similar interval of this width.

By inverse Fourier transformation of $F(u, v)$ the function $f(x, y)$ is written as

$$f(x, y) = \int_{-\infty}^{+\infty} \int_{-\infty}^{+\infty} F(u, v) e^{i2\pi(ux+vy)} du dv. \tag{2.18}$$

This changes to

$$f(x, y) = \int_{0}^{\pi} \int_{-\infty}^{+\infty} |w| P_\theta(w) e^{i2\pi wt} dw d\theta, \tag{2.19}$$

when transferring from the Cartesian $u, v$- back to the polar $w\theta$-coordinate system and making use of the introduced Fourier slice theorem, Equation 2.17. The term $|w|$ is introduced by the coordinate system transformation, and can be used to adopt a filter to the inversion algorithm. Thus, the inner integral of Equation 2.19 is called the filtered projection, while the outer integral is known as backprojection. For algorithms which are based on this **filtered backprojection** (FBP), the knowledge of the position of the centre of rotation ($t = 0$) is mandatory. For further information on the iterative determination of the centre of rotation in recorded sinograms refer to [28].

By defining a filter function as $H(w) = |w|B(w)$ and its inverse Fourier transform $h(t)$

$$f(x, y) = \int_{0}^{\pi} \int_{-\infty}^{+\infty} H(w) P_\theta(w) e^{i2\pi wt} dw d\theta, \tag{2.20}$$

is obtained, or as convolution in real space

$$f(x, y) = \int_{0}^{\pi} h(t) * p_\theta(t) d\theta. \tag{2.21}$$

In this equation $*$ marks the one dimensional convolution operation. Using the term B(w) in the filter function, a filter can be applied that suppresses the noise at high frequencies at the cost of a lower spatial resolution. There are many possibilities to design algorithms with additional filter functions, due to the varieties of desired accented results.

Although convolution in real space as filtering in frequency space are mathematically the same, one often refers to reconstruction algorithms based on Equation 2.21 as convoluted backprojection (CBP) algorithms and those based on Equation 2.20 as FBP algorithms.

In contrast to the mentioned reconstruction algorithms which are based on the presented filtered backprojection, there exist others that make use of algebraic [43] or statistical techniques [110].

## 2.4 Nanotomography at IBL

In the following the nanotomographic experiment at the *imaging beamline* P05 (IBL) at the storage ring PETRA III[13], will be described. The beamline P05 is located in sector 4 in the PETRA III experimental hall, and shares the sector with the *Hard X-ray micro/nano-probe beamline* P06. The imaging beamline is housing the micro- and the nanotomography as well, and some general devices as e.g. the monochromators which are used by both experiments.
Caused by the small beam size and divergence (see Table 2.1), the microtomography hutch had to be installed subsequent to the nanotomography hutch (Figure 2.8). The more diverged and thus bigger beam is needed by the microtomography experiment for dealing with bigger samples. This geometry additionally allows to use the detector camera of the microtomography experiment in the second hutch downstream the beam in combination with the nanotomographic experiment.
A beam pipe changer is mounted in the nanotomography hutch to enable either a continuous vacuum for the beam if the microtomography is running, or to switch easily to nanotomography by lifting the pipe.

The microtomography in the second hutch works according to Figure 2.4 without X-ray optics. Here the detector consists of a scintillator screen from which the image is magnified by visible light optics to a 60 mm $\times$ 60 mm[14] camera plane. The optics are fitted to provide magnifications of M = 5×, 10×, 20× or 40× [104]. This allows sample sizes of roughly 1 to 7 mm for the microtomography.

[13] introduced in subsection 2.2.1
[14] corresponding to a 4096 $\times$ 4096 pixel CCD

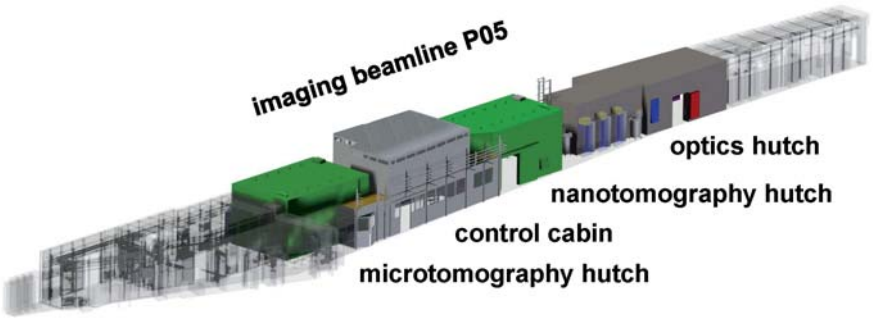


**Figure 2.8:** Layout of PETRA III sector 4 without front end. The beamline P05 is coloured while P06 is blanked in grey. The first experimental hutch downstream the beam ray is dedicated to the nanotomography while the second one is for microtomography [104].

### 2.4.1 X-ray source and front end

An undulator in low -$\beta$ mode generates the X-rays for IBL, as already mentioned in section 2.2 and subsection 2.2.1. The installed PETRA III standard undulator has a length of 2 m, a minimum magnetic gap of 9.5 mm and a period length of 29 mm with an amplitude of 0.81 Tesla [3]. This generates a X-ray beam of roughly $37 \times 6$ $\mu m^2$ (horizontal $\times$ vertical) and a divergence of $27 \times 5$ $\mu rad^2$, related to RMS[15], refer to Table 2.1.

A carbon filter is fixed in the front end, as well as further optional carbon and copper filters, in order to avoid thermal load on the downstream components by absorbing the low frequencies of the whole spectrum. Two water cooled slit systems are installed in the front end. The first one is a fixed slit system to extinct the two useless beam cones, which are always generated by an undulator besides the main beam. The second one is to fine tune the beam size. A water cooled diamond window separates the experimental part from the front end of the beam line, like the obligatory beam shutter does too.

### 2.4.2 Beamline optics

The monochromators are located in the optics hutch. Here the X-ray beam is adjusted in energy by a silicon double crystal monochromator (DCM) in Bragg geometry or a double multilayer monochromator (DMM) which is going to be installed in 2015. The original harmonics of the undulator source, which are much broader, are tailored by passing those devices. In both cases the monochromatisation is physically based on constructive interference by reflection on well aligned planes. In the first case the beam is reflected by the lattice planes of the crystals (see Figure 2.3 in section 2.2), while in the latter case this happens by reflection on the planes of the multilayer stack.

[15] root mean square

For the Bragg geometry there are two facilities present, one silicon 111 DCM set and one silicon 311 DCM set. This double DCM is the standard DESY monochromator layout for PETRA III, and provides a small energy bandpass, i.e. it is $\delta E/E \approx 10^{-4}$. This enables very defined energy settings, which are e.g. required for absorption edge imaging and tomography.
The DMM shall cover an energy range of 5 to 50 keV, there are different coatings to be done inhouse at HZG [129]. The main advantage of the DMM is the high reflectivity and the large energy bandpass of $\delta E/E \approx 10^{-2}$, resulting in an increased photon flux by two orders of magnitude compared to the DCMs ($\delta E/E \approx 10^{-4}$) [104].

### 2.4.3 X-ray optics

To achieve nanoscale resolution by the nanotomography experiment, focussing and magnifying X-ray optics are needed. The real part $1 - \delta$ of the complex refractive index

$$n = 1 - \delta + i\beta, \tag{2.22}$$

is responsible for refraction of an electromagnetic beam at a boundary, physically caused by different group velocities in different media.

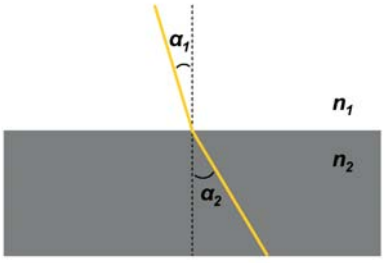


**Figure 2.9:** Schematic refraction behaviour of X-rays at a boundary.

Snell's law describes the refraction of an electromagnetic wave by transition from one medium into another. It is also applicable for the range of X-rays, and by implication of Equation 2.22 it is

$$\frac{sin\alpha_1}{sin\alpha_2} = \frac{\mathrm{Re}\, n_2}{\mathrm{Re}\, n_1} = \frac{1 - \delta_2}{1 - \delta_1}. \tag{2.23}$$

The principal of refraction with X-rays is quite the same as it is for the range of visible light, but now the real part of the refractive index $n$ is smaller for optical denser materials. Hence, a beam which is passing from a lighter to a denser medium is refracted away from the surface normal (Figure 2.9). The opposite happens with visible light. A biconvex shaped lens for visible light effects qualitatively the same as a biconcave X-ray lens on X-rays.
Further, the media dependent differences in the real part of the refractive index $\delta$ are quite small for X-rays, resulting in a weak refraction. To compensate for this,

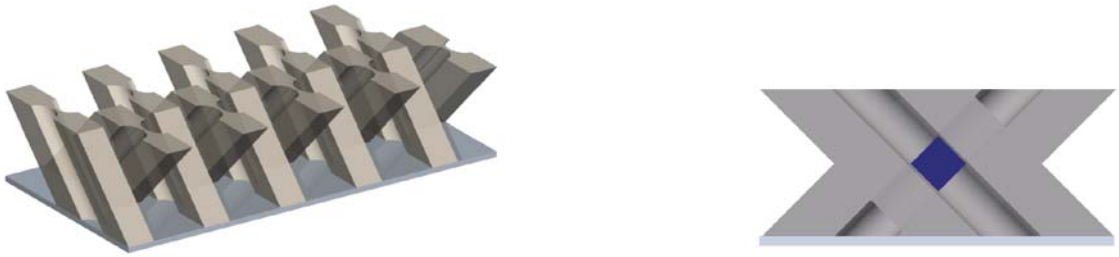

**(a)** X-ray lens pack

**(b)** X-ray lens pack in beam direction

**Figure 2.10:** Crossed X-ray lens layout of a CRL (a) and in cross sectional view (b). The one dimensional focussing segments alternate in orientation by 90° in order to create a two dimensional focus [117] (illustration from [104]).

compound refractive lenses (CRL), consisting of a pack of subsequently arranged single X-ray lenses (Figure 2.10), are applied [79; 118]. The focal length $f$ for a lens element is given by

$$f = \frac{R}{2\delta}, \quad \text{which changes to} \quad f = \frac{R}{2N\delta}. \tag{2.24}$$

$N$ is the number of lens elements and $R$ the radius of curvature. Example: To decrease the focal length to 1 m while using hard X-rays with $\delta \approx 10^{-6}$, a single lens would need a radius of curvature of 1 $\mu$m, which makes it uselessly small. By using a CRL at the same focal length consisting of 100 single lenses, the radius of curvature would be about 100 $\mu$m [9].

CRLs can be produced by pressing techniques using beryllium or aluminium [78]. Lightweight elements are dedicated for hard X-ray lens material because of their $\delta/\beta$[16] ratio, which is higher for lower atomic number $Z$.

To avoid speckles with polycrystalline lenses at $3^{rd}$ generation synchrotron sources other techniques like deep X-ray lithography have to be applied [98]. This technique is very precise and enables also alternating structures on one substrate, as shown in Figure 2.10. In order to increase the usable aperture and to avoid spherical aberrations, parabolic lens profiles are often used too [78].

For imaging purposes also diffracting Fresnel zone plates could be used, but regarding the optimum efficiency they are limited to the sub 10 keV range. Thus CRLs are generally used for nanotomography imaging at IBL.

### 2.4.4 Nanotomography setup

The experimental hutch is positioned 63.5 to 72.5 m from the undulator source. About 7 m of the hutch can be used for the experiment itself. As optical bench to arrange the single components with respect to another, and as vibrational

[16] i.e. the amount of refraction per absorption, compare Equation 2.22

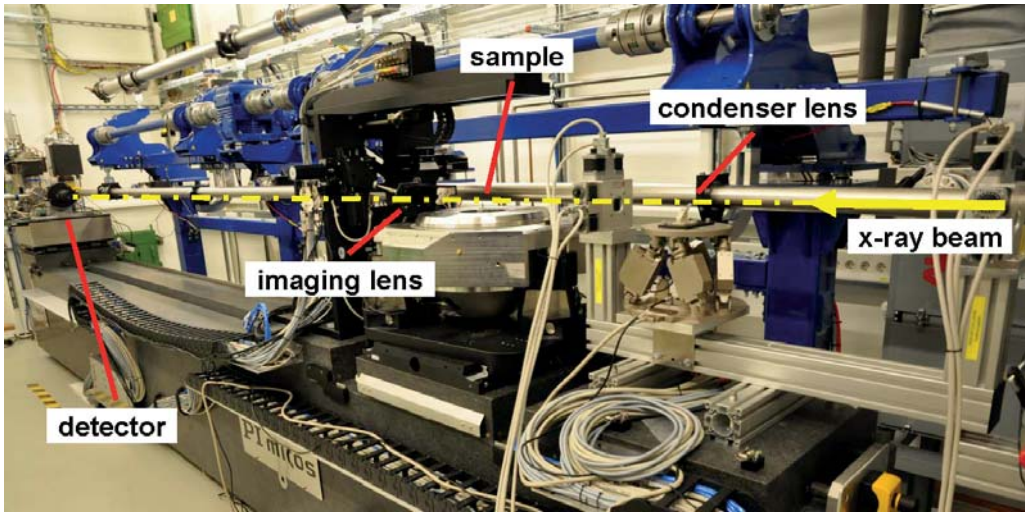


**Figure 2.11:** The inside of the nanotomography hutch with the granite slab and the beam pipe changer. The X-ray microscopy setup is currently mounted on the slab, while sample, lenses and the detector position are marked.

dampener as well, the experiment itself is mounted on a 6.8 m long and 10 t weighted granite slab (Figure 2.11). Also the sample positioning and rotation is designed to allow highest precision, which is mandatory for imaging and reconstruction of samples in the nm range. E.g. by using an encoder the rotational error can be reduced to around $10^{-5}$ deg. The movement of the center of the axis of rotation, called radial error, was determined among others by M. Ogurreck to 21.43 nm. For further details view [104].

In general the setup of the nanotomography experiment is similar to the microtomography setup using a scintillator detector, but has an addition by X-ray optics to yield the desired magnification.

As introduced in subsection 2.3.1 projection images are taken in transmission. The projected attenuation is caused by the physical properties inside the object along the beam path. For high resolution tomography, microscopy X-ray techniques are required. To realise this, there exist three basic methods: scanning transmission X-ray microscopy, full field transmission X-ray microscopy and cone beam projection. At IBL the latter two are considered, while the cone beam setup includes always the possibility for scanning techniques. Those two, generally different experimental layouts, are shown in Figure 2.12. A diffuser could be applied in the case of transmission microscopy to enhance angle broadening for a more divergent beam at the position of the sample. The calculations for these two different optical setups were done by Ogurreck [104]. The following description is focussed on the results.

The nanotomography experiment is dedicated to provide resolutions in the nm range, which requires in general very small samples in the $\mu$m range (discussed in subsection 2.3.1). Apart from this, the experimental optics limit the field of view

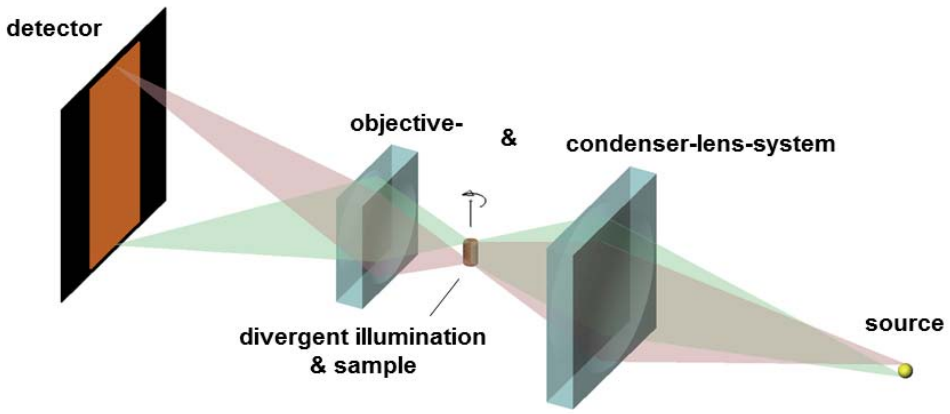


**(a)** X-ray microscopy tomography setup

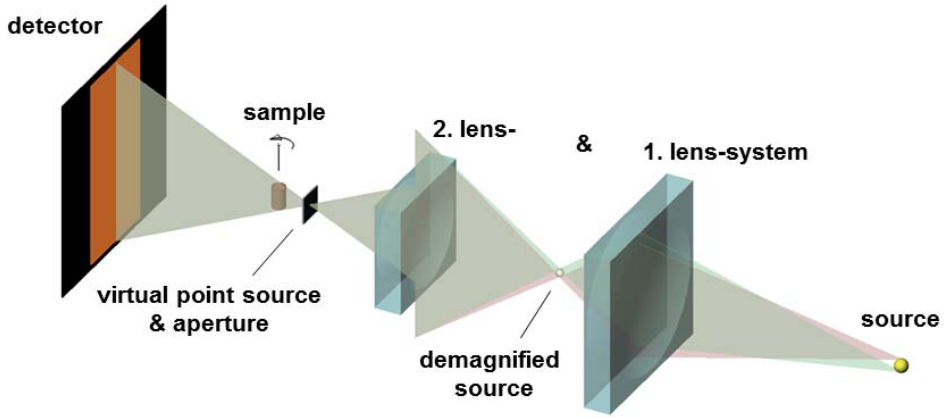


**(b)** Cone beam tomography setup

**Figure 2.12:** For X-ray microscopy (a) the sample has to be illuminated with a beam whose divergence fits to the numerical aperture (NA) of the objective lens. For cone beam tomography (b) a nanometer sized virtual source is generated by the X-ray optics.

to a size of $60 \times 60 \times 60$ $\mu$m.

### X-ray microscopy setup

For X-ray microscopy (Figure 2.12a)the numerical aperture of the **objective lens** system, i.e. in this case the CRL, is limiting the resolution. The numerical aperture $NA$ is in general defined as

$$NA = n\, sin\alpha, \tag{2.25}$$

where $\alpha$ is half the opening angle of the light cone, if the lens is illuminated by a parallel beam and focuses the light in the distance $f$ (Figure 2.13). In case of

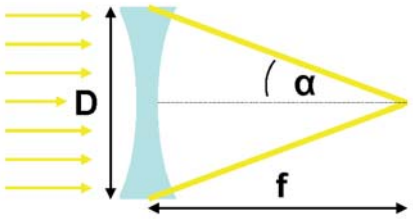


**Figure 2.13:** Definition of the numerical aperture of a focussing lens with the half opening angle of the light cone $\alpha$ during parallel illumination. The aperture opening of the lens is defined by $D$.

X-rays $n \approx 1$, and since $\alpha$ is very small $sin\alpha \approx tan\alpha$ can be approximated. By the definition $tan\alpha = \frac{D/2}{f}$, it follows

$$NA \approx \frac{D}{2f}. \tag{2.26}$$

The definition for two features with distance $R$ still being resolved [9] is

$$R = 0.61\frac{\lambda}{NA}. \tag{2.27}$$

Combining this with Equation 2.26 in the case of X-ray lenses one obtains

$$R = 1.22\frac{\lambda f}{D}. \tag{2.28}$$

This equation makes it obvious that the objective lens should feature a short focal length and a large aperture in order to increase the resolution.

Further on it is necessary that the field of depth of the objective lens is larger than the sample thickness, to obtain a sharp and uniformly resolved projection image. Hence, the chosen maximum sample size, and thus the field of view, determines the minimum focal length. A focal distance of $f = 100$ mm was chosen for the objective lens with an aperture diameter of $D = 100$ $\mu$m. Out of this, the achievable resolution is calculated to be below 100 nm [104].

The **condenser lens** system is required to adapt the beam divergence to the numerical aperture of the objective lens, i.e. to cover the full angular acceptance between 5 and 10 mrad. For the source of PETRA III, providing a beam divergence between 5 and 30 $\mu$rad [RMS] (see Table 2.1), this can't be achieved without condenser optics enhancing the beam divergence. The source should not be imaged at the sample position, a proper beam expansion and divergence is needed to illuminate the sample.

The resulting condenser lens system has a focal length of $f = 650$ mm with an aperture of $D = 600$ $\mu$m, and fully adapts to the divergence and beam size requirements. Any further increase of the divergence would yield nothing but decreasing the photon flux.

The 2D resolution of this setup was determined by a Siemens star to below 100 nm. Even with bad contrast additional parallel lines could still be distinguished for a distance of 90 nm [104].

### Cone beam setup

Cone beam tomography (Figure 2.12b) means to ray a specimen by a light cone with an ideal point source origin. The sample size itself and the distance to the detector define the magnification.

Besides the limitations to the resolution discussed in subsection 2.3.1 the resolution is now given by the expansion of the source. The size of the sample features being resolved is equivalent to the source spot size. To provide a proper approach to a point source the expansion of the original PETRA III beam has to be demagnified. Classical lenses provide an image magnified or demagnified by $M$, defined by the relation

$$M = \frac{d_{source-lens}}{d_{lens-focus}}. \tag{2.29}$$

Since a resolution and thus a target spot size of 50 nm is considered, a demagnification of $M \approx 1800$ is needed (referred to the beam dimensions given in subsection 2.4.1). In order to preserve simple handling of the sample, there should be enough space between lens, sample and detector. Hence, the divergence ought to be kept moderate.

In practice the source demagnification is realised in two steps, i.e. for the demagnification it is $M_1 \times M_2 \approx 1800$. Hereby the source to the second lens is the demagnified image spot provided by the first lens.

An aperture of which the opening was prepared by the later discussed focussed ion beam (FIB) device of HZG (section 3.2) is installed at the position of the virtual source to suppress strayed X-rays.

## 2.4.5 Sample requirements

Due to the required nano scaled resolution the samples have to be $\mu$m scaled (subsection 2.3.1). As mentioned in subsection 2.3.2, the sample can only be fully reconstructed if the angle of sample rotation $\theta$ covers not less than the range of $[0, \pi]$. Cylindrical shaped specimens would provide a homogenous attenuation range during the applied rotation.

A pillar shaped specimen with the maximum lateral diameter of 40 $\mu$m fits all requirements (Figure 2.14). The sample would be positioned in the very heart of the beam where it is most stable. By this shape it is guaranteed that at every angle $\theta$ the sample is fully imaged, even if beam variation occurs or the centre of rotation does not fit perfectly. If the height of the pillar is longer than the viewing field, the tomography could be performed in several height steps. Once the data is taken it could be reconstructed to one 3D object.

IBL is equipped with a sample holder system providing automatic sample identification and handling (Figure 2.14). For nanotomography these holders had to be

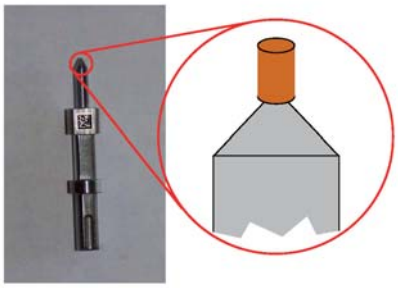

**Figure 2.14:** Photography of an IBL sample holder with schematic magnification of the top. For nanotomography the top, with an original diameter of 2 mm, is sharpened to cone shape and the cylindrical sample is positioned on the tip.

sharpened to gain a free field of view to the sample by divergent and cone beam illumination.

To prepare samples in the required dimensions and for complementary characterisation, a scanning electron microscope (SEM) with focused ion beam (FIB) device was used providing maximum flexibility to adapt different kinds of samples. This device is presented in the next chapter.

## 2.5 Synchrotron-radiation-based X-ray scattering

### 2.5.1 Introduction to X-ray diffraction

X-ray scattering experiments that show diffraction patterns allow to conclude detailed information about the material chrystallography in the interaction volume. A short introduction is given here, for more information please refer to a textbook as e.g. by Zolotoyabko [148]. The crystal structure in solids forms lattice planes on which incoming X-rays are scattered elastically by the angle $\theta$. Constructive interference by plane electromagnetic waves occurs on families of lattice planes in a crystal if the Bragg condition $2d\,sin\theta_B = n\lambda$ is fulfilled (section 2.2, Figure 2.3). Describing this incoming wave in reciprocal space by wave vector $\vec{k}$ enables to describe the scattering process with a directional change to $\vec{k'}$. The Bragg condition is again fulfilled if $\Delta\vec{k}$ is equal with a translation vector $\vec{G}$ of the reciprocal lattice (Equation 2.30), also known as Laue condition.

$$\vec{k} - \vec{k'} = \vec{G}, \tag{2.30}$$

The accessible diffraction reflexes can be visualised by the so called Ewald-construction (Figure 2.15).

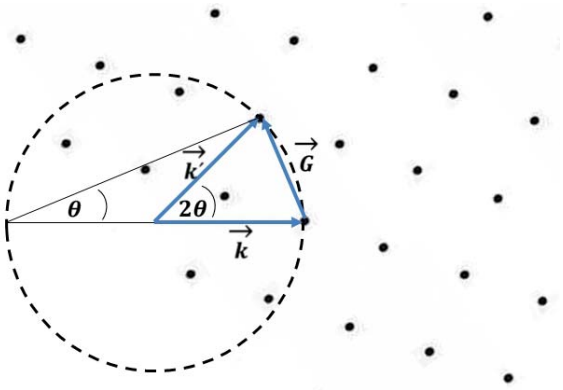


**Figure 2.15:** Ewald-construction to determine point reflexes in reciprocal space.

The wave vector $\vec{k}$ has to be drawn along the horizontal X-ray beam direction *to* a lattice point, defining the origin of the reciprocal space. The cutting points of a sphere with radius $r = |\vec{k}| = \frac{2\pi}{\lambda}$ with the reciprocal lattice points define the observable reflexes. If the crystal is rotated in real space, the reciprocal space is also rotated around its origin, changing the possible diffraction points on the Ewald-sphere cutting points.
Hence, a single crystal would have to be rotated during measurement to obtain all accessible reflexes. If the material is statistically composed out of many crystal grains the whole diffraction data can be obtained at once, without rotating the sample.
By such a measurement, the phase composition in solids can be determined

statistically by comparing the resulting data with calculated diffraction pattern of crystal models.

### 2.5.2 Nanodiffraction at Petra III

Nanodiffraction describes a diffraction experiment using a nanofocused X-ray beam in combination with thin samples, which is therefore providing a much higher resolution.
In the following the nanofocus endstation of the MiNaXS beam line (P03) at PETRA III at DESY (Hamburg, Germany) was mainly used for nanodiffraction.
A horizontal emittance of about 1 nm rad as provided by PETRA III is crucial to generate a beam in the range of nanometers. CRLs generate a virtual point source and subsequent installed Kirkpatrick-Baez mirrors enable a beam size of to date $250 \times 350$ nm$^2$ [93].
The sample preparation follows in general the same steps as for nanotomography, described in the following chapter. However, instead of cylindrical specimen some $\mu$m thick lamella shaped specimens are processed for this experiment by the FIB device.

# Chapter 3

# Instruments and methods: SEM and FIB

In contrary to X-ray microscopy techniques classical microscopy is constricted to the characterisation of the surface. By using visible light this technique is accessible at low costs and established as a basic laboratory tool. However, the resolution for visible light is limited by the wavelength and the numerical aperture of the microscope. The most modern microscopes of this kind reach a resolution between 300 and 200 nm. A scanning electron microscope (SEM) yet enables to image nanometer sized features due to the shorter electron wavelength.

Since H. Busch invented magnetic lenses for electrons in 1925, in analogy to lenses for visible light made of glass, it was possible to build electron microscopes. The very first electron microscope was built in 1931 by E. Ruska and M. Knoll, but it could only image a single spot on the surface of the specimen [73]. Four years later, the theoretical basics for a scanning electron microscope were again laid by Knoll [72].

The first scanning electron microscope was made by M. von Ardenne in 1937, with a spot size and thus resolution of 10 nm. The aim was to build an electron microscope that extincts the chromatic aberration. This aberration is inherent to the so far established *not scanning* electron microscopes which obtain the image as a whole.

Based on the work of McMullan [91; 92], Smith & Oatley [124; 102] and Wells [136] *Stereoscan* (Cambridge Instruments Ltd.) offered the first commercial SEM in 1965. "Since this commercialization in the mid-1960s the SEM has revolutionised the study of fracture surfaces and, more recently, made crucial contributions to the science and engineering of microelectronic devices to the point where it is an essential presence on commercial fabrication lines" [99]. A complete historical bibliography with publications on developments in the field of SEM since this time can be found in [123].

The focussed ion beam (FIB) technique uses generally the same function principle as scanning electron microscopy. In addition ion beam milling and surface

structuring is possible due to the much heavier ions, compared to electrons. The crossbeam device used for this thesis in order to perform specimen preparation and pre analysis for nanotomography at IBL and nanodiffraction at MiNaXS (see section 2.4 and subsection 2.5.2) is the workstation Auriga 40 from *Zeiss* (Oberkochen, Germany) of the Helmholtz-Zentrum Geesthacht (HZG). The Auriga is providing both, electron microscopy and focused ion beam using gallium ions. All kinds of SEM or FIB investigations in this thesis were done with this device.

## 3.1 Introduction to SEM techniques

Scanning electron microscopy (SEM) features a magnified image of the specimen's surface by scanning it with a nanometer sized electron beam spot. The different response signals to this electron irradiation are measured by certain types of detectors for every single local spot of the scan region on the sample. The signal intensity is amplified and visualised by grey values on a screen. Hence, the maximum achievable resolution is generally determined by the spot size of the electron beam focus. The magnification is determined by the expansion of the scanning region on the specimen.

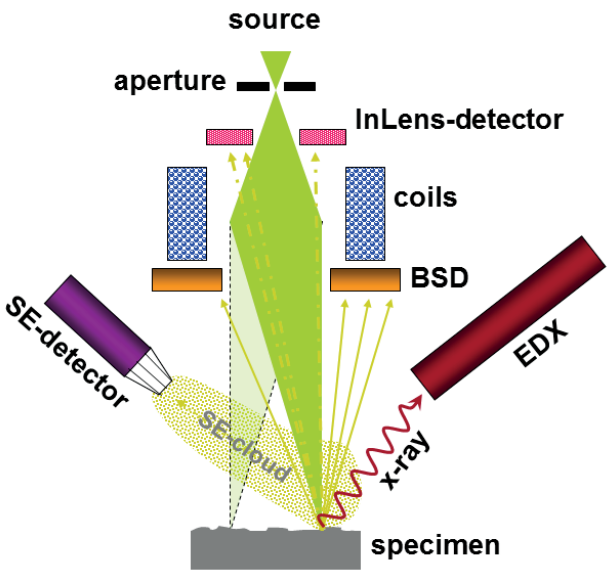


**Figure 3.1:** SEM principle: the surface of the sample is scanned by a nanometer focussed electron beam, generated by the SEM column (indicated by aperture and objective coils); the different responses to this irradiation on the surface are detected for every scan spot by specialised detectors.

Starting at the source, the electrons are emitted from the cathode by an electrical field, given by the so called extractor voltage $U_{Ext}$. Subsequently the electrons are accelerated into the SEM column by a tunable electron high tension $U_{EHT}$. The column consists generally of the magnetic condenser lens, different apertures, the focussing objective lens and obligatory scan coils.
To minimise the lateral electron beam cross section and to focus it on the specimen, electron lenses are used. Those lenses operate usually magnetically by the effect

of the Lorentz force $F = ev \times B$. This is forcing the different electrons to helix paths, which are crossing in a focus. Hereby also an image rotation occurs.
The SEM lens system is not used for direct imaging but its only purpose is to focus the electron beam to the smallest possible point.
The errors of electron lenses are as follows [111]:

- *spherical error*; if the beam incidence is too far from the optical axis a shorter focal length results. This error is generally increasing with focal length.
- *chromatic error*; occurs by varying electron energy. Can be avoided by stabilised $U_{EHT}$ and lens currents.
- *axial astigmatism*; caused by magnetic inhomogeneities, mechanic asymmetries of lens drill holes as well as charging of drill holes or apertures, and is resulting in two line foci. This error can be corrected by cylindrical electric or magnetic correction fields, providing the desired rotationally symmetrical focus spot.
- *diffraction error*; due to the aperture boundary, the electron waves close to the focus maximum cannot annihilate by interfering.

A major benefit of SEM is the large depth of focus, due to the comparably small numerical aperture of $NA$[1] $< sin(1°)$ [119].
Beside the smallest possible spot size the main parameters determining a SEM measurement are the electronic high tension, the working distance (WD) or focal length, and the type of response electrons caught by the applied detector.
To enable the operation of the gun, and to avoid collisions between electrons and gas molecules, the whole SEM system is evacuated to UHV.

### 3.1.1 Electron scattering

In general two different mechanisms explain the scattering of the electrons in the specimen.
**Elastic scattering** occurs when an electron beam with a lateral cut of $d\sigma$ passes an atomic core with charge $+Ze^2$. The Coulomb force $K = -e^2Z/r^2$ affects a hyperbolic deflection of the electrons with deflection angle $\theta$. By this, the incoming parallel beam with cross section $d\sigma$ dissociate with opening angle $d\Omega$. The differential cross section is given by Rutherford:

$$\frac{d\sigma}{d\Omega} = \frac{e^4Z^2}{16E_0^2\, sin^4\theta/2}\left(\frac{m_ec^2 + E_0}{m_ec^2 + E_0/2}\right)^2, \quad \text{with } E_0 = eU_{EHT}. \tag{3.1}$$

[1] definition of $NA$ in section 2.4.4
[2] In every single case the shielding of the electron shells has to be considered.

In case of big scattering angles $\theta$ the electron spin has to be considered too. Then much bigger values as given by Equation 3.1 can occur, as it is the case for electron backscattering [111].

**Inelastic scattering** happens by electron - electron scattering, and causes a loss of energy. This happens by ionisation, excitation of shell electrons to higher energetic states, as well as excitation of plasmons. Inelastic interaction occurs mainly at small scattering angles. Hence, one can neglect the scattering angle $\theta$ and concentrate on the energy loss along the trajectory [111].

Compared to heavy particles as e.g. protons which steadily loose energy along their path, electrons have a less defined penetration depth. All ionisation energies of the atom shells have to be known to calculate an average energy loss $dE$ per path element $dx = \rho ds$[3]. Bethe introduced in 1933 a standardised deceleration formula, using an average ionisation potential $I$ of the atom, with $I = 11,5\ Z$ in eV and $N_L/A$ the amount of atoms per area[11]:

$$\frac{dE}{dx} = \frac{2\pi\ N_L\ e^4\ Z}{A\ E_0}\ \ log\frac{E_0}{I}. \tag{3.2}$$

Summing up both scattering mechanisms, the penetration depth can only be determined experimentally by the approach

$$R = a\ (E_0)^n \quad \text{in } [\mu g/cm^2], \tag{3.3}$$

with the energy and material dependent constants $a$ and $n$[4].

### 3.1.2 Imaging signals

Generally two different types of electron responses to the electron beam on the investigated surface occur: backscattered electrons (BSE) and secondary electrons (SE). The former came directly from the electron gun and penetrated the material, interacted elastically or inelastically with the atomic cores which scattered them back, in direction of the electron gun. If elements with a higher atomic number $Z$ are present in the specimen's material at the electron beam spot, more electrons are scattered back than at spots with lower $Z$ value composition. The intensity is visualised by the backscattered electrons detector (BSE-detector). The BSE-detector is situated directly under the outlet port of the electron column (Figure 3.1), providing material contrast.

The SE are generated by interaction with the primary electron (PE) beam. The SE which are generated by PE are called SEI. The BSE generate additional SE along their path, which are called SEII. Due to the lower energy of BSE compared to PE their ionisation probability is higher. Hence, a single BSE generates more SEII than a single PE releases SEI [111].

[3] $\rho$ is material density.

[4] $n$ is typically varying between 1,3 and 1,67 [111].

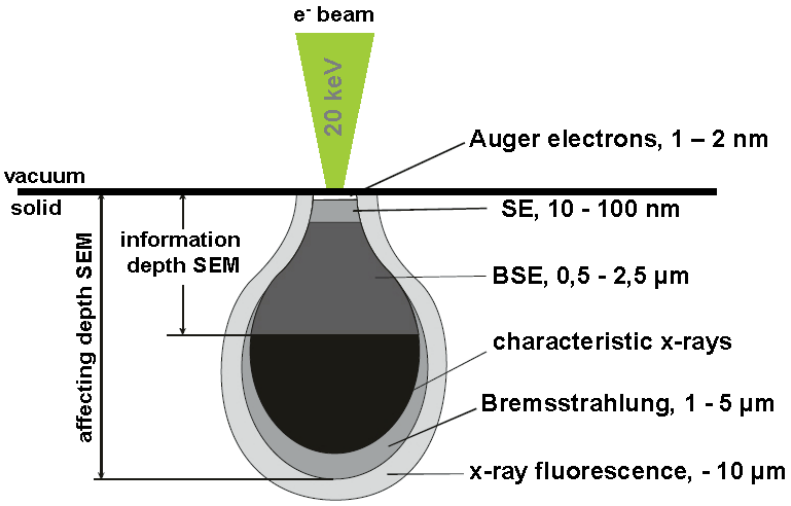


**Figure 3.2:** Schematic chart of the regions in the sample that related to different responses to a 20kV electron irradiation, after [8].

The detected signals cannot be totally assigned to BSE and SE by the detectors. It is mainly for the backscatter direction, as also for the position of the BSE-detector and the much higher energy of the BSE, that the BSE-detector detects mainly them.

At lower primary energies it is not possible to distinguish between SE and BSE, and all escaping electrons are counted as SE. At higher energies the electrons below 50 eV are conventionally assigned to SE. In general about 70% of the escaped SE have an energy of below 15 eV [111].

The SE can escape the material only from small depths $z$ by overcoming the electron affinity. The probability to escape can be described by the exponential law

$$p(z) = p(0)\, exp\left(-\frac{z}{d}\right). \tag{3.4}$$

The "escaping depth" $d$ is in the range of 10 Å for metals and in the range of 100 Å for carbon or similar material [111; 121].

Due to their diffuse and cloud like generation, SE must be caught with a detector which is using a sucking tension. This so called secondary electrons detector (SE-detector) is placed laterally to the SEM column, and therefore sensitive to the topography of the specimen: The electrons of directly accessible regions can easier be sucked by the SE-detector than the ones generated in valleys on the specimen's surface. Together with edge flare this effects the topography contrast of the SE image.

In Figure 3.2 all kinds of reactions to the electron irradiation are shown. The detected main signal comes always from the upper centre part, given by the original spot size expansion of the SEM beam. The entire interaction volume, releasing electrons by cascade collisions too, is much bigger. The SE enable to visualise the surface and topography, for they are emitted only from a thin surface region. In contrary to the BSE that come from a much bigger and deeper volume. Furthermore, different types of x-rays are generated by the incoming beam. The

exploitation of characteristic x-rays will be discussed in subsection 3.1.3.

**High resolution** is possible if the interaction volume in the sample is either big and homogeneous enough, merely contributing to the signal as a constant background noise, or if it is about the same size as the beam spot size. In both cases the main signal, coming from the beam spot region on the surface, has enough contrast to the surrounding and is not significantly affected.
If scanning transmission electron microscopy (STEM) is applied, the sample has to be as thin as for transmission electron microscopy (TEM) - providing a thickness of less than 100 nm. Now interaction volume is respectively limited and the resolution is no longer limited by the signal noise.

By comparing the amount of charge which is given by the SEM gun to the specimen, and that one leaving the sample again - directly or as a cloud of SE - it is found that the incoming fraction is much higher. To avoid a charging of the sample it is mandatory to fix the sample on the respective holder by a conductive connection, e.g. by silver glue (solvent: n-butylacetate).
In case of insufficient internal specimen conductivity the sample is charged which leads to a locally deflection of SE, generating annoying effects in the SEM image. For those samples surface conductivity can be achieved by sputtering a conductive coating to the specimen. During this thesis a sputter device SCD 030 from Balzers Union (Balzer, Liechtenstein) with gold-palladium target was used for this. To achieve an equal deposition thickness of the coating, each sample was exposed for 50 - 60 s at 30 mA.

### 3.1.3 Energy dispersive X-ray spectroscopy

The irradiation by SEM generates SE and causes holes in the electron shells of the atoms in the specimen. This happens directly by electrons from the gun, kicking out electrons from the atom shells, and indirectly via already generated X-rays or higher energetic secondary electrons and BSE from the surrounding. This empty electron place in lower energetic shells is filled with an electron from a higher energetic shell. The energetic difference is radiated by a characteristic X-ray which can be assigned to the respective atom shell (Figure 3.3).

The energy of this X-ray photon can be measured by a detector, which is either a lithium drifted silicon detector (Si(Li)) or a silicon drift detector (SDD). The older Si(Li) detector type consists of a cylindrical silicon crystal, while the SDD is made out of silicon wafers and enables a 10 times faster measurement. The function principle is basically similar: incoming X-rays generate electron-hole pairs which are separated and drifted by a voltage to the electrodes. The amount of generated electron-hole pairs is proportional to the energy of the X-ray photon. By this energy dispersive X-ray spectroscopy (called EDX or EDS), the elementary composition of the specimen can be detected with an energetic resolution of up to 100 eV.
As presented in Figure 3.2, the entire volume from where the EDX signal is

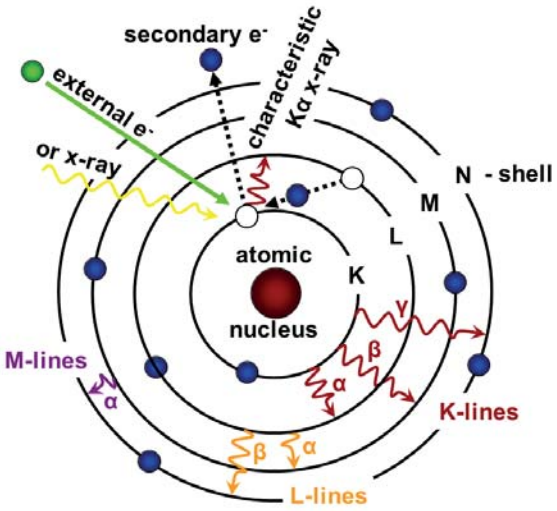


**Figure 3.3:** EDX principle: electrons leave the atom shell by external stimulation; the empty electron position is taken by an electron from a higher energetic shell; the energetic difference between the atom shells determines the characteristic X-ray photon (according to [111]).

obtained is much deeper as for SE and BSE.

If the released characteristic X-ray photon is absorbed by an electron of a higher energetic shell, the electron will be emitted with a characteristic energy that is defined by its original shell and the absorbed X-ray photon. Due to the penetration depth of these electrons at the relevant energy range of about 50 eV to 3 keV, the so called Auger electrons are coming from the ten topmost atom layers.

### 3.1.4 Electron backscatter diffraction

The SEM can also be used to analyse the crystal structure and composition of a sample by the electron backscatter diffraction (EBSD). The sample surface has to be prepared very well by grinding and polishing techniques, because this technique is very sensitive to any surface defects.

By scanning a surface the crystal type and its orientation can be determined by analysing the so called Kikuchi-pattern (Figure 3.4). These patterns are generated by inelastically and isotropically scattered primary electrons, providing an ideal divergent source inside the sample. These electrons are now scattered elastically for a second time on *all* lattice planes, featuring the *whole* crystal symmetry by the diffraction pattern. The only condition for the contributing electrons is, that the energy loss of the first inelastic scattering is only little compared to the primary energy of the beam [120].

The EBSD can be explained in analogy to the Ewald-construction [5] for X-ray scattering in a crystal. Using the Bragg condition in reciprocal space, introduced in subsection 2.5.1 Equation 2.30, $\vec{k} - \vec{k'} = \vec{G}$ with the reciprocal wavelength $\vec{k}$ of the isotropic incoming electron, the stray vector $\vec{k'}$ and the reciprocal lattice vector $\vec{G}$. In our case $\vec{k}$ has to be drawn *from* the origin of the reciprocal space -

[5] Compare to subsection 2.5.1.

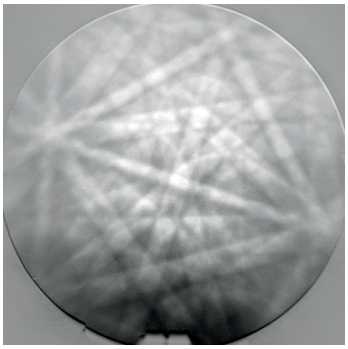

**Figure 3.4:** EBSD pattern of the TiAl$\alpha$ phase on a scintillator screen, imaged by the DigiView camera (EDAX, section 3.2), at 15 kV $U_{EHT}$: the so called Kikuchi pattern occurs by diffraction of inelastic strayed electrons on the lattice planes in the crystal.

or Brillouin-zone - , because the divergent source is given by lattice points *in* the sample. Therefore, the diffraction pattern would not change with respect to the crystal if the crystal is rotated in real space.
That is different to the Ewald-construction for X-ray scattering[6] techniques, by which this vector is drawn *from* the origin of real space *to* a lattice point which is defining the origin in reciprocal space.
In both cases a sphere with radius $|\vec{k}| = \frac{2\pi}{\lambda}$ determines the accessible diffraction reflexes, but for the ideally divergent electrons not point but line reflexes are generated because now the cutting edges of the respective Brillouin-zones with the sphere around the origin define the reflexes.
The pattern are visualised by a scintillator screen and a camera, while the analysing indexing is fully automated by computer software. For details on EBSD we refer to a textbook, as e.g. [120].

### 3.1.5 Introduction to FIB

Focused ion beam (FIB) is based on the same functional principal as SEM but is using ions, commonly gallium, instead of electrons. A review of focused ion beam technology and its applications in transmission electron microscopy is given by Sugiyama [130] or by the textbook of Giannuzzi [42].
A liquid metal ion source (LMIS, Figure 3.5) heats the metal to liquid state. By the extractor voltage the gallium is formed to a Taylor cone [131] on the tip of a Tungsten needle. Due to the decreasing radius at the Taylor cone head, the electric field becomes stronger until the ion evaporation begins.

Gallium with its low melting point, vapour pressure and reactivity offers the most proper characteristics to be used in a LMIS. Furthermore the gallium atom is heavy enough for ion beam milling, which is usually the main purpose of a FIB device. If necessary, the LMIS gallium emitter can be regenerated by additional heating. This will remove the oxide which deposed during FIB operation.

By the same principle as described in subsection 3.1.2 also SE imaging can be done with an ion beam, but using primary ions and not PE. Besides the significantly

[6] A short introduction to X-ray scattering is given in subsection 2.5.1.

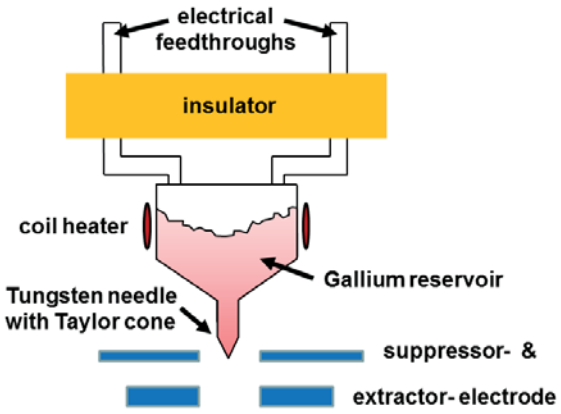


**Figure 3.5:** Simplified schematic liquid metal ion source (LMIS) with gallium (after [84]). The gallium is heated to the liquid state by coils, and the emission current of the Taylor cone is generated by the extractor tension.

increased SE emission, the interaction of the much heavier ions with the sample results in sputtering of neutral atoms or secondary ions as well as backsputtering of primary ions. The occurring ion - solid interactions are shown in Figure 3.6. Again also X-rays and Auger electrons are emitted, due to the effects introduced in subsection 3.1.3.
Some primary ions are implanted into the substrate material, causing lattice defects. As a rule of thumb a minimum penetration depth of the collision cascade into the substrate of approximately 1 nm/kV[7] can be assumed [42].

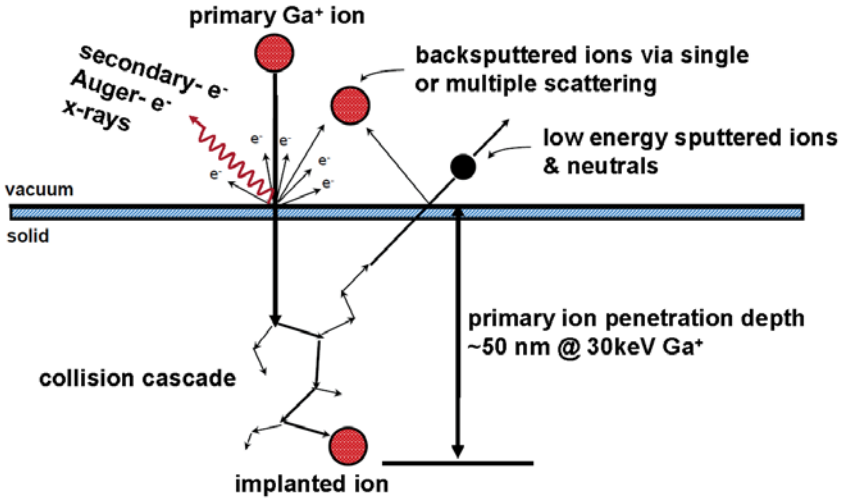


**Figure 3.6:** FIB induced ion - solid interactions in the sample, after [42].

The sputter rate of neutral atoms or secondary ions is always much higher than the implanted amount. Thus, a sample can be milled to desired micro scaled shapes, or a small structure can be processed out of a region of interest from the original sample for further investigations, as a pillar for SRnCT or a TEM lamella. TEM lamella preparation is commonly one of the main fields of FIB operation.

[7] accelerating voltage, or ion high tension $U_{IHT}$, of the FIB column

Such a lamella is prepared at different angles in several milling steps. The excavating first step is performed with relative high currents in the nA[8] range, with the sample surface perpendicular to the FIB. This is followed by the lift out and fixation to an appropriate sample holder using the obligatory micro-manipulator. Now the thinning can be performed by lower currents in the pA[9] range on both sides of the lamella. This happens at slightly over- and under- tilted positions with respect to the exactly perpendicular orientation to the FIB, in order to avoid a wedge like profile of the lamella by the Gaussian intensity distribution of the ion beam profile. The thinning by milling on the backside is performed until the FIB generated secondary electrons are visible to the SE-detector, i.e. the lamella becomes apparently transparent (Figure 3.7). The remaining thickness is then roughly about 50 nm, defined by the penetration depth of *Ga* ions at 30 kV (Figure 3.6).
By preparing a TEM lamella or a FIB cross section into the sample, the damage by the ion beam to the crystalline or amorphous structure of the specimen is always an issue. In order to avoid as much damage as possible the acceleration voltage can be decreased during the last polishing FIB milling steps. In Figure 3.7 a TEM lamella is shown, which was prepared at the crossbeam workstation Auriga in order to exercise a TEM lamella preparation and to compare the benefit of two different polishing currents. As a preliminary result no significant difference between the two currents 5kV:100pA and 3kV:50pA could be detected by the subsequent TEM investigation.

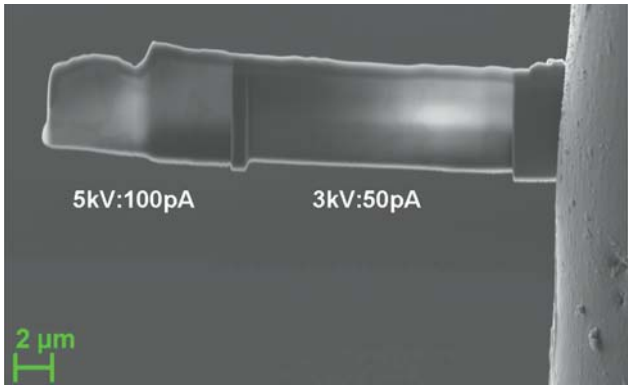


**Figure 3.7:** TEM lamella prepared out of a shear zone of a TiAl alloy, with protective platinum deposition on top, attached to a default *Cu* TEM-grid and finally polished by two different FIB currents: 5kV:100pA & 3kV:50pA. SEM image at 5 kV $U_{EHT}$, 5 mm WD, SE2-detector.

For further information on the topic of beam damage the publications from Ishitani *et al.* [64; 65], or Kato [70] are recommended.

## 3.2 The Auriga crossbeam workstation at HZG

The crossbeam workstation AURIGA 40 from *Zeiss* (Oberkochen, Germany) situated at the Helmholtz-Zentrum in Geesthacht (HZG, Germany) was used for

[8] nano Ampere
[9] pico Ampere

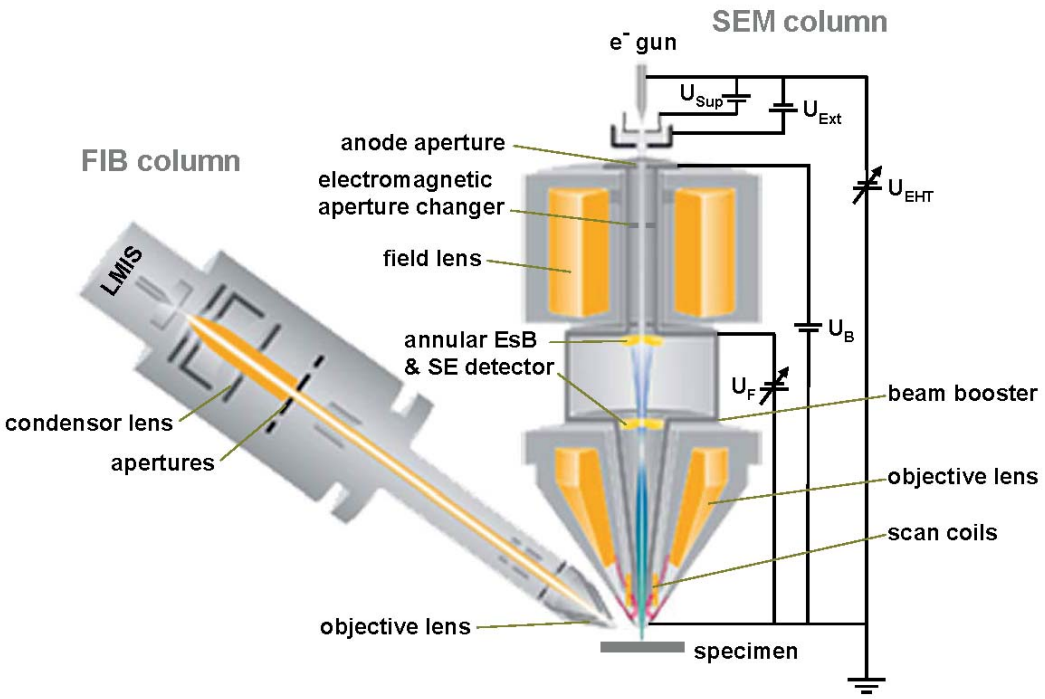


**Figure 3.8:** Scheme of the crossbeam workstation Auriga from Zeiss with SEM and FIB column [146]. Both columns are arranged in an angle of 54° to each other. Please refer to the text for detailed explanations.

this thesis and will be described in the following. It combines a SEM with a FIB column in one device as shown in Figure 3.8. The two columns are arranged in an angle of 54° to each other, the coincidence point of both beams is at 5 mm SEM working distance.
The Auriga is operated by the SmartSEM software (version V05.0403.00), from *Zeiss* (Oberkochen, Germany).
The sample stage enables - besides motion along the cubic axes $x, y, z$, the rotation axis $r$ and the tilt axis $t$ - eucentric sample positioning along the $m$ axis, which is perpendicular aligned to the tilt axis $t$. For samples of a thickness of up to 10 mm this eucentric positioning provides a stable positioning of the region of interest in the SEM *and* FIB image while tilting the sample.
The coarse stage motions and the entire inside of the chamber can be viewed by two CCD cameras. These cameras have to be switched off for EDX measurement, because the necessarily corresponding lights inside the chamber would affect the detector. The chamber is generally vented with nitrogen to avoid moisture by normal room air, which would affect the UHV performance. The nitrogen venting pressure should not exceed 0.5 bar in order to prevent damage to the EDX detector window and similar parts.

**Starting at the source**, the electrons are generated by a Schottky field emitter, using an fine etched tungsten tip which is implemented in the cathode. In case of

a Schottky field emitter the filament is heated by the filament current, supporting a very constant emission by the extractor voltage $U_{Ext}$, suppressing chromatic errors (section 3.1). To avoid thermoionic emissions from the shank of the field emitter, a supressor voltage $U_{Sup}$ is applied as well.
The Schottky field emitter needs UHV for operation. In order to keep the gun in operation and to preserve a constant emission, a valve separates automatically the chamber from the column when the chamber vacuum is not sufficient for microscopy operation. This valve is always used if no air lock can be used and thus the chamber has to be vented in order to change the samples.

The SEM column related *GEMINI*-concept from Zeiss affects a decreasing lens-aberration-coefficient with decreasing beam energy, enabling high resolution contrast also during low energy operation.
The so called beam booster effects an additional electrical potential downstream the anode aperture of $U_B$ = 8 kV to the electron beam in the column, since the high tension does not exceed 20 kV. This ensures that the beam is not disturbed by magnetic stray fields and minimises beam broadening. Before the electron beam exits the objective lens, an opposed electrostatic field again decreases the energy by 8 kV.
The standard aperture of the *multihole aperture changer* is 30 $\mu$m[10]. The aperture size determines mainly the probe current. The Auriga is equipped with 6 different apertures of 7.5 - 120 $\mu$m diameter, enabling a wide range of different applications. The electron high tension $U_{EHT}$ can be tuned in the range of 0.1 - 30 kV. Also at low energy operation of less than 1 kV this device enables high resolution of down to several nm, assuming ideal metallic samples. At 15 kV $U_{EHT}$ resolutions of about 1 nm [146] are possible.

The Auriga crossbeam workstation is further equipped with a **charge compensator** device that enables to operate SEM on non-conductive samples without sputtering. This is achieved by a nozzle which has to be situated as close as possible to the surface, blowing nitrogen on the scanned region.

The nitrogen is ionised by the incoming electron beam and the response electrons. The positively charged ions neutralise the negative charge in the surface of the sample. This suppresses charging effects and enables SEM imaging up to a much higher magnification than without. The beneficial effect on the imaging is shown in Figure 3.9: the distortion of the silk fibre is straightened and smaller features can be visualised. However, the charge compensator is not applicable during FIB operations due to the necessary better vacuum.

To enable analysis of a wide range of biological samples a Leica EM MED020 cryo system from *Leica Mikrosysteme* (Wetzlar, Germany) is present in combination with the Auriga. This device enables to freeze, slice or sputter biological samples if necessary, and enables the subsequent transfer into the Auriga chamber via air lock. For imaging of those samples by the Auriga, the stage has to be temporarily modified by a few Leica cryo parts, to enable a steady sample cooling

[10] aperture opening in diameter

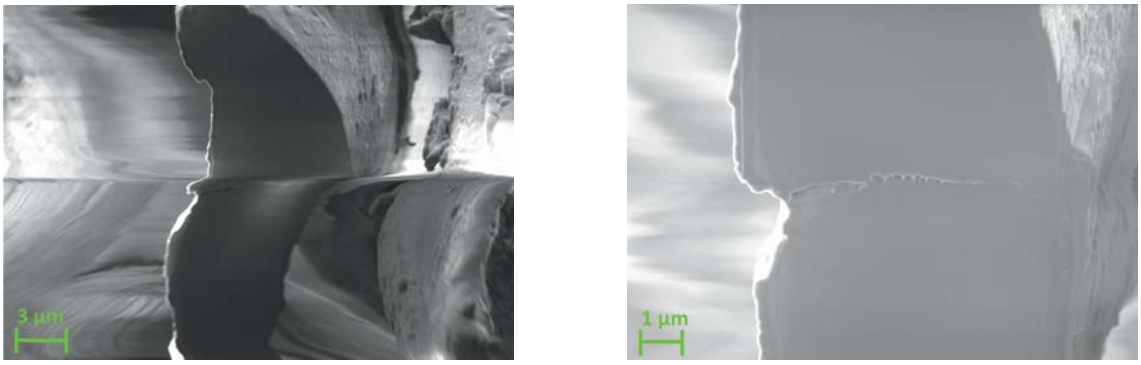


**(a)** without charge compensator (2 kV $U_{EHT}$, 4.5 mm WD, SE2-detector)

**(b)** with charge compensator (2 kV $U_{EHT}$, 4.6 mm WD, SE2-detector)

**Figure 3.9:** FIB prepared cross section in silk fibre.

at approximately -140 °C by liquid nitrogen.

### 3.2.1 Detectors

Several detectors are installed in the Auriga to obtain all important signals. An overview on the different detectors and the corresponding signals is given in Table 3.1.

To grab the backscattered electrons, a **BSE-detector** (backscattered electrons detector) consisting of four diodes is installed in the Auriga. For operation, the BSE-detector must be moved manually to the position directly under the column outlet of the SEM. The polarity of each diode can be set to plus or minus, featuring different contrasts.

A laterally placed Everhart-Thornley-detector (so-called **SE2-detector**) with a tunable sucking tension in the range between -250 and +400 V is the basic SE detector of the Auriga. It also provides a pseudo backscattered image at negative voltages showing pronounced topography, because all the low energetic and more diffuse

| detector | signal |
|---|---|
| SE2 | secondary electrons; topography |
| InLens | secondary electrons by $U_{EHT}$ of up to 20 kV; surface contrast |
| EsB | backscattered electrons (below 1.5 kV energy selective); material contrast at low energies |
| BSE | backscattered electrons; material contrast |
| STEM | transmitted electrons; requires thin specimen (approx. 50 nm) |
| EDX | characteristic X-rays; elementary composition |
| EBSD | diffracted electron patterns; crystallographic analysis |

**Table 3.1:** Detectors installed to the Auriga at the HZG and their recorded signals.

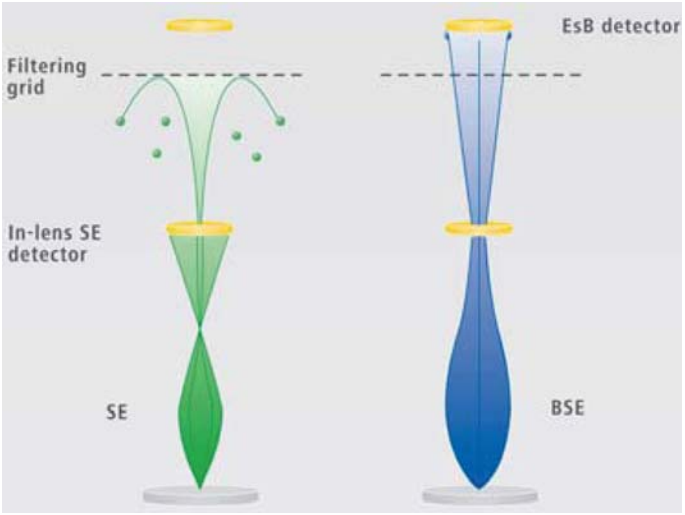


**Figure 3.10:** Function Principle of the InLens- and the EsB-detector. The lower energetic SE follow a different curvature than the BSE on their way upstream, sorted by energy to the InLens-detector [146].

SE are now repulsed and cannot contribute to the signal. Furthermore an **InLens-detector** is placed - as the name implies - at in-lens position behind the objective lens of the SEM column to catch vertically emitted SE (Figure 3.10). These are actively accelerated upstream by the described deceleration field for the primary electron beam of the beam booster. This InLens detector provides excellent surface contrast and high resolution, especially at low energies and short working distances. For geometrical reasons the SE2-detector mainly catches SEII while the InLens-detector catches SEI[11] [146]. Both detectors detect the individual electrons by a scintillator.

Upstream to this InLens-detector an energy-selective-back-scatter-detector (**EsB**) is situated, also at in-lens position, to provide a low energy BSE signal. A tunable filter grid with a maximum tension of 1.5 kV in front of this detector rejects the few lower energetic SE which passed the InLens-detector. Below an acceleration high tension of 1.5 kV the grid can be used to set the threshold energy to select the energy range of inelastically scattered BSE, enhancing contrast and resolution. The signal yield of this detector is very low, but it features unique and tunable material contrast at low energies.

To perform energy dispersive X-ray spectroscopy (**EDX**) the Auriga provides the EDX device Apollo XP from *EDAX* (Ametek GmbH, Wiesbaden, Germany). The Silicon drift detector (SDD) of Apollo XP enables an energy resolution of 127 eV. EDX at the Auriga is calibrated to a working distance of 8.5 mm.
The element composition of a certain spot, line or area on the surface can be determined quantitatively by EDX. For reliable values it is necessary to calibrate the measurement with a standard sample that provides almost the same elemental composition.
EDX mapping can be also used for semiquantitative measurements, if no standard sample can be provided for calibration, as e.g. shown in the section 5.1. Intensity

[11] SEI and SEII were defined in subsection 3.1.2

maps of each desired element on the surface can be obtained in parallel, i.e. a lateral intensity map of the respective regions of interest in the EDX spectrum.
The existing automatic drift correction of the Auriga was applied for mappings and all long term measurements in this thesis to guarantee image quality.

**EBSD** at the Auriga is provided by the DigiView detector, again from *EDAX* (Ametek GmbH, Wiesbaden, Germany). The detector camera is able to index diffraction patterns with a rate of up to 150 per second. Data acquisition and analysis is accomplished by the EDAX software TSL-OIM[12] for data-collection and -analysis respectively.

Furthermore, the Auriga provides also the possibility to perform scanning transmission electron microscopy (**STEM**). For this a special detector is installed on the SEM chamber, which has to be driven in manually for measurement. The present STEM sample holder must be used to obtain the signal below the sample, also providing the mounting of the default 3 mm *Cu* grids known from TEM. The sample must fulfil similar restrictions as a TEM sample regarding thickness and size, like e.g. a FIB prepared TEM lamella.

### 3.2.2 FIB apparatus

The crossbeam workstation Auriga is equipped with the Canion column from Orsay physics (Fuveau, France). The Canion is providing 7 different sized mechanically positioned apertures with diameters of usually 10, 30, 50, 100, 200, 400, and 600 $\mu$m to feature a variety of ion currents. The acceleration voltage, or ion high tension $U_{IHT}$, of the Canion column is by default set to 30 kV. Though also lower voltages are adjustable, especially to enable custom polishing currents.
The Auriga is using a gallium LMIS[13] for ion generation, which is the common FIB layout. The emission current is generated by the extractor tension, and is kept constant by an automatic regulation of the suppressor voltage (in analogy to the scheme of the SEM column in Figure 3.8). The FIB currents have to be adjusted by the user to the desired values if necessary [146]. The character of the individual LMIS defines the highest possible currents in the >10 nA range. Not all currents are possible with each LMIS.
To ensure a constant high quality of the desired FIB currents, they have to be readjusted frequently in current value (by tuning the condensor[14] voltage), aperture position, focus, stigmation and beam shift correction.
By using the 50 pA standard current for sample adjustments and determination of the milling region, an increased damage by the higher milling currents is avoided. However, the default use of the 50 pA current requires an adjusted beam shift correction of the milling current, i.e. by the beam shift correction the milling currents image exactly the same area as the standard 50 pA current does.

[12] orientation imaging microscopy (OIM)
[13] liquid metal ion source, introduced in subsection 3.1.5
[14] The value of the condensor voltage is inverse proportional to the FIB current value.

The FIB extends the surface limited SEM techniques to deep matter investigations. By combination of both techniques the structure of a fine polished FIB prepared cross section, up to a depth of several 10 $\mu$m, can be analysed by the SEM component.

The **gas injection system** (GIS) of the Auriga enables in combination with the FIB amorphous deposition of different materials as tungsten, platinum, carbon and an insulator material. Each of these materials is a component of a special precursor gas[15] that can be blown inside the SEM chamber onto the specimen's surface. To enable a deposition, the nozzles of the GIS have to be placed as close as possible to the surface of the specimen in order to gain a high gas concentration at the dedicated deposition region.
The deposition process itself takes place by decomposing the precursor molecules by the secondary electrons, which are emitted by the ion beam. The volatile by-products are pumped away while the desired material is deposited amorphously. The deposition layer contains about 10-20% implanted gallium and 10-20% implanted carbon from the precursor or residual contamination [147].
The deposition is essential for lift out procedures of FIB processed specimens as also for the attachment to adequate sample holders. Furthermore, it is useful to cover a region of interest - that is dedicated to FIB cross sectioning or similar - with a deposition in order to avoid FIB damage and curtaining. This curtaining would be induced by the beam deflecting on the edge of a bumpy sample surface and can be avoided by smoothing it with a deposition layer.
The GIS also enables etching by use of the installed fluorine or water precursor. Etching happens in a similar way as the deposition procedure: The precursor is decomposed by the secondary electrons, creating a volatile compound which is again pumped away while the chemical active part reacts with the surface. The etching can be used to increase the FIB milling yield and performance. It is dependent on the reactivity of sample and the active etching part of the precursor.
During the usage of the GIS the precursors and the corresponding nozzles have to be heated at individual temperatures to enable the gas flow. To guarantee a good performance of the GIS precursors the heating should be started some hours or even a day before the application is scheduled.

To move a FIB prepared specimen, as e.g. a TEM lamella, to an appropriate sample holder like a TEM grid, the **micro-manipulator** Autoprobe 200 from *Omniprobe*[16] (Texas, US) is installed to the Auriga. This device provides a long needle with a tip diameter of only some hundred nanometers. The needle can be positioned with an accuracy of 100 nm, in order to attach the FIB prepared specimen to it, by using the FIB/GIS technique. Subsequently the processed specimen is transferred to the sample holder and must be fixed to it, again by using the FIB/GIS technique. Some samples can also be welded by redeposition to the manipulator needle or a sample holder. For this a FIB current in the nA range should be used, dependent

[15] details can be found in [147]
[16] distributed by Oxford Instruments

on the involved materials.

Due to the wide field of different samples which are investigated with the Auriga, and especially to the FIB milling products, a **plasma cleaner**, Evactron 25 from *XEI Scientific Inc.* (Redwood City, California, US), was installed to restore the purity of the vacuum and thus the performance of the whole device. By partially venting the chamber with oxygen, or a gas mixture containing oxygen - as i.e. room air for the Auriga at HZG - this cleaner ignites a local plasma inside the chamber which generates highly reactive oxygen radicals. The radicals then react with the deposited contamination in the chamber, as on the walls, cracking them into volatile parts which are pumped away. During this procedure the Auriga turbo pump has to be switched off to avoid an overheating that would be affected by the partly vented chamber during plasma cleaning operation. In our case the carbon contamination was decreased by 57 % after 10 h plasma cleaning at 0.7 mbar and 14 watt on a sample composed of *Al* and *Cu*, as shown by EDX.

### 3.2.3 FIB tomography techniques

#### FIB-SEM tomography

Destructive **FIB tomography**, or serial sectioning, can be performed with the crossbeam workstation Auriga by cutting a volume of interest slice per slice with an appropriate FIB current. A sample is repeatedly milled with the FIB and each newly produced cutting face is imaged by the desired SEM detector signal. The 3D data set is then generated out of the 2D image stack by interpolation with an adequate software program. In our case the tomography software Avizo Fire from the *visualisation sciences group (VSG)* (Mérignac Cedex, France) was used.

Because of the possible high resolution of up to some nm by the SEM, FIB tomography can enable lateral structural information on a scale which cannot be obtained with conventional tomography methods [61; 62; 96]. Even the calculated resolution of the SRnCT experiment (section 2.4) cannot reach the resolution of this destructive 3D imaging technique. However, the FIB/SEM tomography technique is destructive, and if the experiment does not provide usable data there is no possibility for a second try.

#### 3D-EBSD

Another FIB tomography technique provided by the Auriga is tomographic crystal structure characterisation using the automated 3D-EBSD procedure [50]. For every slice the sample has to be initially moved to the FIB milling position, and subsequently to milling to the EBSD-scanning position.

For this the special 3D-EBSD sample holder from Zeiss has to be used, shown in Figure 3.11, as well as the 3D TSL-OIM collection software from *EDAX* (Ametek GmbH, Wiesbaden, Germany). For this, the stage has to be tilted to 17° during

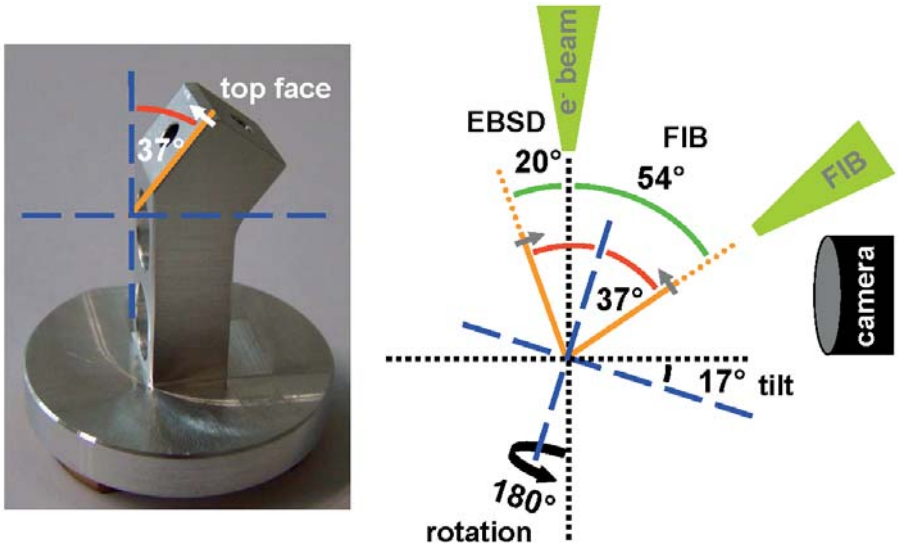


**Figure 3.11:** Auriga sample older for 3D-EBSD with 37° pre-tilt (left) and the corresponding working scheme (right): The stage has to be tilted for 17° to achieve an angle of 54° for FIB milling of the respective EBSD slice. Turning the rotation axis for 180° leads to the mandatory angle of 20° to the EBSD camera.

the whole process. Due to this pre-tilt of the sample holder, the position for FIB milling with the ion beam parallel to the sample surface - in order to process the next EBSD slice - and the EBSD position at 20° with respect to the SEM column are accessible by simply turning the stage rotation axis for 180°. This turning has to be done between every working step. Besides this only an additional positioning for the vertical $z$ axis of the stage is necessary. However, no tilt axis motion is needed to move into the respective next position for FIB or EBSD operation.
By this the obligatory drift correction, software has to do less corrections than for sample positioning with an additional movement of the tilt axis. The risk that the field of view is beyond the range of the drift correction software is therefore minimised.

## 3.3 FIB specimen preparation method for nanotomography at IBL

### 3.3.1 Modifications to the Auriga

The Auriga is supposed to prepare specimens for the nanotomography experiment at IBL, according to the requirements given in subsection 2.4.5. The described cylindric or pillar shaped specimens have to be processed out of a region of interest from the original sample, taken out and fixed onto an IBL sample holder (shown in Figure 2.14 and 3.12a).

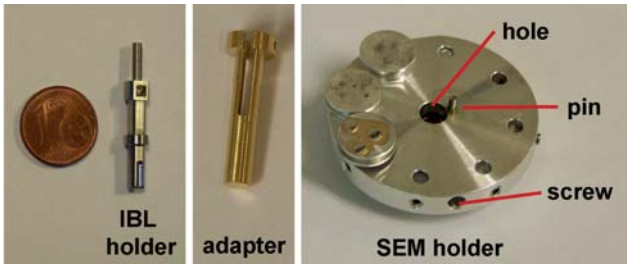


**(a)** IBL sampleholder with adapter for the hole in the modified SEM holder

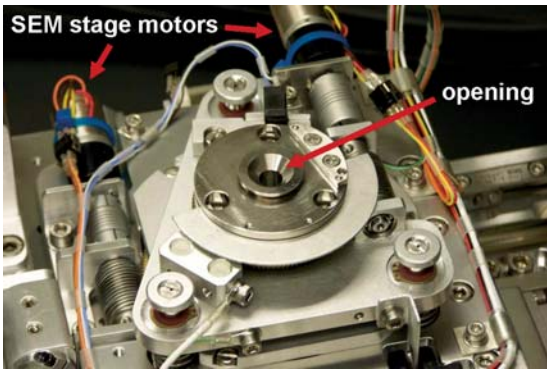


**(b)** Auriga stage with centre opening

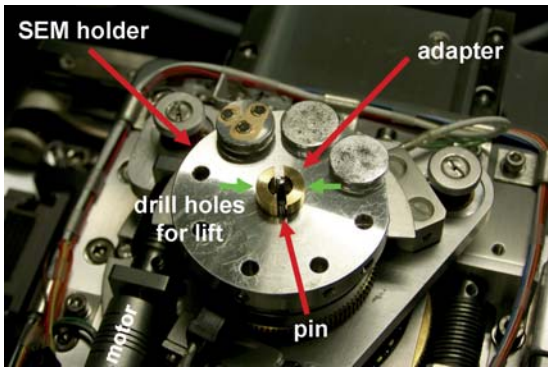


**(c)** Modified sample holder of the Auriga with adapter and IBL holder

**Figure 3.12:** Parts and modifications for adaption of the IBL sample holder to the Auriga. Figure part (a): the adapter for the IBL sample holder fits into the middle opening of the Auriga stage (Figure part (b)). For this the sample holder of the Auriga was modified by a hole in the middle, a direction defining pin and a fixation screw (Figure parts (a) and (c)).

The Auriga SEM sample holder had to be modified to adapt the IBL holder. An opening in the Auriga stage (Figure 3.12 part (b)), which cannot be modified, provides a diameter of 6 mm, and therefore allowed to design an adapter shell for the IBL holder with a basic diameter of 5 mm (Figure 3.12 part (a)).

The Auriga sample holder itself was extended by a middle hole which can take in the adapter, and a pin to define the position of the adapter with respect to the installed fixation grub screw (Figure 3.12 part (a) and (c)). To transmit the pressure from the screw also to the IBL holder itself, the adapter shell has two slits, splitting the upper part into two halves.
Because of the hole in the stage the shell could be designed high enough, so that the top of the contained IBL holder is still in range of the $m$ axis to enable eucentric positioning (compare section 3.2). This crucially facilitates the FIB specimen production for nanotomography.

The Auriga holder has to be pushed in horizontal direction to mount it upon the stage. Because of the length of the IBL holder it reaches - and therefor the adapter too - beyond the Auriga holder into the mentioned stage opening. Hence, it is

mandatory to insert the shell with the IBL holder subsequently to the mounting of the Auriga holder.
To enable a safe lift out of the IBL holder inclusive specimen pillar on top, the adaptive shell was designed with a drill hole on both sides of the top - where no slit is - to enable insertion of a small tool driver or similar to lift it initially from the Auriga holder. Then it can be grabbed carefully by hands.

### 3.3.2 Specimen processing for SRnCT

In the following the specimen preparation method by FIB for the nanotomography experiment at IBL is introduced including the optimised parameters which were found during the general development of this method. The whole process is similar to the fabrication of a TEM lamella.

When the **region of interest** is chosen by appropriate SEM techniques, as e.g. the use of material contrast by the BSE-detector, the original sample has to be tilted by the stage to 54° in order to enable a perpendicular milling to excavate the pillar out of the material (Figure 3.13a and 3.13b).
The structure itself is excavated by several **FIB milling** steps from the bulk material, in minimum one circular and two trapezoid shaped ones. The trapezoid ones enable a cut off from both sides. This saves time during the excavation procedure, because for geometric reasons a cut off from only one side would effort a deeper circular milling. Additionally, an excavating milling with increased depth consumes more time, caused by the higher energy which is needed for the sputtered particles to leave the hole.
Depending on the individual material and whether the depth milling is performed only in one or very few layers, redeposition leads to a wedge like shaped trapezoid excavation hole. If this does not restrict the cut off, this is acceptable. In contrast, the circular milling has to be performed in at least 10 layers to guarantee a free standing pillar without wedge shaped redeposition.
For the excavating FIB mill steps, currents of at least >10 nA should be used.

For an optional partially cut off from the back side, the stage should be tilted as close as possible to 0° or even a slight negative tilt. The vertical milling position is dependent on the previously chosen trapezoid depth on the front side. In any case it should be tried to cut off as flat and deep as possible, first partially from the back side and then finally from the front side. Before the second and final cut off, the GIS operation has to be prepared, because it is mandatory to attach the pillar by the FIB to the micro-manipulator needle tip before the final cut off is done. Otherwise the pillar would be charged by the electron beam and attracted by the SE2-detector's sucking tension, or another source of attraction, and would get lost.

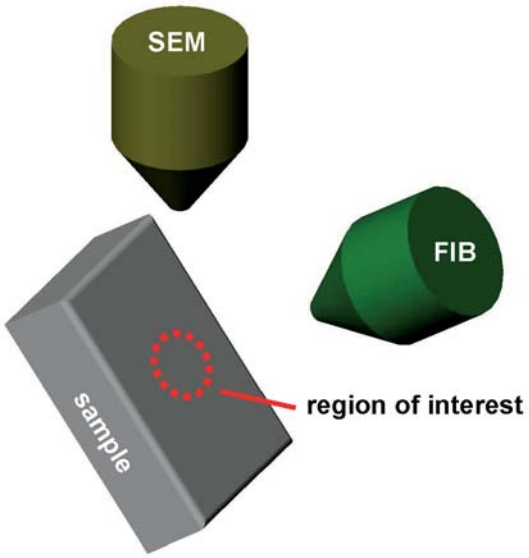


**(a)** Sample with region of interest

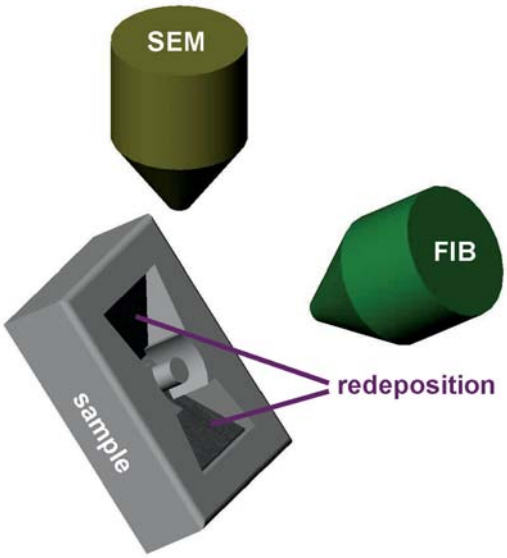


**(b)** FIB processed pillar including the region of interest milled at 54° stage tilt

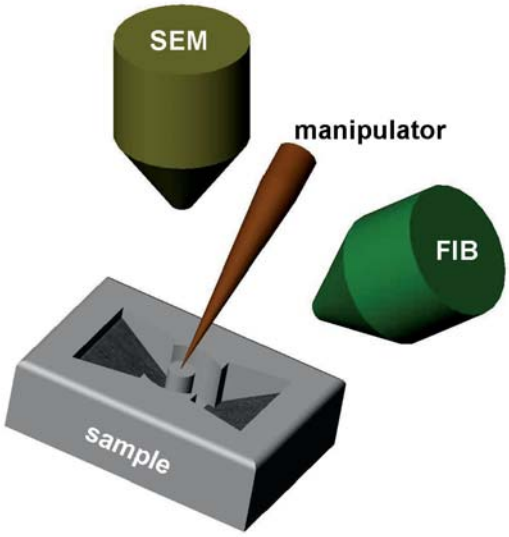


**(c)** Pillar in contact with the manipulator at 10° stage tilt

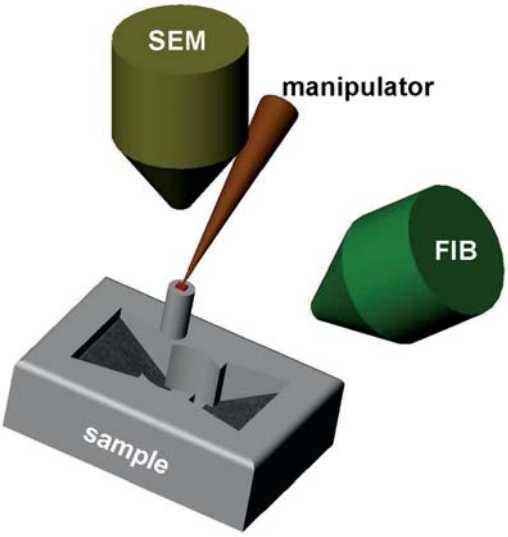


**(d)** Pillar lift out subsequently to attaching it to the manipulator

**Figure 3.13:** Schematic FIB specimen preparation procedure for nanotomography at IBL until the lift out of the specimen pillar. The attachment to the IBL sample holder is not shown here, but this follows generally the same steps as Figure parts c and d but in opposite order.

The nozzles of the **GIS** must be driven manually to the surface of the specimen, mainly in horizontal motion, to the closest possible position. The predefined positions of the automated GIS insertion are calibrated to 54°. At any less tilted position than 54° the automated insertion of the GIS cannot be used, since the GIS nozzles would crash into the surface.
The yield of gas used for deposition, compared to the gas fraction which is just pumped away, is greater the closer the nozzles are positioned to the attachment point. If the stage tilt value is very low and the sample is flat, the distance of the GIS nozzles to the attachment point must be increased for geometry reasons. Due to this, and dependent on the particular sample geometry, it was experimentally derived that the tilt at final cut off position should be about 10° (Figure 3.13c and 3.13d).
The GIS deposition currents should be roughly chosen by the ratio

$$\frac{5\,pA}{\mu m^2}, \tag{3.5}$$

with respect to the deposition area in $[\mu m^2]$. The deposition rate is generally lower at stage tilt angles where the sample surface is not perpendicular to the FIB.

Furthermore, the Auriga provides a so called **touch alarm**. This would immediately stop any motion by the motor driven SEM devices if it is activated by a touch of the electrically separated stage to the surroundings, like e.g. the outlet of the SEM column (refer to Figure 3.14). This would necessarily happen during the following step, when the processed specimen is taken out by the manipulator.
Caused by a possible overtravelling of the stage motors in the moment when the alarm would be activated, some motion steps could be lost and the defined continuation of the operation is endangered. Therefore a stage initialisation would be necessary, which is again impossible without sample detachment and loss during a lift out situation. Hence, the so called specimen current monitor, which enables the measurement of stage currents and thus disables the touch alarm function, must be always switched on during lift out operations. The operator has to be

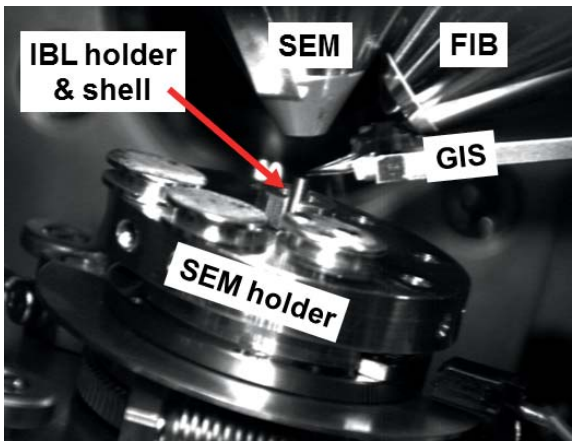


**Figure 3.14:** CCD view inside the chamber of the Auriga while the stage is tilted at 15°, the GIS is in operating position and the manipulator (not visible, too small) is in touch.

very careful now, at every movement of stage, GIS and manipulator. No motion would be stopped automatically in case of a touch, and also no alarm would warn the operator!

The FIB processed pillar is now attached to the **manipulator** needle, followed by the **final cut off** from the sample. The stage tilt has to be kept constant at the previously chosen value of e.g. 10°, while the $x, y, z$ axes are moved to the position of the prepared IBL sample holder in the very centre of the Auriga holder.

The attaching of the specimen pillar to the IBL tomography holder follows the same steps like Figure 3.13 (c) and (d) but in opposite sequence: The specimen pillar is moved to the IBL holder and is attached to it, again by FIB using the GIS. Now the attachment point of the manipulator needle to the pillar is milled away by the FIB, cutting off this interim transport connection.

Subsequently the specimen should be attached to the holder at two more contact points, if available, to guarantee a strong connection. This is important since it occurred in some experiments that samples moved while they were exposed to the X-ray beam if they were only attached at one contact point.

### 3.3.3 Specimen transport

After venting the Auriga chamber the specimen on top of the IBL sample holder has to be taken out very carefully. Due to the drill hole in the top of the shell, mentioned above, the shell should be lifted slightly for some millimetres with an appropriate tool. Now the shell containing the IBL sample holder can be easily grabbed by fingers, without touching the very top and destroying the FIB processed specimen. The IBL holder itself then has to be grabbed with tweezers, and be moved to a safe transport box, as shown in Figure 3.15, and be transported to the IBL (DESY).

**Figure 3.15:** A possible transport solution made from an SEM cathode box for FIB processed specimen on IBL holders to ensure a safe transport to DESY. The IBL holders are easily accessible by tweezers and fixed by grub screws. The box should be additionally wrapped in something soft and vibration absorbing for transport.

# Chapter 4

# Applications: Porous Ti-6Al-4V implant material for cell ingrowth

Due to the necessity of fast healing and mechanical stability there is still a need for further development of implants. The characteristics of titanium alloys regarding bio-compatibility, mechanical properties and corrosion resistance make them a very suited material for orthopaedic or dental implants. Since the late 1930's this led to the natural choice of titanium or related alloys as major material for implants, like e.g. bone screws, hip replacements or parts of artificial heart valves. Regarding the still proceeding increase of human lifetime, it becomes necessary to develop long lasting implants to avoid multiple revision surgeries. To enable a proper adaption and long lasting stability of the bone implanted devices, it is essential that the Young's modulus[1] of the implant is similar to the one of cortical bone [125]. A further improvement of stability can be achieved by bone-cell ingrowth into the implant [20]. It is known that the topography of prosthetic devices can directly influence the cellular response. Thus, assuming a direct connection between material pore size and bone formation [88], it becomes necessary to find the most proper porosity, enabling cell migration and *in vivo* blood vessel formation.

Metal injection moulding (MIM) provides the advantage of processing net-shaped and rather complex parts at comparably low production costs, as well as adjusting the porosity by using different sizes of metal powder or tuning the sintering temperature. This includes also *Ti* alloys [30].
Control of the porosity gradient allows to mimick the structure of natural bone. This should be ideal to enable ingrowth of new bone tissues and vascularisation. Moreover, the mechanical properties of porous titanium are very close to those of natural bone. This characteristic is mandatory for osteoinduction.

Four different porous sample categories were produced by A. Deing within the scope of his thesis, by using different sized *Ti*-6*Al*-4*V*[2] powders. Those were

[1] also known as tensile or elastic modulus
[2] composition in mass percent

colonised with cells in order to analyse the cell ingrowth and response by FIB/SEM and common computed X-ray tomography. These results were jointly published with A. Deing *et al.* [25], and will be part of his thesis as soon as accomplished.
Furthermore, as exclusive part in the scope of the present thesis, the confirmation of the osseous tissue colonisation (osteoblast-like cells) inside the porous material was considered by SRnCT, in other words to see single cells inside the artificial bone matrix.
The main challenge for tomography on those samples is the extremely small attenuation of X-rays by cells compared to the highly absorbing *Ti*, in contrast to explanted porous samples in which mineralised bone has a sufficient attenuation [68; 5]. To overcome this, the cell-attenuation has to be increased by incorporation of metals, as well as using a small sample diameter of the *Ti*-6*Al*-4*V* substrate material, to enable the usage of a low X-ray energy.

## 4.1 The porous substrate material

By using four different powder compositions, named according to their individual particle diameter range "Small" (<45 $\mu$m), "Medium" (45-63 $\mu$m), "Large" (125-180 $\mu$m) and "Mix" (90% 125-180 $\mu$m + 10% <45 $\mu$m), four different porosities were tailored by MIM for tomography experiments. The powders are composed of spherical, gas-atomised *Ti*-6*Al*-4*V* grade 23 powders, purchased from *TLS Technik Spezialpulver* (Bitterfeld, Germany).
Besides special sample geometries for tensile and compression testings, also sample discs were fabricated for cell colonisation experiments, described in detail by Deing *et al.* [25].
The **MIM process** starts with the production of the so called feedstock, obtained by merging the desired powder composition with the binder under argon atmosphere. The binder is composed of paraffin and polyethylene derivates.

**(a)** pre-sintered 30 mm disc together with subsequently hand punched 10 mm discs

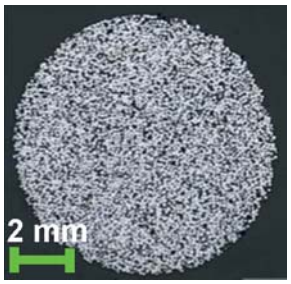


**(b)** 10 mm disc made of Large powder

**(c)** 10 mm disc made of Mix powder

**Figure 4.1:** Manually produced pre-sintered sample discs (figure part (a)). Light microscopy images of sintered discs in Figure part (b) & (c).

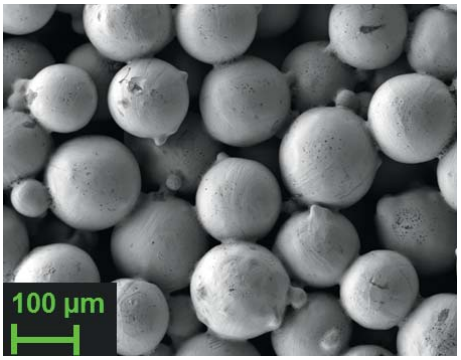


**Figure 4.2:** SEM image of the newly sintered Mix substrate material (3 kV $U_{EHT}$, 3.3 mm WD, SE2 detector).

The feedstock is pressed into the favoured tool form, enabling manifold material shapes, in our case a plate like shape of 30 mm diameter and 2 mm thickness. Out of these plates the final plates with a diameters of 10 mm and 3 mm (see Figure 4.1 part (a) were manufactured using a hand punch.

The chemical debinding of the samples, to extract the paraffin, was done in hexane in a debinding furnace at 450°C and 600°C, each for 1 h, under argon gas flow. The subsequent sintering was performed at 1100°C and 1300°C for 2 h under a vacuum of $10^{-5}$ mbar in a cold-wall furnace with molybdenum shieldings and tungsten heater(XVAC, *XERION Ofentechnik GmbH*, Freiberg, Germany).

### 4.1.1 Material characterisation by tomography

The porosity was characterised on the 10 mm sample discs by computed micro-tomography ($\mu$CT) in cooperation with A. Deing. For this the laboratory Phoenix X-ray tube system Nanotom (*GE Sensing & Inspection Technologies GmbH*, Hurth, Germany), equipped with a tungsten X-ray source and a 2304 x 2304 pixel detector was used. It was found that the present voxel[3] resolution of 12 $\mu$m was too coarse to analyse the pore sizes in "Small" and "Medium".
The experiment parameters were set to 140 kV source voltage under usage of a 0.5 mm copper filter, 50 $\mu$A source current for Large and 45 $\mu$A for Mix, with an exposure time of 1000 ms (Large) and 1250 ms (Mix). Of both sample porosity types four discs were imaged.
Image reconstruction was accomplished using the software DatosX Reconstruction 1.5 (*GE Sensing & Inspection Technologies GmbH*, Hurth, Germany), while the 3D image data analysis was performed by the myVGL 2.1 software (*Volume Graphics GmbH*, Heidelberg, Germany) and by the MAVI V1.4.1 software (*Fraunhofer-Institut für Techno- und Wirtschaftsmathematik*, Kaiserslautern, Germany).

The analysis of the tomographic data of the sample discs from Mix and Large by the myVGL software have revealed interconnected pores, through which air and water can pass (pore network, Figure 4.3). Thus, the sample has an increased specific surface area compared to an ordinary titanium plate. The pore network

[3]volume data unity, in analogy to a 2D pixel

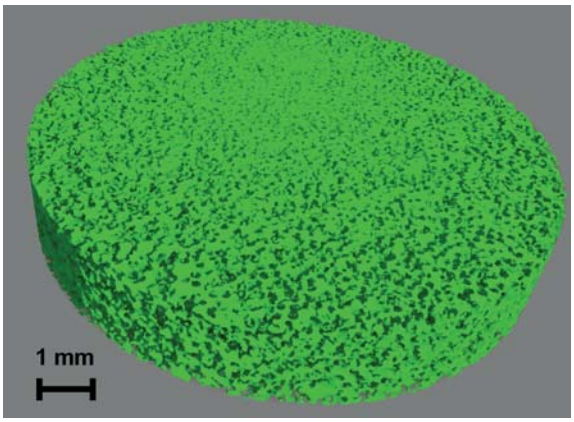


**Figure 4.3:** Tomographic reconstruction image of the network in the porous *Ti*-6*Al*-4*V* Mix material, sintered at 1300°C (lab CT device, compression: binning 2); the pore-network appears green while the material is blanked out.

volume of Mix represents 29.2 ±0.6% and of Large 34.1 ±0.5% from the whole sample disc volume.
The surface to volume ratio of the porous network was calculated to estimate the network's diameter. This ratio is namely 6.83 $\mu m^{-1}$ in average for Large, sintered at 1300°C, and 7.65 $\mu m^{-1}$ for Large sintered at 1100°C. For the Mix samples this ratio is slightly lower with 6.45 $\mu m^{-1}$ in average for 1300°C, and 6.49 $\mu m^{-1}$ for 1100°C, most likely caused by the 10% <45 $\mu$m powder faction which is filling up pore spacings. The noticeable difference of this ratio between the two different sintering temperatures on the Large material is probably due to the increased shrinking of the sample at higher temperature. The volume to surface ratio difference is not observed at the Mix material, which could be explained by the approximately 5% lower pore volume fraction, caused by the additional small particles that possibly avoid shrinking by providing more contact points. In other words, the small particles in the Mix material are suspected to stabilise the bigger ones.

By related investigations regarding tensile strength, yield strength and elongation for Large and Mix, the 1300°C fraction showed the better values. "Small" and "Medium" showed a Young's modulus close to those of bulk *Ti*-6*Al*-4*V*, and are thus applicable only for conventional implant devices.
Altogether, the Young's modulus for the Large and Mix samples at 1300°C is close to that one of bone, while the remaining mechanical properties make these materials pertinent for less load-bearing implant applications such as smaller bone defect corrections [25].
Therefore, only the samples of Large and Mix at 1300°C sintering temperature were used to characterise the size of the pore network on the uncompressed data (binning 1) by the MAVI software, by using the implemented granulometry tool. For this the data had to be binarised by setting a threshold to the grey values of the tomography, that distinguishes between air (i.e. pore) and *Ti*-6*Al*-4*V* material. Subsequently a "ball"-shape-based opening was performed on the binarised foreground voxels (i.e. material), which is smoothing the boundaries and is thus resulting in a more true data-set.
The subsequently performed granulometry links every voxel to an imaginary

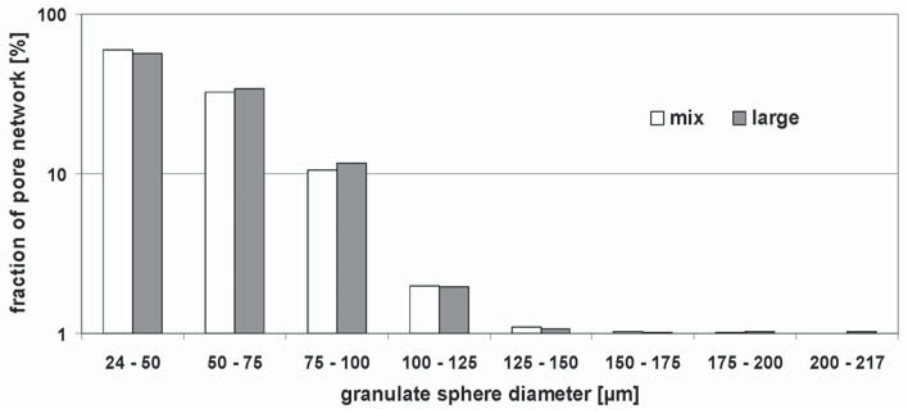


**Figure 4.4:** Average frequency of voxels indexed to the respective sphere shells (see text); obtained by the MAVI granulometry tool on the fractions Large and Mix of the 1300°C samples.

biggest sphere shell, that would still fit into each particular place of the pore network. The voxel assignment to the respective shell diameters of the four samples from Large and Mix at 1300°C is shown in the histogram in Figure 4.4.

### 4.1.2 Phospholipid coating

To afford a fast healing, i.e. to increase the implant osteointegration, a phospholipid coating (POPE, 1-palmitoyl-2-oleoyl-sn-glycero-3-phosphoethanolamine from *Avanti polar lipids inc*, Alabama, US) was applied. POPE is essential for cytokinesis [32] and is found in minor amounts in erythrocyte membranes. POPE covered metallic Ti alloys showed an increased osteogenic differentiation to human cell lines, while the number of bacteria was significantly reduced [139; 140]. By current *in vivo* studies with rats no inflammatory reaction could be found to those coatings [74].
The coating process itself is quite easy, as the dissolved POPE is simply dropped on the surface (details in section B.2). While the solvent evaporates, the POPE forms a self-organised phospholipid multilayer, mimicking a biomembrane by which the surface recognition of surrounding cells is improved.

The generated multilayer is of nanometer ranged variable thickness. For such a thin, homogenous and even coating, the direct detection by SEM imaging is impossible. The detection by EDX using the carbon or phosphate signal is not possible too, due to the homogeneity of the coating, the low amount of *P*, and the usually present carbon contamination of surfaces especially on biological samples.
To prove exemplarily the presence of the applied POPE coating, five mirror polished titanium samples were coated with a POPE solution using the described evaporation technique. The POPE was added by a varied amount of gold labelled DPPE (dipalmitoylphosphatidyl ethanolamine - nanogold from *Nanoprobes*,

NewYork, US).
The artificial amount of gold in the homogeneous coating was then detectable with EDX by the M-shell signal of the *Au*-atom. On each sample a 2 mm × 2.7 mm region, chosen as large as possible, was scanned by EDX and the resulting spectrum was quantified (Figure 4.5).
The comparably increased amount of the 0.5% coating, could be caused by a thicker phospholipid multilayer at the EDX scanning region.

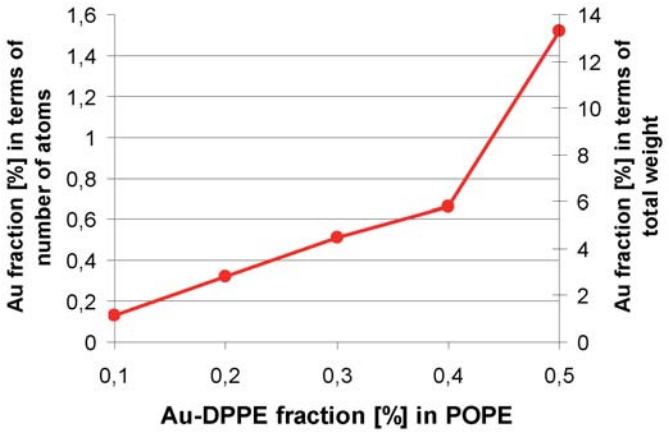


**Figure 4.5:** Proof of the phospholipid coating by EDX ($U_{EHT}$: 6 kV). Gold amount in atom and weight percent by detecting the M-shell signal of the atom, related to the entire signal of the scanning region.

## 4.2 Cell colonisation

Both sample types Large and Mix, including both sinter-temperature fractions of 1100°C and 1300°C, were used for the following cell colonisation investigations, since the sinter-temperature is affecting no difference to cell colonisation. Previous to cell colonisation the samples were cleaned by several ultrasonic treatments in different solvents, followed by autoclaving for 20 min at 121°C (Systec VE-150, *Systec GmbH*, Wettenberg, Germany) [25]. To gain enhanced information on cell proliferation regarding POPE, all samples were manufactured in pairs, as control and POPE coated ones.
To mimic osteointegration the osteoblast cell model Saos-2 (sarcoma osteogenic), a non-transformed cell line derived from a primary osteosarcoma from *European collection of cell cultures* (ECACC, Salisbury, UK) was selected.
Prior to deposition onto the porous substrate the cells were incubated for two days either with *myristic-acid covered iron-based nanoparticles* (synthesized at the *Laboratory of Magnetic Fluids of CFATR*, Timisoara, Romania) [2] or with *Eu* (europium(III) chloride hexahydrate) from *Sigma-Aldrich* (Missouri, US), in order to increase the attenuation of the biological matter for the planned tomographic experiments. The complete sample preparation protocol can be found in the appendix section B.3. The *Fe*-based nanoparticles are already known from another research topic, where it was tried to affect glioblastoma cells destructively by this

nanoparticles [2]. Glioblastoma cells[4] are typical malicious brain-cancerous cells. After two days culture in growth medium the samples were stabilised for SEM as well as for SRnCT with $OsO_4$[5], dehydrated by an alcoholic row using isopropanol and were supercritical dried in order to maintain the cell natural shape and stability under vacuum conditions.
Besides the described incorporation of *Fe* and *Eu*, the obligatory osmiumtetroxide (*OsO*4) fixation stain is now in charge to contribute additionally to the cell attenuation regarding SRnCT.
Supercritical drying by $CO_2$[6] was performed with a Leica EM CPD030 from *Leica Mikrosysteme* (Wetzlar, Germany) (the detailed procedure is given in section B.1).

[4] As proof of principle a FIB tomography on a single glioblastoma cell is given in Appendix C.
[5] osmiumtetroxide
[6] $CO_2$ critical point @ 73,9 bar and 31.1 °C

## 4.3 Cell ingrowth investigation by SEM techniques

For a general and detailed SEM pre-characterisation of attenuation enhancing stained cells, the 10 mm sample discs were used, with the two equally suitable substrates Large and Mix. The samples were prepared according to the previous section, while an overview on all samples of this row is given in subsection B.3.1.

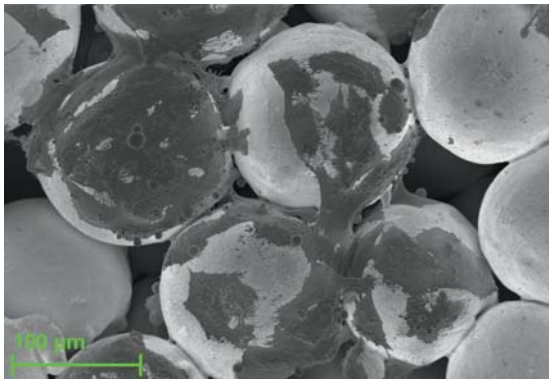


**(a)** Saos-2 cells on *mix* substrate; sample #24

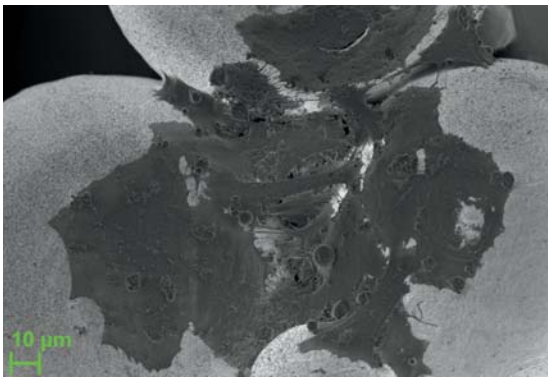


**(b)** The cells are also bridging adjacent particles; sample #11

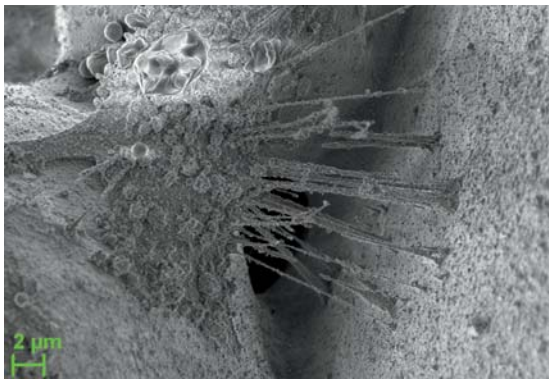


**(c)** Bridging "arms" of a cell; sample #5

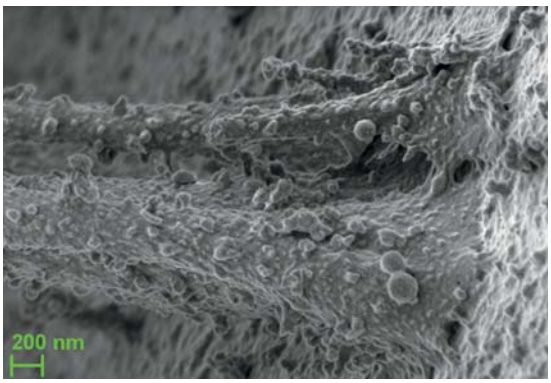


**(d)** "Foot" of a cell arm with a resolution of approximately 3.5 nm; sample #5

**Figure 4.6:** Low voltage image of Saos-2 cells on the sintered *Ti-6Al-4V* Mix-material, at 0.7 kV $U_{EHT}$, 1 mm - 3 mm WD, InLens-detector.

As a first step, the cell proliferation on the surface of the samples was imaged, revealing strongly varying amounts of cell colonies, even if the respective cell seeding amounts of the samples are taken into account. The Saos-2 colonies crowded the free surfaces of powder particles as well as the pore regions (Figure 4.6 part (a) & (b)). Especially the POPE coated samples showed very well adapted, effused cells, which spread their connection points or "arms" over very long distances. Even some of the not POPE coated samples showed this cell-arm behaviour, while the cells themselves effused usually not that strong (Figure 4.6 part (c)). One of the cell-arm's "feet" was imaged at high resolution to prove the

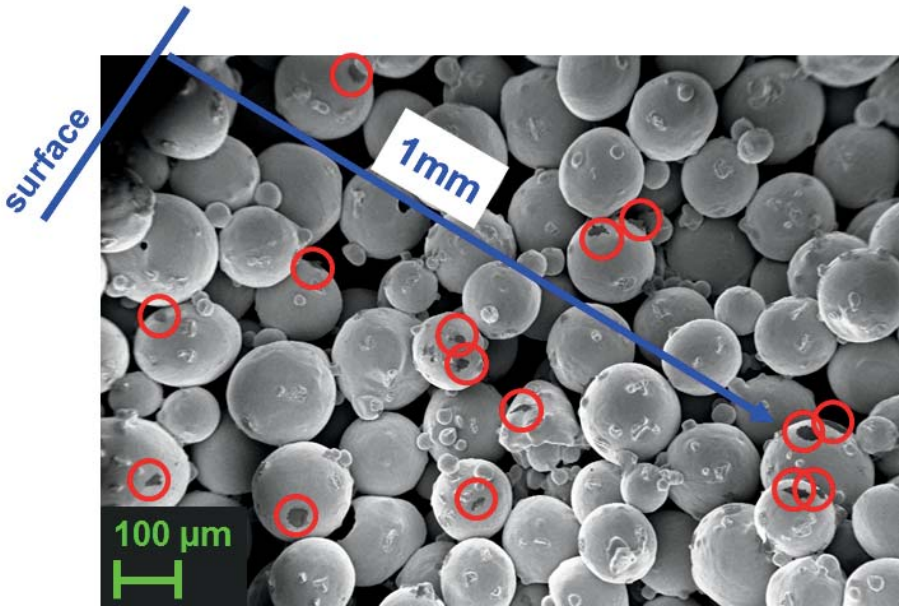


**Figure 4.7:** Cross section of broken sample disc #7. Cells, encircled in red, are distributed everywhere inside the porous material, even till the middle of the 2 mm thick disc. SEM Image at 0.7 kV $U_{EHT}$, 3.3 mm WD, InLens-detector.

performance of the Auriga on soft matter, Figure 4.6 part (d).

To verify that cells do not only grow on the surface of the material but are also colonising the porous network inside, four samples that showed already cell colonies on the surface, in equal parts with and without POPE, were broken by using grippers and investigated by SEM along the cross section. In this way a general internal cell distribution was detected in all samples, mostly by single cells (see Figure 4.7). Cell colonies like imaged on the surface were not present. Nevertheless, this doubtlessly proved the permeability of the porous network for cells, as well as the supply for their nutrition by the obviously occurring diffusion of growth medium through it.

### 4.3.1 SEM imaging of the phospholipid coating

During low acceleration voltage investigations at $U_{EHT}$ = 0.7 kV of the previously described broken sample discs, the remains of a cracked coating were found. This coating could be imaged at several places on both cross sections of the POPE covered samples #48 and #32 (Figure 4.8 part (a)). By these SEM images it is obvious that the elsewhere homogeneous coating became conspicuous by breaking the connection points of the adjacent powder particles, which cracked and peeled the coating too. The detected homogeinity of the coating makes it highly possible that it is a POPE multilayer.

This POPE suspected, damaged coating was found mostly in the upper half of the two broken cross sections. An average EDX area scanning on those regions

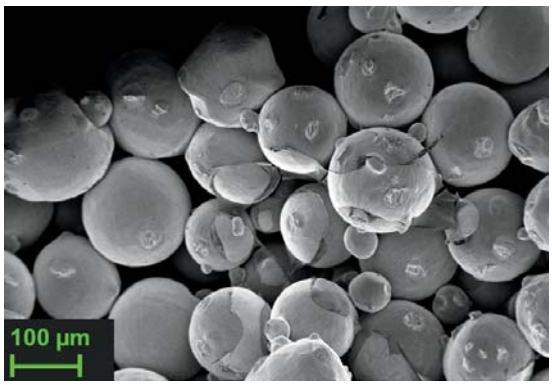


**(a)** Peeled coating at 0.7 kV $U_{EHT}$, 3.4 mm WD, InLens-detector

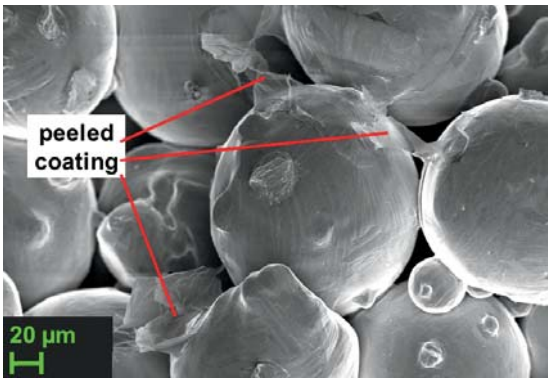


**(b)** EDX mapping region at 3 kV $U_{EHT}$, 8 mm WD, InLens-detector

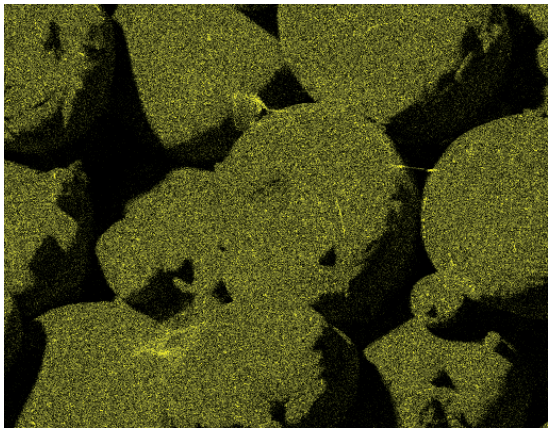

**(c)** Phosphorus mapping (K-shell peak)

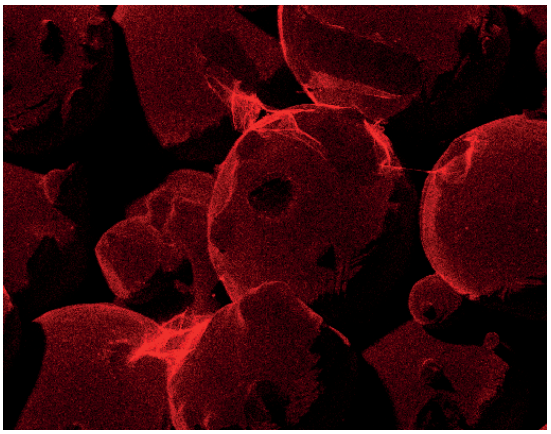

**(d)** Carbon mapping (K-shell peak)

**Figure 4.8:** Broken & peeled coating (figure part (a)). EDX mapping to prove POPE covering (at 3kV $U_{EHT}$) by the presence of phosphorus and carbon on a region of broken coating (figure parts (b) - (d)). All images taken from sample #48

revealed that the coating must consist of *C* (carbon) and a little amount of *P* (phosphorus). To assign this comparatively light elements *C* and *P* to the composition of the coating, a low energy EDX-mapping at $U_{EHT}$ = 3 kV was performed for the respective regions of interest in the EDX-spectrum, in an area featuring this described, slightly peeled coating (Figure 4.8 parts (b) - (d)). At 3 kV the peeled edges of the coating appeared with less contrast and are rather transparent than by 0.7 kV. However, a further decrease of the energy would have made the EDX measurement impossible, due to the necessary threshold of excitation energy, which has to be the double energy of the K-shell X-ray photon. On the other hand, the energy was already high enough to observe a change of the shape of the peeled coatings by appearing like slowly melting.
By the increased colour contrast at the peeled edges of the coating in the mapping images it is clear that the coating is definitely made out of *C* and also some amount of *P*. An orientation dependent effect on the value of the EDX signal can

be neglected. If there would be such an effect, the peeled coating on the right edge of the shadow of the middle sphere of Figure 4.8 part (d) must be in a significantly lower intensity than the other peeled coating on the left. A quantification by EDX in the present case would be again senseless, since no reliable standard sample could be prepared to enable the necessary calibration of such a thin coating.

## 4.4 Incorporation of Fe nanoparticles by cells

The major obstacle for tomomgraphy on cells in a metallic substrate is the higher attenuation to X-rays of metal compared to the biological matter. As already mentioned in section 4.2, a new strategy was applied to increase the attenuation of the cells which are embedded in the titanium substrate material: incorporation of iron-based nanoparticles, naturally uptaken by viable cells.

The presence of the main two attenuation enhancing elements *Eu* and *Fe*, as well as their affiliation to the cells, could be qualitatively detected by EDX, while the distribution of the *Fe*-based nanoparticles was investigated in more detail. The nanoparticles can not be imaged by SEM as single particles, due to their size of only several nanometers and the contour-less, smooth surface from soft matter. Only by transmission electron microscopy (TEM) it was possible to image their metallic cores. This was done by a Tecnai F20 TEM from *FEI* (Eindhoven, Netherlands), shown in Figure 4.9. In the TEM image the metallic iron core is visible, and could be measured to approximately 7 nm. The amorphous myristic acid coating is merged with the also amorphous background of the applied TEM sample holder grit.

As shown in Figure 4.10, EDX mapping detected the co-localisation of the *Fe*-based nanoparticles and the cell colonies. However, this could still also indicate an agglomeration of the nanoparticles on the cell's outer membrane. It is so far not certain that they are really incorporated.

The presence of the nanoparticles inside the cells was proven by combined FIB and SEM techniques, as likewise done by Garcia *et al.* [106] regarding the cell uptake of *Ag* nanoparticles. Therefore, two single cells were chosen to be cut by

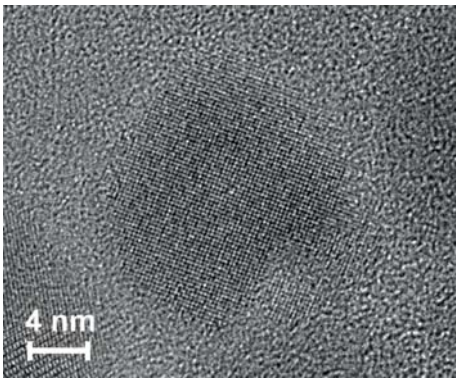


**Figure 4.9:** TEM image of a *Fe*-based nanoparticle, with a *Fe* core of about 7 nm in diameter. The point-lines are projected atom layers of iron crystal structure.

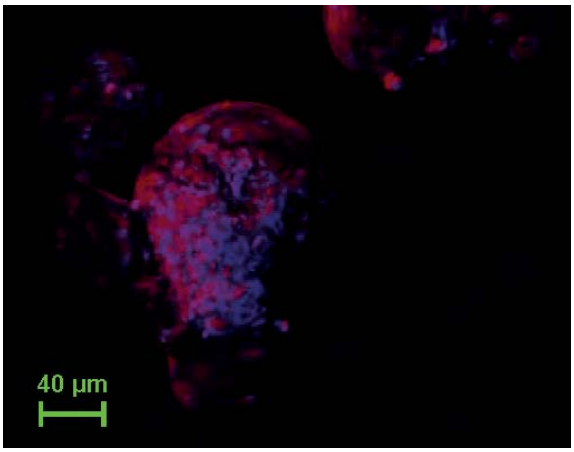


**Figure 4.10:** EDX mapping overlay composed of the *C* signal in red, and the *Fe* signal (K-shell) in blue. This is indicating a perfect co-localisation of the *Fe* nanoparticles and cells, performed at 20 kV $U_{EHT}$ on sample disc #23.

FIB to perform EDX-mapping on the cross section, and thus on the inner parts of the cells. To avoid curtaining a *Pt* layer was deposited at the dedicated cutting area on the top[7] of the cell by using the GIS. The FIB cut was performed by a 2 nA FIB current, resulting already in a very smooth cross section surface (Figure 4.11 parts (a), (b) & (c)). A subsequent fine cut with a lower FIB current of 200 pA showed no improvement of the cross section.
The EDX mapping on the cross sections proved in both cases that the *Fe*-based nanoparticles are inside the cell. In Figure 4.11 parts (a) & (c) an overlay composed of the cell's cross section with the mapping of the K-shell signal of *Fe* is shown.
Regarding figure part (a), the iron content below the *Pt* deposition is definitely in the cell. Also by considering a possible deeper positioned origin of these mainly two *Fe* agglomeration-spots, - besides the cell matter - only *Ti*-6*Al*-4*V* substrate material which contains no iron is present in the deeper regions below the detection area. Those *Fe* signals behind the *Pt* deposition are probably shining through the outer cell membrane, since EDX is also sensitive to the subsurface.
The EDX mapping on the cell which is cross sectioned parallel to the FIB, in Figure 4.11 part (c), made it very clear that the *Fe* is laterally distributed inside the cell.
In both mappings the nanoparticles appear to be located outside but close to the nucleus, and may aggregate in cytoplasmic structures. The *Fe*-based nanoparticles are therefore really incorporated by the cell and don't just adhere on their surface. But regarding the incomplete enclosure of *Fe* in the cell as a whole, it can be concluded that the iron alone will probably not achieve the necessary attenuation increase of the whole cell for tomography.

[7] the top is always defined in direction to the FIB column

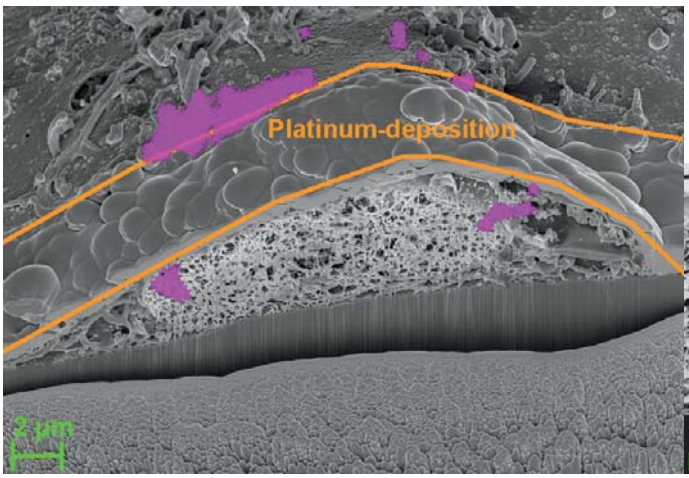


**(a)** FIB processed cross section on cell perpendicular to FIB, with purple *Fe* overlay

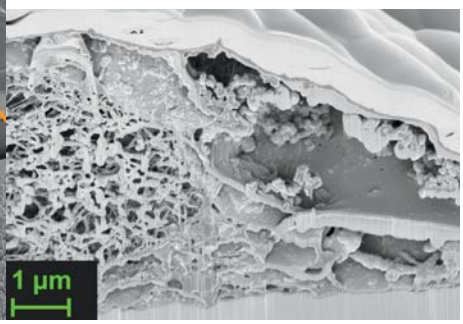


**(b)** Partial cross section of (a) in detail

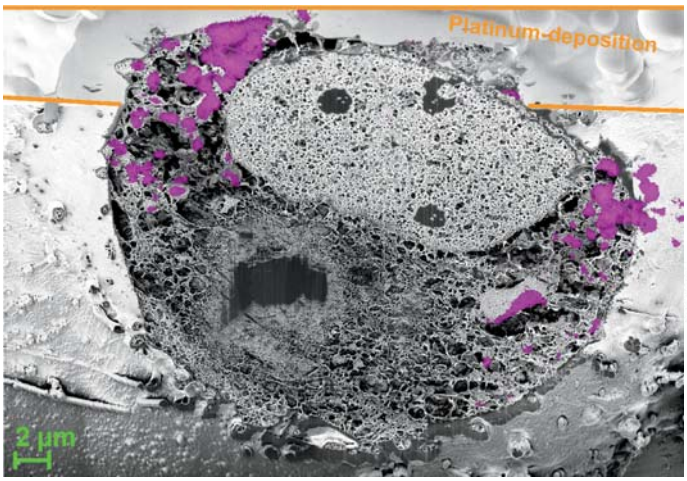


**(c)** FIB processed cross section on cell parallel to FIB, again with purple *Fe* overlay

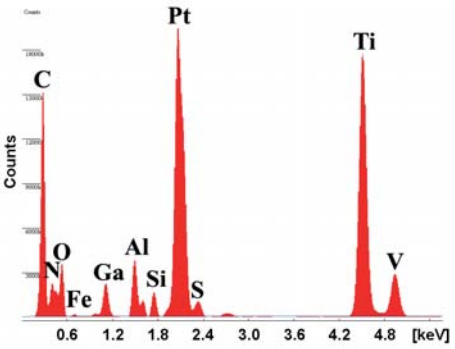


**(d)** Corresponding EDX spectrum to (a)

**Figure 4.11:** (a) & (c) SEM Image of FIB cross section on cells (sample disc #23) at 3 kV $U_{EHT}$, 5 mm WD, InLens-detector, with *Fe* K-shell mapping overlay (purple) (EDX performed at 15 kV $U_{EHT}$). (c) cell cross section in detail, at 1 kV $U_{EHT}$. The cell nucleus is the inner, strongly networked area, while the plane shaped structure to the right (figure part (c)) is supposed to be endoplasmatic reticulum.

## 4.5 SR$\mu$CT on porous implant material with cells

To characterise single cells inside the porous matrix material SRnCT should be performed, providing the necessary high resolution. For a first step the visibility of the described cell attenuation enhancing staining was to be proven in a tomography experiment by SR$\mu$CT at beamline BW2 (DORIS III, DESY).
Therefore the mentioned smaller cylindrical samples of about 3 mm in diameter and 2 mm in height were prepared in analogy to the already SEM-investigated 10 mm diameter samples. Except for one additional advancement: Now the osteoblast-like cells were also cultivated for three different times in order to see proceeding colonisation steps of the cells into the porous materials. These samples were again pre-characterised by SEM, revealing a proper cell enclosure on the surfaces.

During the tomographic experiment it was found that a X-ray energy of 50 keV is needed to penetrate the *Ti*-6*Al*-4*V* substrate material. This was more than expected for these purposely small shaped and even porous samples. The following data evaluation by using again the myVGL software did not confirm the pre-characterisation by SEM: no significant attenuation peak could be found in the grey value histogram of any tomography image of the samples which would image something in between the obtained attenuation peaks of air and of the substrate material.
To make it certain, the voxels on the surface were selected by separating an intermediate attenuation value to air and *Ti*-6*Al*-4*V* in the grey value histogram. These voxels were then coloured in a transparent red (Figure 4.12). By this explicitly every additional material that is situated on the surface of the substrate would be highlighted. Unfortunately nothing was found.
None of the cells were visible by SR$\mu$CT, thus all applied staining methods were insufficient for this purpose.

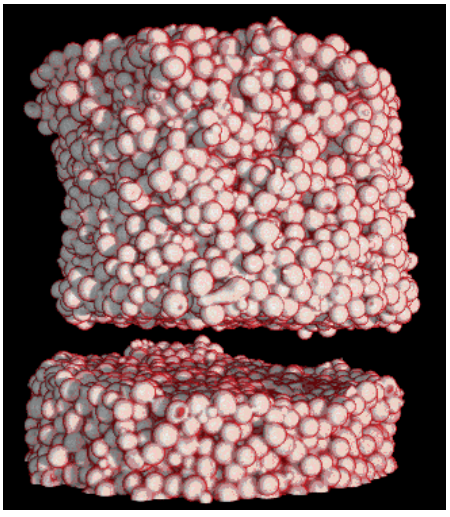

**Figure 4.12:** SR$\mu$CT by BW2 at HASYLAB (DESY) on a Mix-material substrate with adherent Saos-2 cells subsequent to metal incorporation. The image shows a 3D reconstruction of one and a half samples, each 3 mm in diameter, the lower supposed to be with cells, and the upper as control without.

## 4.6 Summary

The characterisation of the material substrate by tomography provided detailed knowledge on the porous network structure inside, and the pore size distribution by the granulometry calculation.
External *in vivo* studies revealed a crucial role on material porosity for tissue ingrowth, highlighting a 30% porosity provides an excellent tissue ingrowth [4]. It could be shown by the tomographic characterisation that this precondition is totally fulfilled by the two porosities Large and Mix.
Evaluating the granulometry data, both sample types Large and Mix exhibit a similar and high pore size variability of up to basically 200 $\mu$m pores in diameter, proposing to be well suitable for cell ingrowth [17; 68].
The SEM imaging of the cell colonisation could successfully clarify the ingrowth of cells into the porous network. Independent of the porosity types Large and Mix the viability for cells through the entire sample was proven, which was cooperatively published by Deing *et al.* [25].
The presence of the phospholipid coating is indicated by *Au*-labelled phospholipids on polished surfaces as well as by SEM imaging and EDX on the internal surface of the respective broken samples.
The incorporation of iron nanoparticles was verified by EDX inside of two single Saos-2 cells, enabled by a FIB cross section.

None of the cells was visible by SR$\mu$CT, therefore the staining can be expected to be insufficient for SRnCT too.
Therefore, in the next step the tomographic phase contrast[8] method should be applied in the scope of SRnCT future experiments on such samples as soon as this method is available at IBL.

[8]For background information on phase contrast please refer to Appendix A.

# Chapter 5

# Applications: Degradable magnesium based implants

## 5.1 Corrosion of different Mg alloys in physiological solutions

In a proof of concept study *Mg* already showed favourable properties for medical applications [142]. But besides of stent applications there is so far no other clinical usage. Although orthopaedic and paediatric applications are of high interest, the necessary approaches are hindered by the deficit of proper and predictive in vitro systems. A first step was done by recent studies regarding *Mg* degradation under cell culture conditions, which revealed a change in the formed corrosion products compared to technical setups [138; 132].

To explore further aspects of the corrosion environment the availability of oxygen and proteins was studied within this work, jointly published by F. Feyerabend *et al.* [34]. Since it is known that the type of alloy and the preparation of the samples have an influence on the corrosion properties of the material, three different alloys (pure *Mg*, WE43 ($Mg4Y0.5Gd2Nd0.5Dy$) and E11 ($Mg10Gd1Nd$)) under four surface conditions were analysed.
The relevant parts of the sample preparation, which was done by Feyerabend [34], are shortly outlined in the following.

### 5.1.1 Sample preparation and corrosion environment

The Magnesium casting was prepared by pure *Mg* (99.95 wt.%) and pure alloying elements in a mild steel crucible under a cover gas mixture of $Ar_2$ and 0.3% $SF6$. After mixing at 730°C for 1.5 h, the alloy was cast to the preheated mould at 500°C. The filled mould was held at 670°C for 1 h under protective gas ($Ar$ + 0.3% $SF6$). Afterwards, the steel crucible with the melt was immersed continuously into the cooling water with a speed of 10 mm/s. When the bottom of the steel crucible

touched the water it was stopped for 1 s. As soon as the liquid level of the melt at the inside was in alignment with the height of the water outside, the solidification process was finished.
The ingots were cut by electrical discharge machining into plates (20 cm × 12 cm × 2 cm). Cylindrical samples (5 mm diameter) were prepared by laser cutting. The sample surfaces were treated by three different methods: (1) as cut; (2) electro polished, and (3) etched. The samples were cleaned in ethanol after every process step.
Sonificated was done with the samples for 20 min in dry isopropanol, dried and gamma-sterilized at the In core irradiation (ICI) facility of the Geesthacht neutron facility with a total dosage of 29 kGy.
The corrosion tests were performed by using two different solutions: I. Hanks balanced salt solution without calcium and magnesium (HBSS, *Invitrogen Corporation*, Karlsruhe, Germany) and II. Dulbecco's modified eagle medium Glutamax-I (DMEM, *Invitrogen Corporation*, Karlsruhe, Germany). An additional experiment was performed by supplementing all solutions with standardized 10% fetal bovine serum (FBS, *PAA Laboratories*, Linz, Austria), to determine the influence of proteins.
Corrosion experiments were done at 37°C, 5% $CO_2$, and 95% humidity in an incubator (Heraeus BBD 6620, *Thermo Fisher Scientific*, Schwerte, Germany). The oxygen content was either set to 20 or 5%, while the exposition time of the samples was at maximum 72 h. Subsequently the samples were rinsed for 1 min in distilled water, followed by drying in a vacuum oven for 24 h.
The specimens were cross sectioned by a diamond wire, embedded in a resin and polished in two steps: with alumina and finally with a 0.1 $\mu$m colloidal silica suspension.

### 5.1.2 Scanning electron microscopy

The surface imaging of the corroded samples was performed at 5 kV $U_{EHT}$ accelerating voltage using the secondary electron detector (SE2-detector). The voltage was chosen comparably low to avoid charging effects by the less conductive corrosion layer.
Due to the epoxide resin the cross sectioned samples had to be coated with a gold-palladium alloy, by the sputter device introduced in subsection 3.1.2, to allow SEM investigations. These embedded and coated samples could be imaged at 20 kV $U_{EHT}$ using the back scattered electrons detector (BSE-detector) in order to gain material contrast along the cross section. The influence of the thin gold-palladium coating did not seriously bother the BSE imaging.
EDX-mappings were performed at again 20 kV $U_{EHT}$ on every sample for the respective regions of *Mg*, *N*, *Na*, *C*, *Ca*, *Cl*, *K*, *O*, and *P* in the EDX spectrum to identify qualitatively[1] the lateral element distribution of the corrosion layer.

[1] without calibration standard sample

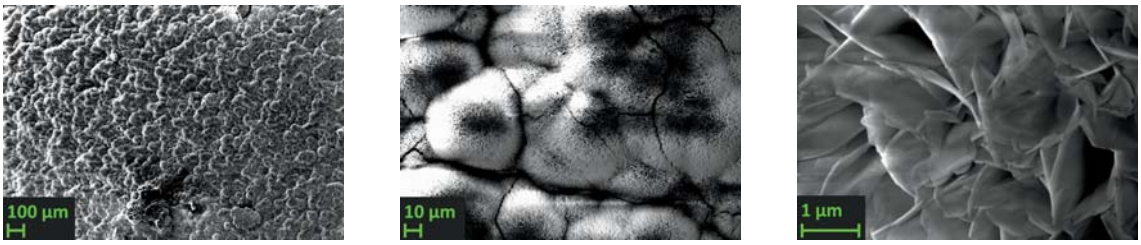


(a) (b) (c)

**Figure 5.1:** SE2 images of HBSS immersed sample at 5kV $U_{EHT}$. Figure part (c) reveals a corrosion structure made by very thin plates.

Every image consists of at least 32 summed mapping frames, at a minimum resolution of 512 × 400 points with a dwell time of 500 $\mu$s per point, on a sample area of approximately 130 $\mu$m × 100 $\mu$m respectively. To obtain a high counting rate by EDX the SEM high current mode in combination with the 120 $\mu$m diameter aperture was used. Automatic drift correction by the smart SEM software was applied during mappings to improve image quality. Altogether 27 different EDX-mappings were performed on interesting areas on the samples.

### 5.1.3 Results by SEM

The surface visualisation by SEM depicted a characteristic corrosion behaviour by the different immersion media, though the different alloys appeared similar. In general a formation of crystalline precipitates in different shapes was found.

The visualisation of samples immersed in HBSS under cell culture conditions (Figure 5.1) revealed an irregular *Mg* corrosion surface, built by a dense formation of very thin plates. EDX analysis detected only *Mg*, *C*, and *O* as basic elements. The atomic percentages were *C*: 3.24 At%, *O*: 90.91 At%, and *Mg*: 5.85 At%.

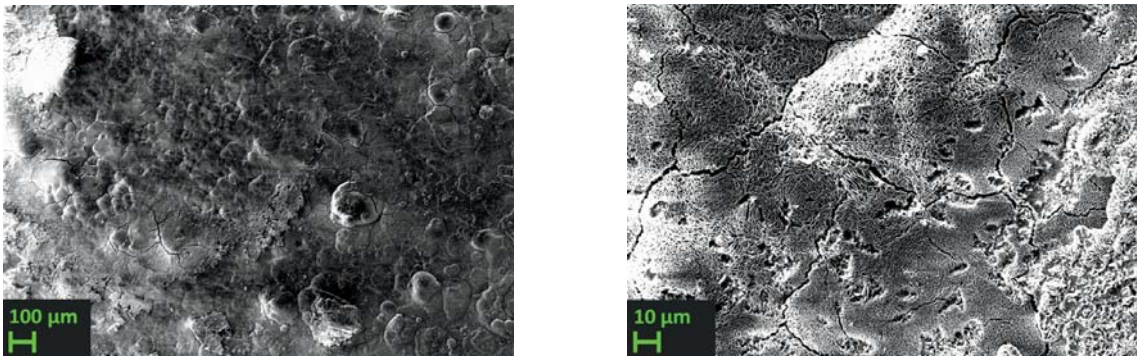


(a) (b)

**Figure 5.2:** SE2 images of HBSS + 10% FBS immersed sample at 5kV $U_{EHT}$.

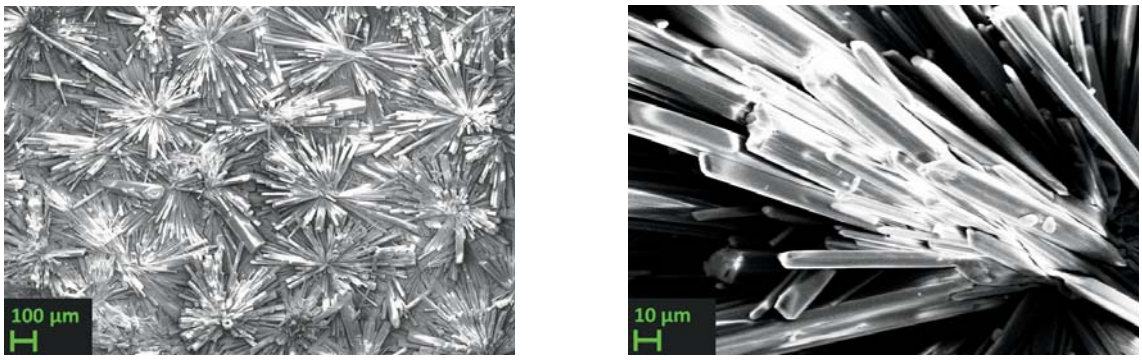


**(a)** **(b)**

**Figure 5.3:** SE2 images of DMEM immersed sample at 5kV $U_{EHT}$.

The addition of proteins to the immersion media by adding 10% FBS caused many additional holes on the corrosion surface and made it even more irregular (Figure 5.2). Now also *N* and *Na* could be detected by EDX, which could indicate some protein residuals incorporated by the corrosion layer. The entire element ratio is depicted as *C*: 4.54 At%, *N*: 0.47 At%, *O*: 90.24 At%, *Na*: 0.09 At% and *Mg*: 4.66 At%.

For the samples immersed in DMEM, a mainly homogeneous structure of crystalline formations became visible by SEM (Figure 5.3). These structures were already discernable by eye as white matter on the surface. Therefore they appear comparably big by the magnified look by SEM, which revealed no substructure of the crystals. The EDX analysis depicted the element composition to *C*: 2.94 At%, *O*: 94.74 At%, *Ca*: 0.02 At% and *Mg*: 2.3 At%.

Adding 10% FBS to DMEM is the most similar physiological corrosion media. Compared to the pure DMEM immersion, the crystal formation was now reduced (Figure 5.4). Besides the crystalline formations which are already known from the pure DMEM immersion samples, two additional and smaller kinds of crystalline corrosion shapes could be observed on the surface (Figure 5.4 part (c) and (d)). The EDX analysis on this sample showed the elemental composition *C*: 5.34 At%, *N*: 0.58 At%, *O*: 90.06 At%, *Na*: 0.07 At%, *Mg*: 3.9 At%, *P*: 0.03 At%, *S*: 0.01 At% and *Ca*: 0.01 At%.

The EDX-mapping on the corrosion cross section of this sample (Figure 5.5) revealed a co-localisation of calcium (*Ca*) and phosphorous (*P*). This visualised the formation of calcium phosphates ($Ca_x(PO_4)_x$) in calcium containing medium (DMEM). The distribution of these elements is inhomogenous throughout the corrosion layer, manly located at the interface of bulk material and corrosion layer. This was observed for in vivo stent applications too, where calcification during degradation was found [55; 29]. Though for stent applications calcification is undesired this could be highly favourable for orthopaedic ones [34].
Furthermore, the carbon (*C*) distribution was associated in many regions with oxygen (*O*).

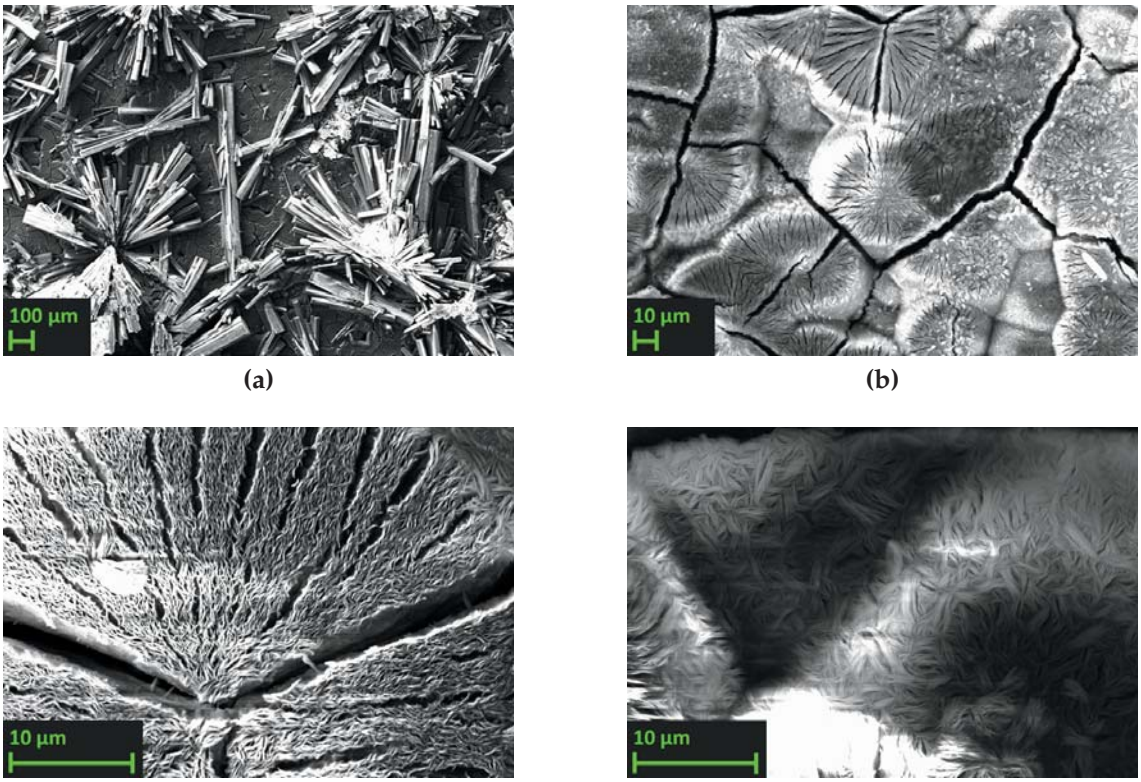


**Figure 5.4:** SE2 images of DMEM + 10% FBS immersed sample at 5kV $U_{EHT}$.

### 5.1.4 Summary

The SEM visualisation and EDX analysis provided a complementary and more detailed insight of the corrosion process. Among others, the different buffering capacity of the four immersion solutions as well as the varied presence of proteins led to a unique crystalline growth on each sample. The EDX-mapping revealed the co-localisation of elements. This knowledge could not be achieved by the statistical analysis alone.
Evaluating the experimental results together with the existent literature data leads to the assumption that the application of cell culture conditions in combination with an appropriately buffered solution including proteins should be a standard

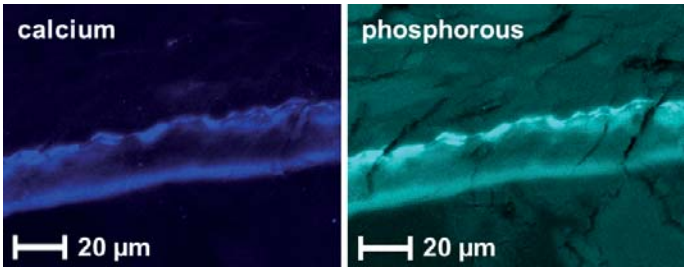


**Figure 5.5:** EDX mapping for *Ca* and *P* on the corrosion cross section of a *Mg* sample immersed in DMEM + 10% FBS. The co-localisation of both elements is nicely visible.

for the in vitro analysis of magnesium and its alloys [34]. The comprehension of underlying corrosion mechanisms as well as of relevant influencing factors will provide the knowledge to improve an in vitro magnesium degradation test setup. Finally the comparison of experimental data from in vitro experiments with this setup to data obtained from in vivo experiments will be of major importance [34]. For this it will be a great benefit to perform SRnCT experiments using phase contrast to reveal the in vivo *Mg* degradation and parallel bone formation in different states.

## 5.2 Element distribution in the corrosion layer of Mg-10Dy

The FIB enables additional subsurface investigations to the surface limited SEM techniques. By combination of both techniques the structure of fine polished FIB prepared cross sections, up to a depth of several 10 $\mu$m, can be analysed by the SEM. In the present work this method was used for a study on the corrosion behaviour of a bio degradable $Mg - 10Dy$ alloy, as published cooperatively by L. Yang *et al.* [144].
Since *Dy* is one of the best tolerated rare earth elements regarding cytocompatibility, and offers a good combination of mechanical and corrosion properties, it is considered for a biodegradable *Mg* alloy for medical implants. Provided by the high solubility of *Dy* in *Mg* the ratio of *Dy* should enhance tunable degradation characteristics to the *Mg* alloy.
A good combination of mechanical and corrosion properties was found by a previous study on solution heat treated *Mg-Dy* alloys [145].

In the scope of the present work solution heat treated $Mg - 10Dy$ was investigated regarding composition and element distribution on the surface as by cross-sectioning of the corrosion layer. Furthermore, the cytocompatibility of extracts and the corrosion layer was evaluated by L. Yang. It follows again a short outline of the sample preparation and corrosion testing as well as of the culturing and the cytocompatibility testing which was done by L. Yang [144] to elucidate the context of the FIB/SEM investigations.

### 5.2.1 Sample preparation

**Materials preparation** Pure Mg (99.94%) (MEL, UK) melted in a mild steel crucible was alloyed by 10 Wt% (1.6 At%) of pure Dy (99.5%) (Grirem, Beijing, China) at a melt temperature of 720 °C under a protective gas atmosphere (Ar + 2% SF6). The melt was then stirred mechanically for 30 min with rotational speed of 200 rpm. The permanent mould direct chill casting technique was used to prepare ingots (20 × 12 × 6 cm). Also Pure Mg was prepared as a reference material

for corrosion rate and cytocompatibility tests, using the same melting process. Solution treatment was performed on the $Mg-10Dy$ alloy at 520 °C for 24 h.

**Corrosion tests** The specimens for the corrosion tests were prepared by grinding each side of the sample with 2400 grit emery paper, followed by degreasing with ethanol and drying in room air. Three samples were used for each sterile corrosion condition. The samples were sterilised in a solution of 70% ethanol for 15 min. After drying each sample was immersed in a cell culture medium (CCM) consisting of Dulbecco's modified Eagle's medium (DMEM) Glutamax-I (*Life Technologies*, Darmstadt, Germany) and 10% fetal bovine serum (FBS) (PAA Laboratories, Linz, Austria). The samples were then incubated in an incubator (Heraeus BBD 6620, *Thermo Fisher Scientific*, Schwerte, Germany) under cell culture conditions (37 °C, 21% $O_2$, 5% $CO_2$, 95% relative humidity). The ratio of corrosion medium to surface area of sample was 1.5 ml/cm$^2$. After immersion for up to 28 days without changing the medium the samples were rinsed in distilled water, dried and kept in a vacuum drying chamber.

**Cell isolation and culturing** Osteoblasts were taken from bone chips donated by a patient of total hip arthroplasty following the protocol of Gallagher [36]. Briefly, cancellous bone was removed from the femoralhead with bone rongeurs as pieces of about 5 mm diameter. Bone marrow and non-bone components were removed by thorough vortexing in phosphate-buffered saline (PBS) repeatedly for 30 s, while exchanging continuously the PBS. As bone fragments became white and ivory-like they were cultured in DMEM Glutamax-I with 10% FBS, 1% penicillin, and 100 mg l$^{-1}$ streptomycin (*Life Technologies*, Darmstadt, Germany) for 10 days without changing the medium. Thereafter the medium was changed every 2-3 days. Passage was at 70-80% confluence, and for the experiments cells in passage 2 were used.

**Cytocompatibility of the corrosion layer** Cylindrical specimens with a diameter of 10 mm and a height of 1.5 mm were cut by electrical discharge machining. These specimens were ground all around with 2400 grit emery paper, followed by ultrasonic cleaning in 100% ethanol and drying in room air. Before experiments the specimens were sterilized by immersion in 70% ethanol for 15 min.
The evaluation of the cytocompatibility of the $Mg-10Dy$ alloy's corrosion layer was done by cell adhesion and Live/Dead staining tests, while Pure $Mg$ specimens served as reference samples. Prior to cell seeding the specimens were preincubated for 2 h (cell adhesion test) or 3 days (Live/Dead staining) in CCM under cell culture conditions. To avoid growth of cells on the 12-well plates agarose coatings were used (Nunc, Wiesbaden, Germany). The Osteoblasts were seeded with a density of 100,000 cells per specimen on the top of them, lying in the 12-well plates immersed in 50 $\mu$l of solution. Subsequently this was incubated for 40 min to allow the cells to settle down, followed by 3 ml of CCM which was added to each well and was then refreshed every 3 days.
After incubation of 3 and 7 days the specimens were rinsed with PBS and then immersed overnight in 2.5% glutaraldehyde solution achieving cell fixation. Af-

terwards the specimens were stained by immersion in 1% osmium tetroxide for 30 min. Gradual dehydration was carried out by an alcoholic row from 20 to 100 vol.% isopropanol (section B.1). The specimens became supercritical dried with $CO_2$ by using a Leica EM CPD030 from *Leica Mikrosysteme* (Wetzlar, Germany)[2]. Cell morphology was investigated by SEM using 1 keV $U_{EHT}$ with two replicates for each condition.

### 5.2.2 Results by SEM

#### Corrosion behaviour and element distribution in the corrosion layer

By FIB cross sectioning of $Mg - 10Dy$ after 3 days immersion in CCM (Figure 5.6) some cavities were detected at the interface between the corrosion layer and the substrate (Figure part (b) and (c)).

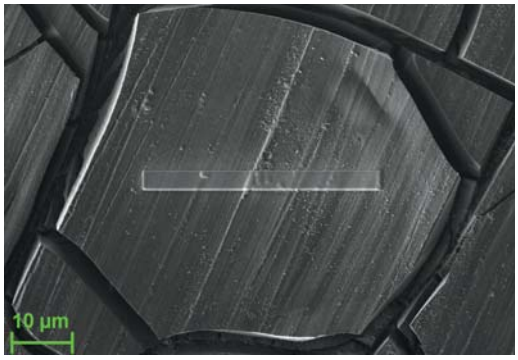


**(a)** FIB image (30 kV, 50 pA) with protective *Pt* deposition at the cut area (5 mm WD, SE2-detector)

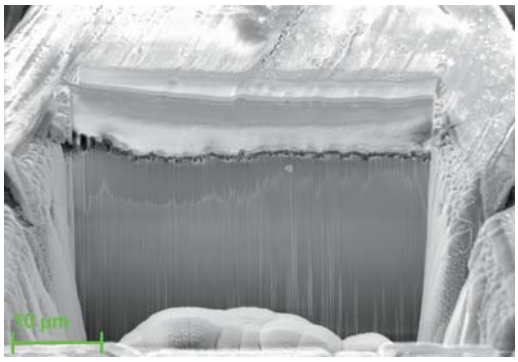


**(b)** SEM image (5 kV $U_{EHT}$, 5 mm WD, InLens-detector) of the cross section

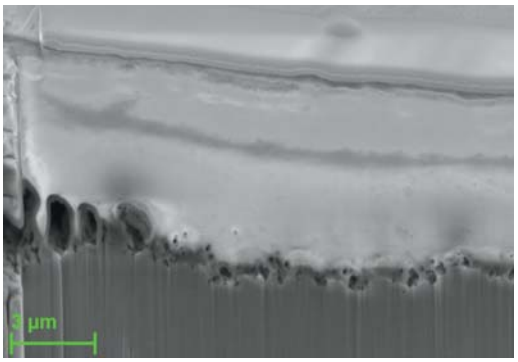


**(c)** cross section in detail

**Figure 5.6:** FIB processed cross section in the corrosion layer of the $Mg - 10Dy$ alloy after 3 days immersion. In Figure part (b) & (c) cavities and drains along the interface are visible.

[2]The critical point drying procedure can be reviewed in section B.1

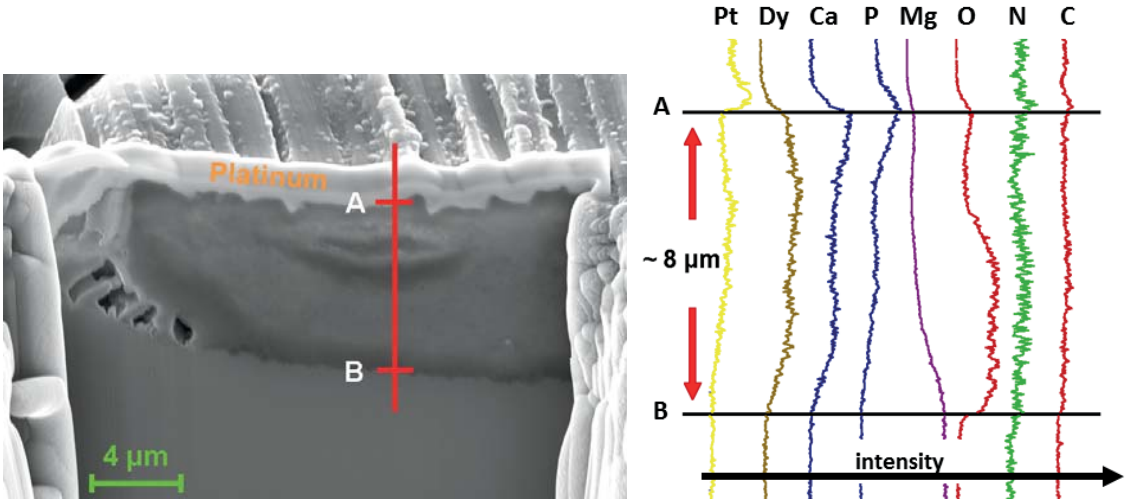


**(a)** FIB milled cross section in the corrosion layer of a $Mg-10Dy$ alloy (20 kV $U_{EHT}$, 4.9 mm WD, InLens-detector)

**(b)** vertical EDX scan along the red line on selected element shell signals

**Figure 5.7:** EDX line scan on FIB processed cross section featuring qualitative distributions of the recorded elements. The sample was immersed for 3 days in cell culture medium. A FIB/GIS processed platinum deposition was applied to smooth the surface in order to avoid curtaining and to protect the upper part of the corrosion layer against FIB damage.

The thickness of the corrosion layer is about 7.5 $\mu$m, in consistence with the other results of this study. The cavities were formed most likely during dehydration, since the corrosion layer volume decreased by drying while the substrate remained unchanged. This mismatch and the oxidation stresses at the interface are certainly the cause for the cavities. [144].
By additional EDX-mapping the elemental distribution in the corrosion layer of this cross section was visualised. $N$ and $C$ are mainly distributed on the surface of the corrosion layer, while the $P$ and $Ca$ content decreases from the top to the bottom of the corrosion layer. $Mg$ and $Dy$ are homogeneously distributed inside the layer. The amount of $Dy$ in the corrosion layer is significantly higher than that in the $Mg-10Dy$ substrate and it seems to accumulate here during the corrosion process [144].

To confirm the results a further corrosion layer cross section was prepared by FIB on another sample which was equally prepared (Figure 5.7). Again cavities are observed on the left side of this cross section. The corresponding semiquantitative EDX line scan along a vertical line from point A to B on the corrosion cross section provided a more detailed understanding of the elemental trend.
The increased amount of $Dy$ in the corrosion layer compared to the substrate is even more clearly observed, indicating a lower solubility for $Dy$ corrosion products in the immersion media than for those of $Mg$. The $P$ and $Ca$ content is gradually decreasing from the surface to the bottom of the corrosion layer. The $O$

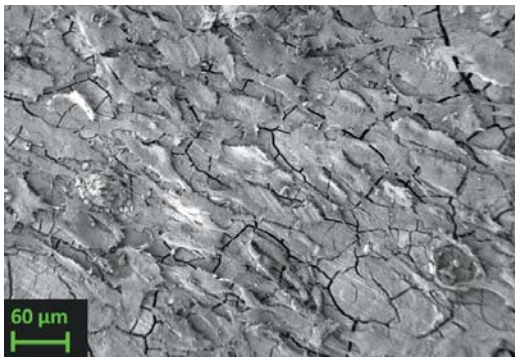


**(a)** *Mg* after 3 days cell culture


**(b)** *Mg* after 7 days cell culture

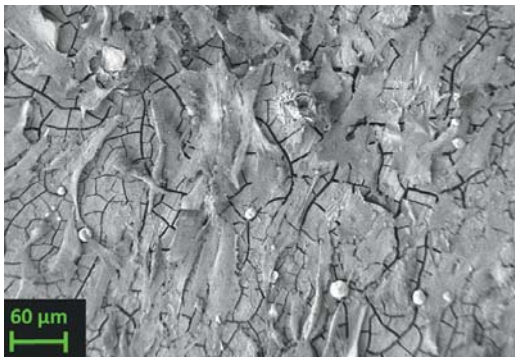


**(c)** *Mg*-10*Dy* after 3 days cell culture

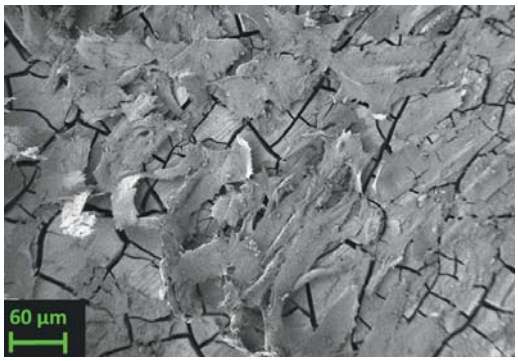


**(d)** *Mg*-10*Dy* after 7 days cell culture

**Figure 5.8:** Population of human osteoblasts on pure *Mg* and *Mg*-10*Dy* after 3 and 7 days culture (1 kV $U_{EHT}$, 4.8 mm WD, SE2 detector).

fraction is increased towards the bottom of the corrosion layer, which indicates a possible oxygen-driven corrosion process.

### Cell morphology

The cell populations on the surface of the samples after culture for 3 and 7 days are shown in Figure 5.8. After culturing for 3 days or more, large numbers of cells were observed on the surfaces. The cells were well spread over the surface of both, pure *Mg* and $Mg - 10Dy$. However, presumably due to the drying of the samples, a gap between cells and corrosion surface is observed in most cases. However, the cells are well connected to the surface, at least by their outspread contact points.
Also after 7 days no negative effect to the cells by the *Dy* enrichment could be observed.

### 5.2.3 Summary

The primary human osteoblast morphology could be observed by SEM on all cultured samples.
The FIB cross sectioning provided the characterisation of the corrosion layer with EDX in order to obtain information about the element distribution. The element distribution is inhomogeneous from the surface to the bottom of the corrosion layer. $Dy$ is enriched in the corrosion layer, and is supposed to exist as a mixture of $Dy_2O_3$ and $Dy(OH)_3$. The content of $Ca$ and $P$ decreases gradually from the surface to the bottom. Due to the buffering effect of $CO_2$, $MgCO_3 \cdot 3H_2O$ forms during corrosion and accumulates in the corrosion layer after the corrosion solution becomes saturated. Both extracts, as well as the $Dy$-enriched corrosion layer of alloy $Mg - 10Dy$, are not resulting in cytotoxicity to human osteoblasts [144].
By SRnCT, again in combination with the phase contrast method, it will be possible in the future to achieve the 3D imaging of a much bigger corrosion layer region. Especially the statistical data evaluation regarding the corrosion determination would be provided by this.

# Chapter 6

# Applications: Nanoconfined materials for reversible hydrogen storage

Hydrogen is considered as one of the most suitable energy carriers for sustainable energies in the future. A crucial issue for the use of hydrogen is to find a safe and high-density storage solution. Reversible storage by using metal hydrides is a promising approach [114].

## 6.1 Introduction

Particularly, lithium borohydride ($LiBH_4$) is interesting for providing the highest hydrogen storage capacity of 18.5 Wt% [16]. However, unfavorable kinetics and thermodynamics for dehydrogenation and rehydrogenation, as high desorption temperatures above 380 °C and slow rehydrogenation at 600 °C under 150 bar $H_2$, reduced its practical applications as a hydrogen storage medium. To improve this characteristics different approaches, as e.g. catalytic doping and Reactive Hydride Composites (RHCs) are explored. The $LiBH_4$-$MgH_2$ system showed a reduction in de-/rehydrogenation enthalpy (see Equation 7.1[1]) due to the formation of $MgB_2$ upon dehydrogenation [48].

$$2LiBH_{4(l)} + MgH_{2(s)} \longleftrightarrow 2LiH_{(s)} + MgB_{2(s)} + 4H_{2(g)} \tag{6.1}$$

Furthermore, the required temperature and pressure conditions are milder compared to pure $LiBH_4$. Since there are still obstacles for practical applications further improvements are needed. Therefore, nanoengineering by reducing the particle size of the metal hydrides is considered as an meaningful strategy to improve the hydrogen release and uptake kinetics.

[1] s: solid-; l: fluid-; g: gas- phase

The Auriga was used in the scope of the present thesis to prove the distribution of the respective elements of nanoconfined $2LiBH_4$-$MgH_2$ compounds on and inside a carbon aerogel scaffold by combined FIB/SEM techniques for several studies, jointly published by Gosalawit-Utke *et al.* [47; 48; 46; 44; 45].
The first study introduces an alternative approach for preparation of nanoconfined RCH by direct melt infiltration of bulk $2LiBH_4$-$MgH_2$ into an inert nanoporous aerogel scaffold [47].

This has been improved by the following study [48]. So far, the carbon aerogel of the resorcinol-formaldehyde (RF) precursor was prepared via several procedures, more than a week was required to accomplish a dried gel for carbonization. In this study a new material of resorcinol-furfural (RFF) aerogel was used complemented by a new technique of $CO_2$ supercritical drying for carbon aerogel preparation. By this drying technique the dried gel was achieved within 12 h instead of more than a week as before. Furthermore, the weight ratio of composite hydride ($2LiBH_4$-$MgH_2$) carbon aerogel increased from 1:2 to 1.5:2 which is enhancing hydrogen storage capacity of the system. Subsequently to carbonization the carbon aerogel scaffold obtained from RFF aerogel was nanoconfined with a bulk $2LiBH_4$-$MgH_2$ composite via direct melt infiltration [48].

In the third study [46] the nanoconfinement of $2LiBH_4$-$MgH_2$-$TiCl_3$ in resorcinole-formaldehyde carbon aerogel scaffold (RFeCAS) is proposed. RFeCAS is encapsulated with approximately 1.6 Wt% $TiCl_3$ by solution impregnation technique, and it is further nanoconfined with bulk $2LiBH_4$-$MgH_2$, again via melt infiltration. Faster dehydrogenation kinetics have been obtained after $TiCl_3$ impregnation.

The FIB/SEM techniques were used in a similar way for all studies to prove the enhanced sample preparation principle. To provide basic knowledge of the sample on the one hand but to stay by the scope of this thesis on the other hand, only the first study [47] is depicted in the following. The sample preparation was exclusively done by Gosalawit-Utke.

## 6.2 Sample preparation

The resorcinol-formaldehyde aerogels were prepared according to previously published procedures [81]. Synthesis of the aerogel was done by mixing 10.3513 g of resorcinol (99%, *Aldrich*), 14.20 ml of a 37 Wt% formaldehyde in water stabilized by methanol (*Merck*), 14.30 ml of deionized water, and 0.0397 g of $Na_2CO_3$ (99.999%, *Aldrich*) in a beaker while stirring continuously. Stirring was conducted until a homogeneous solution was obtained. Subsequently the solution was poured into two 50 ml polystylene bottles and was sealed. The mixtures were initially aged at room temperature (24 h), 50 °C (24 h), and 90 °C (72 h). Cooling down afterwards was done in room air. The blackish solid gel was recovered and infiltrated by an acetone bath, which was displaced twice within a period of 34 h. Finally the monolithic gels were left to dry in a fume hood for several days

and were then cut into smaller pieces (ca. 0.4 $cm^3$) and pyrolyzed in a tube oven under a nitrogen flow at 800 °C (heating rate 2.6 °C/min) and dwelling for 6 h at 800 °C. After switching off the furnace the samples were cooled down to room temperature naturally. The obtained gels were again dried at 500 °C for 16 h under vacuum, and are called RF now. The powders of $LiBH_4$ (>95.0%, *Sigma-Aldrich*) and $MgH_2$ (*Alfa Aesar GmbH & Co KG*) were milled under argon atmosphere for 5 h in the molar ratio of 2:1 respectively, using a Spex 8000 M Mixer Mill placed in a glovebox. The mixture of RF aerogel and bulk $2LiBH_4$-$MgH_2$ was ground at a weight ratio of 2:1 in a mortar, resulting in mortar-mixed RF-$2LiBH_4$-$MgH_2$ [47].

## 6.3 Combined FIB/SEM investigation

The nanoconfined $2LiBH_4$-$MgH_2$ was prepared for FIB/SEM experiments by melt infiltration in a Sievert-type apparatus at 310 °C and $p(H_2)$ = 60 bar. The powder sample was conductively fixed onto the sample holder by using silver glue (solvent: n-butylacetate). The sample was coated by gold-palladium sputtering, this time with a current of 30 mA for 30 s. Without conductive coating the specimen were unstable in the SEM image, even at low voltages the electron beam destroyed the surface structure.

The morphology of the material was investigated with SEM (Figure 6.1 part (a)), depicting the nanoporous structure of the RF aerogel. An internal view of the specimen (approximately 12 × 7 × 5 $\mu$m) was prepared by FIB (Figure 6.1 part (b)), to unravel the elemental composition inside this highly reactive material, because the surface was assumed to be oxidised by the necessary sample mounting for SEM.
In the area of the red frame EDX-mapping was performed for *Mg* and *B*. Both signals were combined in one image (Figure 6.1 part (d)) by photoshop from *Adobe systems* (San Jose, California, US).
The energy of the *B* signal is adjacent to that of *C*. Furthermore EDX is not really sensitive to lighter elements than *C*. Therefore, the *B* peak in Figure 6.1 part (c) is not significant. However, the infiltration of $LiBH_4$ was previously confirmed by SR-PXD[2] and DSC-TG-MS[3] results. The mapping showed homogeneous dispersion of *Mg* (from $MgH_2$) and *B* (from $LiBH_4$) atoms inside the carbon aerogel scaffold. This confirms that both, $LiBH_4$ and $MgH_2$, were successfully nanoconfined in the aerogel.

[2]In situ synchrotron radiation powder X-ray diffraction
[3]Differential scanning calorimetry-thermogravimetric analysis-mass spectrometry

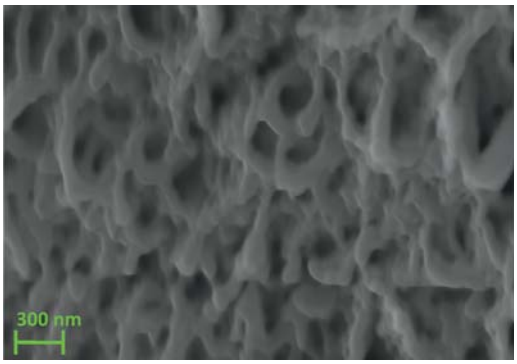


**(a)** surface morphology (15 kV $U_{EHT}$, 5.3 mm WD, SE2-detector)

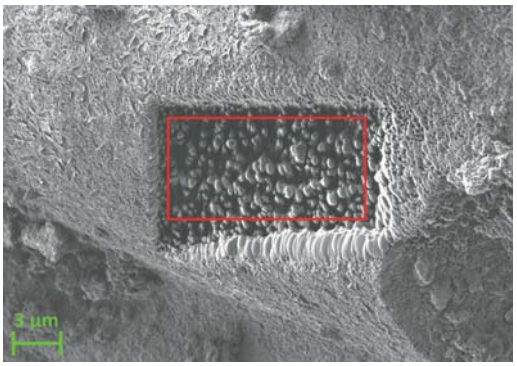


**(b)** FIB generated hole (FIB image (30 kV, 50 pA), 5 mm WD, SE2-detector)

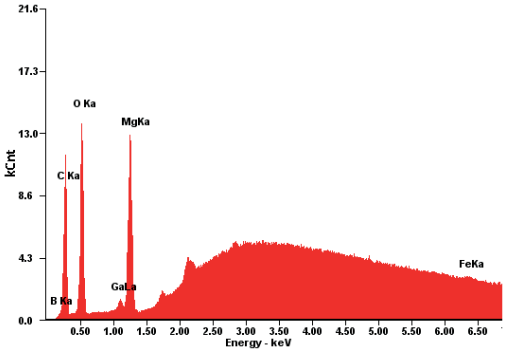


**(c)** spectrum of the corresponding EDX mapping

**(d)** EDX mapping overlay for *Mg* (yellow) and *B* (white dots)

**Figure 6.1:** Surface morphology of the nanoconfined $2LiBH_4 - MgH_2$ specimen (a); FIB generated hole in the specimen with EDX mapping frame (red) (b); EDX spectrum (c); EDX mapping (d).

## 6.4 Summary

SEM micrographs as well as EDX-mappings revealed a homogeneous dispersion of $MgH_2$ and $LiBH_4$ inside the carbon aerogel scaffold. The FIB method provided access to the not oxidised underground of this highly reactive material and hence results were not altered by oxidation or other environmental effects.
By this study it was furthermore proved that the simple preparation of nanoconfined $2LiBH_4 - MgH_2$ by direct melt infiltration of the bulk $2LiBH_4 - MgH_2$ into the carbon aerogel scaffold resulted in the generation of the nanoconfined material together with the improvement in hydrogen desorption kinetics. The hydrogen desorption kinetics of the nanoconfined $2LiBH_4 - MgH_2$ is significantly improved compared to bulk $2LiBH_4 - MgH_2$. To give an example, the nanoconfined $2LiBH_4 - MgH_2$ releases 90% of the total hydrogen storage capacity within 90 min, whereas the bulk material releases only 34% (at T = 425 °C and p($H_2$) = 3.4 bar). A reversible gravimetric hydrogen storage capacity of 10.8 WT% $H_2$, calculated

with respect to the metal hydride content, is preserved over four hydrogen release and uptake cycles [47].
The low density of the nanoconfined $2LiBH_4 - MgH_2$ material makes it again a perfect candidate for future phase contrast SRnCT at IBL as soon as this method is introduced.

# Chapter 7

# Applications: Ti-45Al-5Nb and 10Nb powder

## 7.1 Introduction

Gas-atomised spherical powders of *Ti*-45*Al*- 5*Nb* and 10*Nb*[1] alloys (from now on termed 5*Nb* and 10*Nb*) were produced in-house by HZG using the plasma melting induction guided gas atomisation (PIGA) technique.
In the scope of this thesis it was planned to image the distribution of the different phases in the powder particle interior by SRnCT, imaging the locally different attenuation originating from the local variations in chemical compositions. The 10*Nb* powder should show higher material attenuation for X-rays due to the higher *Nb* content, and therefore a possibly better contrast for SRnCT. Furthermore, the smaller powder particle fractions of up to 40 $\mu$m fulfil the size restrictions by the SRnCT experiment at IBL and allow the imaging of a complete particle.
Regarding the amount of *Al* in both alloys and the high cooling rates, it is expected that the phase composition will consist of hexagonal-close-packed $\alpha$- and body-centred-cubic $\beta$-phase [22].

### 7.1.1 Powder preparation

First a melt is generated by means of a *Ar*-operated plasma torch in a water cooled *Cu* crucible. Subsequently the melt is guided by a funnel to the center of a gas nozzle where it becomes atomised with *Ar* gas [40].
By this technique varying amounts of different sized particles are generated (shown in Table 7.1).

[1] composition in atom percent

| diameter [$\mu$m] | [%] |
|---|---|
| <20 | 4.40 |
| 20-32 | 6.39 |
| 32-45 | 8.43 |
| 45-63 | 11.94 |
| 63-90 | 15.71 |
| 90-125 | 19.71 |
| 125-180 | 18.21 |
| 180-250 | 10.65 |
| 250-355 | 4.57 |

**Table 7.1:** Mesh analysis in mass percent of 113.1 g *Ti*-45*Al*-5*Nb* powder produced by PIGA. The sieving time accounted 40 min.

### 7.1.2 Estimation of the critical growth rate for planar solidification

Schimansky *et al.* determined the cooling rate by *Ar* for a small particle with less than 20 $\mu$m diameter to roughly $10^6$ K/s [113]. This raises the question whether particles of the smallest particle fraction already solidified planar by the high cooling rate or not. The critical growth rate of a planar solid-liquid interface is given by [75]:

$$V_c > \frac{\Delta T_0^v D}{k_v \Gamma}. \tag{7.1}$$

In order to calculate $V_c$ for the $\alpha$- and $\beta$-phase, the solidification interval $\Delta T_0 = 50$ K was determined by the ternary phase diagram for $Ti - 8Nb - X\,AL$ from [143], while the diffusion coefficient at the melting point $D = 2.8 \cdot 10^{-9}$ m$^2$/s and the Gibbs-Thomson-coefficient $\Gamma = 1.5 \cdot 10^{-7}$ m·K are taken from [85].
The disequilibrium-distribution-coefficient is given by $k_v = \frac{k+\delta i V/Di}{1+\delta i V/Di}$ (after [75]). It is $k_v \approx k$ if $k = c_S/c_L \approx 1$, with $k$ the distribution-coefficient. The values for $k$ were again taken from the phase diagram by [143], with $k^\alpha = 0.94$ for the $\alpha$-phase and $k^\beta = 0.90$ for the $\beta$-phase. The critical growth rates finally result to

$$\begin{aligned} V_c^\alpha &> 0.993\ m/s \\ V_c^\beta &> 1.037\ m/s. \end{aligned} \tag{7.2}$$

## 7.2 Characterisation by SEM imaging techniques & EDX

To get a first impression if these particles would be proper samples for SRnCT, all fractions of the two powder alloys, *Ti*-45*Al*- 5*Nb* and 10*Nb*, were investigated by SEM imaging (Figure 7.1 part (a) & (b)). For this the powders were deposited on a sample holder and attached with silver glue. By SEM a cauliflower-like structure was detected on the surface of the particles, which is almost equally sized, independent of the particle diameter. By cross sectioning of embedded particles[2] and investigating using backscattered electron (BSE) contrast the continuation of this surface structures was detected as dendrites throughout the entire particles, shown for 10*Nb* in Figure 7.1 part (c) & (d). A FIB tomography by BSE contrast was not possible due to the shadowing of the ion beam by the lateral expansion of the BSE-detector.
The BSE contrast depicts the dentritic structure by its sensitivity to the atom number z, showing more signal for higher z-values. The structures in the powder particles show an unequal distribution of the alloy's elements and imply that no planar solidification occurred. Hence, even for a small particle with less than 20 $\mu$m diameter the cooling rate in *Ar* of roughly $10^6$ K/s by powder atomisation was still to low to reach the critical growth rate for absolute stability and thus obtaining a planar solidification.

To determine the internal elemental differences of the dendrite structures, EDX point measurements at 20 kV $U_{EHT}$ were performed of darker (interdendritic area) and brighter (dendrite core) regions of the BSE-images of the 10*Nb* alloy in Figure 7.1. The elemental composition in At% of a dark region of the 12 $\mu$m particle Figure 7.1 part (a) is *Ti*-46.02*Al*-8.70*Nb*, while a bright region was determined to be *Ti*-44.95*Al*-9.76*Nb*.
For a darker region of the 80 $\mu$m particle Figure 7.1 part (b), the elemental composition was determined to be *Ti*-48.73*Al*-6.66*Nb*, while a bright region showed a composition of *Ti*-44.46*Al*-10.42*Nb*.
As a result it is obvious that the bigger 80 $\mu$m particle features a higher difference in its elemental composition of the dendritic structures by the distribution of *Nb*. Furthermore, the average *Nb* content of the smaller 12 $\mu$m particle is explicitly less than given by the original composition of *Ti*-45*Al*-10*Nb*, while it is only slightly more for the bigger particle.
A complementarily EDX-mapping performed on the cross sections of these two particles is shown in Figure 7.1 part (f). The elemental contrast by *Nb* for the dendrites is hardly visible for the 12 $\mu$m particle, due to the comparable low resolution of EDX.
The dendritic structure of bigger particles of the *Ti*-45*Al*-10*Nb* alloy is more pronounced, while smaller particles seem to contain in average less *Nb*.

[2]The performed embedding is described in subsection 7.4.2.

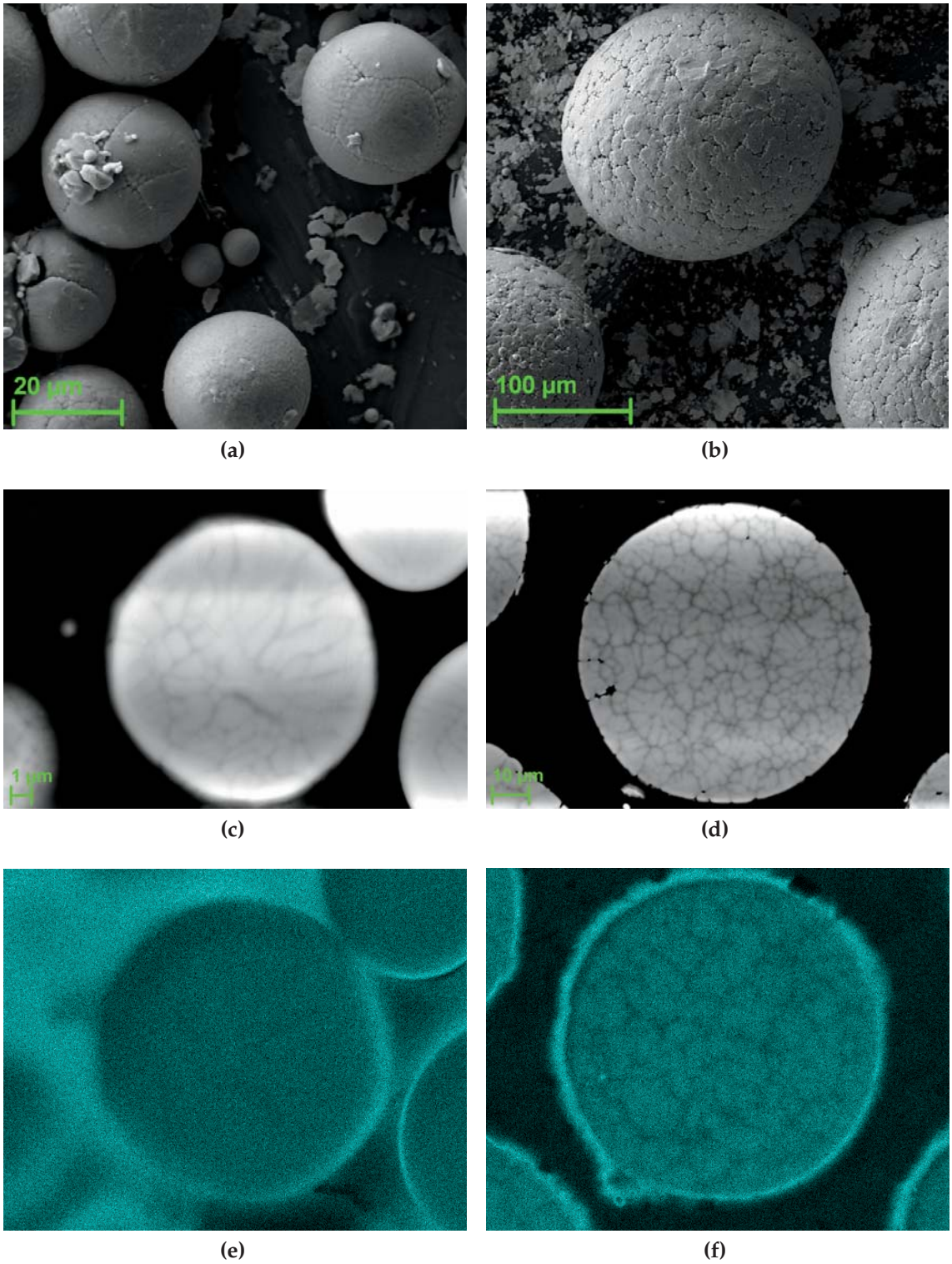


**(a)** **(b)**

**(c)** **(d)**

**(e)** **(f)**

**Figure 7.1:** SEM images of *Ti*-45*Al*-10*Nb* powder on the fractions 20-32 $\mu$m (a) and 180-250 $\mu$m (b); 15 kV $U_{EHT}$, 5 mm WD, SE2-detector. Cross sections with dendrites structures of (c) 12 $\mu$m and (d) 80 $\mu$m particles in diameter, with corresponding EDX-mappings (e) & (f) respectively; 20 kV $U_{EHT}$, 8.5 mm WD, BSE-detector, EDX was performed at 20 kV $U_{EHT}$.

## 7.3 Phase composition by Powder diffraction

Powder diffraction was performed for the *Ti*-45*Al*- 5*Nb* and 10*Nb* powders at the HEMS[3]-sidestation (beamline P07b) at PETRA III (DESY). The powders were filled in glass tubes with an inner diameter of 4 mm. The energy of 87 keV was used to record the diffraction patterns, also called "Debye-Scherrer-Rings", by the "Mar345" detector. Subsequent to a static measurement, each tube was additionally half rotated (i.e. 180°) in the 0,5 × 0,5 mm sized beam during the exposure time of this second measurement. The rotation was applied to obtain totally symmetric diffraction rings on the detector plane for bigger particles too. Due to their size and thus bigger interstices between the particles they are providing less grains per volume to be hit by the beam. Hence not all possible grain orientations are present without rotating, resulting in closed Debye-Scherrer-Rings.

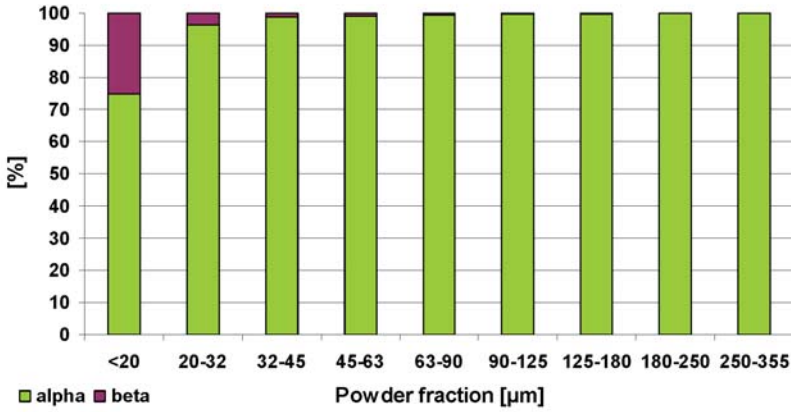


**(a)** Phase distribution of 5*Nb* powder

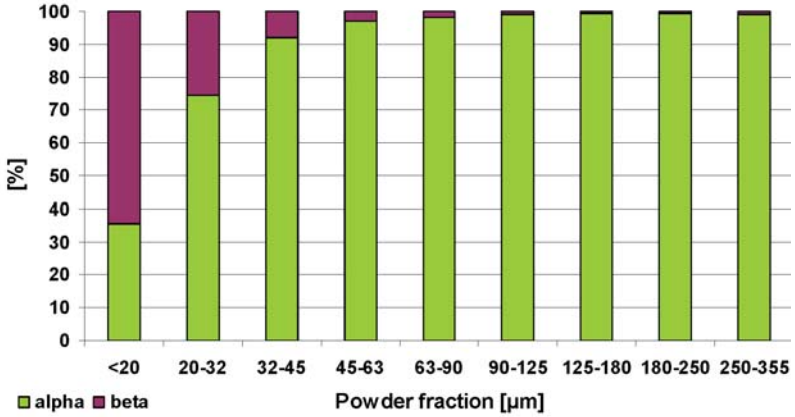


**(b)** Phase distribution of 10*Nb* powder

**Figure 7.2:** *TiAl-α* and *-β* phase composition of 5 & 10*Nb* powder fractions in volume percent. The data was obtained by diffraction at the HEMS-sidestation.

[3]high energy material science beamline

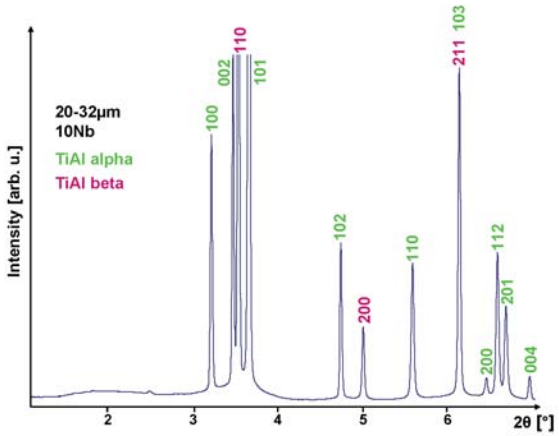


**(a)** 20-32 $\mu$m fraction, 10*Nb* alloy, 74.5% $\alpha$- / 25.5% $\beta$-phase

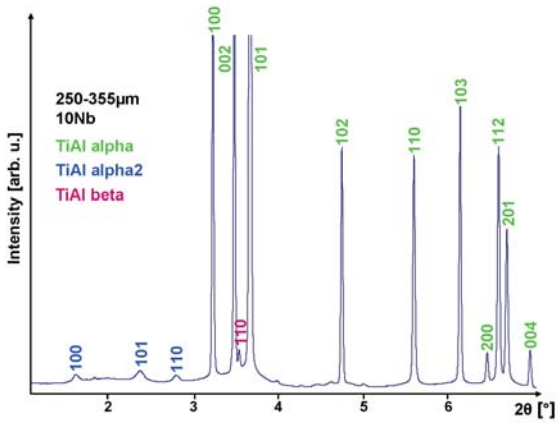


**(b)** 250-355 $\mu$m fraction, 10*Nb* alloy, 99.2% $\alpha$- / 0.8% $\beta$-phase, superlattice peaks of the $\alpha$2-phase

**Figure 7.3:** Reflexes of the pure $\alpha$- and $\beta$-phase (a) and of the superlattice phase $\alpha_2$, which formed in the biggest fractions as exemplarily shown in figure part (b) for the 250-355 $\mu$m fraction of the 10*Nb* alloy.

The data was reworked using the software fit2D (V12.077) from *A. Hammersley, ESRF* (Grenoble, France) while the subsequent data evaluation was done with powdercell 2.4 from *Federal Institute for Materials Research and Testing (BAM)* (Berlin, Germany). The phase composition is shown in Figure 7.2, while further details of the measurement and a complete sample overview is given in Appendix D.

The data-set shows an increased amount of $\alpha$-phase with increasing particle diameter. This is caused by the decreased cooling rate of the bigger gas-atomised powder particles, providing more time to reach a lower temperature phase constitution containing more $\alpha$-phase. Further on, the volume percentage of the $\beta$-phase in the 10*Nb* alloy powder is comparatively higher, due to the already known fact that it is stabilised by *Nb* [22].

The bigger particle fractions of 180-250 $\mu$m and 250-355 $\mu$m show furthermore slight peaks of the ordered phase $\alpha_2$ (Figure 7.3), again caused by the decreased cooling rate. The peaks of the $\alpha_2$-phase are slightly more pronounced in the 5*Nb* alloy. This effect is caused by the lower Nb amount in the 5*Nb* alloy, not restraining the diffusion processes which are necessary to develop the $\alpha_2$-phase out of $\alpha$.

## 7.4 EBSD on Ti-45Al-5Nb and 10Nb powder

### 7.4.1 2D & 3D EBSD on single particles

2D EBSD mappings on FIB processed cross sections were performed on single particles of the 10*Nb* alloy with sizes of roughly 20, 40 and 100 $\mu$m diameter. The used FIB acceleration voltage of 30 kV $U_{IHT}$ on all samples induced negligible FIB amorphisation damage. Although experiments by T. L. Matteson *et.al* found a better EBSD signal quality on FIB cross sections milled by lower FIB acceleration voltages [89], the resulting signal was sufficient to enable crystal labelling of the surface. Furthermore a better image quality was obtained by using comparably higher ion currents of some nano Ampere. The crossbeam workstation Auriga together with the EDAX software TSL-OIM provide 3D-EBSD[4]. Several 3D EBSD measurements on different powder particles of the 10*Nb* alloy could be performed in adequate times, which still means on the scale of days. However, not all measurements succeeded.
The main obstacle for the 3D-EBSD measurement is the correct positioning for every single FIB and EBSD step by the sample stage and the automated drift correction. During some 3D-EBSD measurements it happened occasionally that this wasn't done precisely enough, which led to a wrong positioned FIB cut, destroying the so far measured powder particle and thus disabling a meaningful continuation of the measurement.

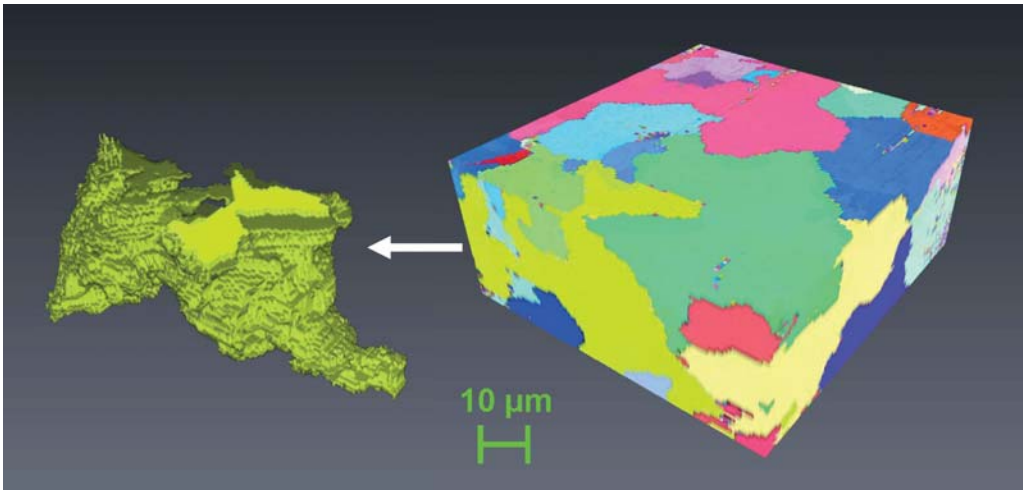


**Figure 7.4:** Cropped cube of 3D $\alpha$-phase grain structure of a 100 $\mu$m sized *Ti*-45*Al*-10*Nb* particle, sliced by a 2 nA FIB current. Each grain is arbitrary but unique coloured. The green grain (left side) was isolated out of the entire 3D body.

Due to this, no entire particle could be scanned slice by slice with EBSD, but fractions of up to half the size of a particle were completed. In Figure 7.4 the

[4]introduced in subsection 3.2.3

$\alpha$-phase grain structure of a powder particle with 100 $\mu$m diameter is presented in three dimensions. The measurement was performed at 20 kV $U_{EHT}$ and default 70° sample tilt. The EBSD slices as also the scan points of the measurement are both distanced by 600 nm. In this Figure the scan points are interpolated between the slices, done with the tomographic Avizo software. The isolation of the bright green $\alpha$-phase grain was done by a so called *watershed transformation* on accordingly selected, grey valued voxels, again performed with Avizo. It shows a compound of an apparently arbitrary grown $\alpha$-phase grain. A preferred growth direction could not be determined and the grains even grew partially around each other. The grains are not arranged in accordance to the cauliflower-like structures detected by BSE inside the particles.

### 7.4.2 EBSD on embedded powder fractions

To enhance the statistics of the phase composition measurements by EBSD, embedding and cross sectioning was performed, featuring a larger scan area with many single particle cross sections at once. The powder diffraction already revealed an increased $\beta$-phase amount for the smaller particle size fractions. Therefore the powder fractions <20 $\mu$m, 20 - 32 $\mu$m and 90 - 125 $\mu$m of the 10Nb alloy were selected and embedded in a conductive epoxy resin, consecutively grinded with 1200 and 2500 $\mu$m grained paper and finally polished by hand using a $SiO_2$ solution on a polishing disc wheel. The EBSD measurements were done at 20 kV $U_{EHT}$ and default 70° sample tilt with respect to the beam. The mapping of the 20-32 $\mu$m fraction was done on a larger region to obtain a comparable particle statistic regarding the <20 $\mu$m fraction.

The ratio of $\alpha$- to $\beta$- phase in the EBSD phase images was determined. For this the noise in the area between the particles had to be set to a homogeneous value like black, to read out the remaining pixels of the two colours green ($\alpha$-phase) and red ($\beta$-phase) in the pixel-histograms of the images.
This was done on the one hand by using the EDAX software TSL-OIM-Analysis 5.31. All pixels of the respective EBSD scan were indexed by a so called cleanup with a confidence value, calculated from the misorientations of the surrounding pixels. Subsequently a partitioning of the data was performed by setting a threshold to the confidence index, which resulted in an phase image without noise.
This determination of the phase fractions was proved in parallel by using photoshop from *Adobe systems* (San Jose, California, US), by tailoring masks out of the corresponding quality-images of the EBSD mappings. This masks were then used to cut off the noise between the powder particles. By changing the so called RGB colours to indexed ones, and by applying a subsequent colour-tone-separation to only *one* green and *one* red hue, the image pixel-histograms contained only three bars: one for the amount of black pixels, one for the green and one for the red. The frequency values were used to determine the phase composition in percent. The resulting image, from which the phase fractions were determined, is shown

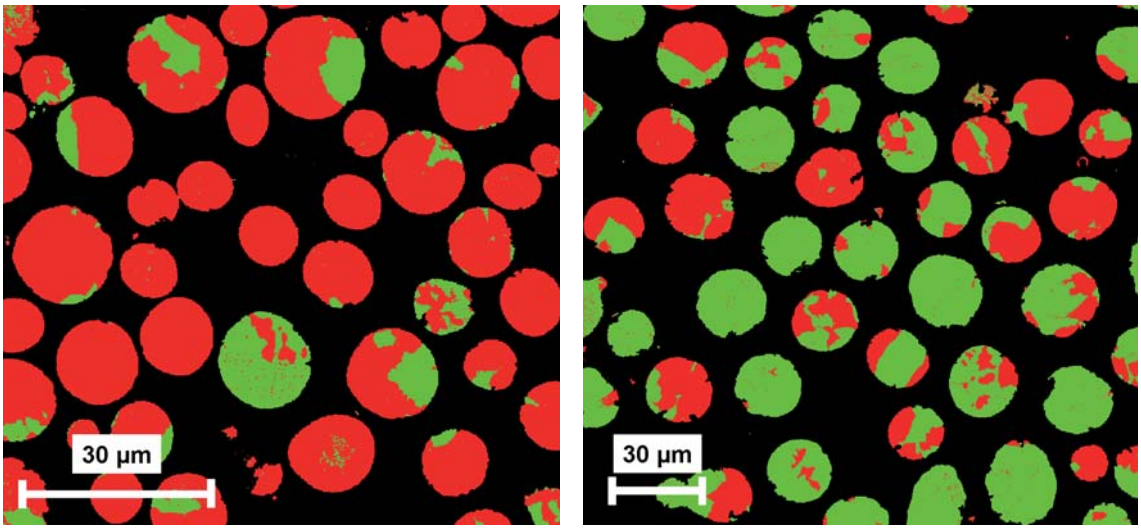


**(a)** <20 $\mu$m **(b)** 20-32 $\mu$m

**Figure 7.5:** EBSD mappings of resin embedded 10*Nb* powder fractions cross section; $\alpha$-phase (green) and $\beta$-phase (red).

in Figure 7.5.
The obtained phase fractions by both methods resulted in exactly the same values. The percentage of the <20 $\mu$m fraction is 14.7% $\alpha$- and 85.3% $\beta$-phase, while the 20 - 32 $\mu$m fraction revealed 64.1% $\alpha$- and 35.9% $\beta$-phase. Both showing values which are clearly higher by 10 - 20% for the $\beta$-phase than obtained by the diffraction experiment. However, this could be explained by the lower statistics compared to diffraction.

Numerous particles with $\alpha$-phase grain are not completely transformed from the primary $\beta$-phase. Figure 7.6 shows the crystal orientation of the $\alpha$- and $\beta$-grains of the sub 20 $\mu$m powder fraction scan, visualised on the basis of the previously noise cleaned data by the EDAX software. As a result no preferred crystal orientations in radial direction can be determined.

The EBSD scan of the 10*Nb* alloy 90 - 125 $\mu$m powder fraction was equally reworked by the described noise cleanup using the EDAX software. The phase composition of Figure 7.7 part (a) shows only 0.4 % $\beta$-phase amount, like expected by the results of the previously performed powder diffraction. The $\beta$-phase is only present in very small satellite particles and no $\beta$-phase grains are present in big particles. In Figure 7.7 part (b) again no preferred orientations can be detected.

The *Ti*-$\alpha$-phase grains are usually supposed to be transformed out of *Ti*-$\beta$-phase grains [53]. When the *Ti*-$\beta \rightarrow$ *Ti*-$\alpha$ transformation obeys the Burgers orientation relationship [19] each *Ti*-$\beta$ orientation would result in 12 possible *Ti*-$\alpha$ orientations. The $\alpha$-grains growing from the same parental $\beta$-grain are thus characterised by related misorientation angles. Gey and Humbert showed that grains do stem from the same parent *Ti*-$\beta$ grain when the misorientation angles 10°53′, 60°, 60°83′,

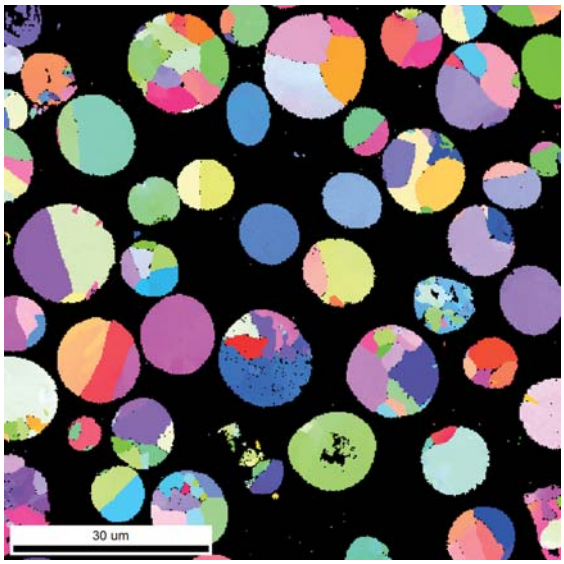


**(a)** Crystal orientation

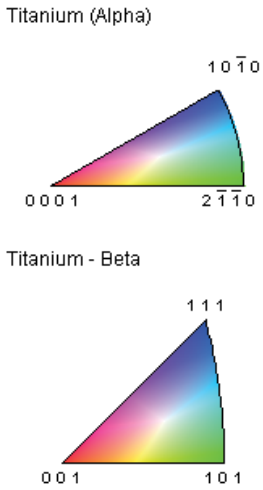


**(b)** legend

**Figure 7.6:** Crystal grain orientation image of the 10*Nb* sub 20 $\mu$m powder fraction, without detectable preferred radial orientation of the mainly $\beta$-phase grains.

63°26′ or 90° are measured by EBSD for neighbouring *Ti*-$\alpha$ grains [41].
Therefore the misorientation of neighbouring $\alpha$-grains was evaluated for the performed EBSD scan for the 90 - 125 $\mu$m fraction, depicted in Figure 7.8. However, no preferred misorientation angle could be detected, as already the 3D image of a 100$\mu$m in Figure 7.4 let to assume. Hence, one finds that the $\alpha$-grains are not formed out of already solidified $\beta$-grains according the Burgers relationship [19] by a solid state phase transformation.

Finally, initial $\beta$-grains are formed out of the melt during cooling, since the $\beta$-phase is generally preferred to be primarily formed [133]. The cauliflower structure is giving proof that diffusion took place during the solidification of the initial $\beta$-grains, resulting in an unequal distribution of the alloying elements. The solidification interval $\Delta T_0$ (subsection 7.1.2) presumably allowed the solidification of initial $\beta$-grains by diffusion of the heavier elements into the grain formation area, while further amounts of the lighter element *Al* remained in the interstices, represented by the darker regions of the cauliflower structure in the BSE images. However, the dendritic cauliflower structure is not correlated with the $\beta$-grain orientation (Figure 7.6).
In the following the hexagonal-close-packed $\alpha$-phase is possibly originated by a martensitic phase transition from the body-centred-cubic $\beta$-phase as observed for *Ti*-48*Al* powder [90], driven by the extremely fast cooling rates. Although there was found no significant orientation relationship between the $\alpha$-grains this diffusion less transition would be possible on such a time scale [126].

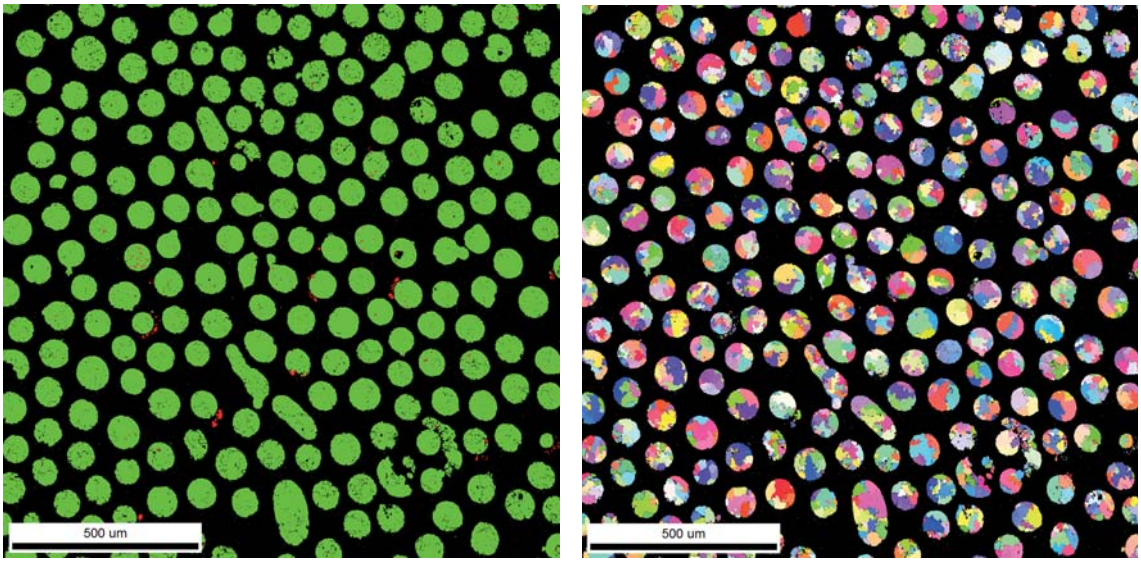


**(a)** Phase composition **(b)** Crystal orientation

**Figure 7.7:** Phase composition of the 10*Nb* alloy 90 - 125 $\mu$m powder fraction, $\alpha$-phase (green) and $\beta$-phase (red) (a). No preferred crystal orientations in radial direction are present (b) (refer to the legend of Figure 7.6 part (b)).

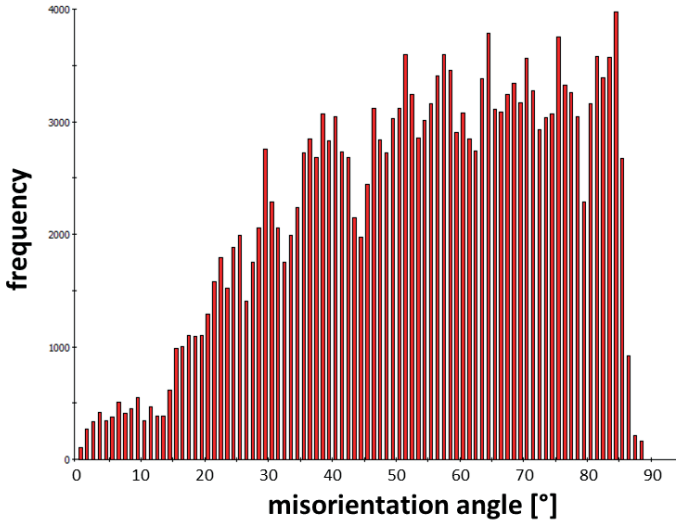


**Figure 7.8:** Misorientation histogram of neighbouring $\alpha$-grains of the 10*Nb* alloy 90 - 125 $\mu$m powder fraction EBSD scan (compare to Figure 7.7 part (b)).

## 7.5 Sample preparation for IBL

For contrast testing of the powder material regarding the planned SRnCT experiment, some lamellas out of 40 and 100 $\mu$m sized particles from both alloys were produced by FIB to perform a radiography. In Figure 7.9 part (a) such a lamella is shown, which was milled out of the particle by using the so called rocking stage technique, in order to achieve the best possible homogeneous thickness throughout the entire disk. By using this technique the lamella is turned after milling from one direction to mill additionally from the opposite side.

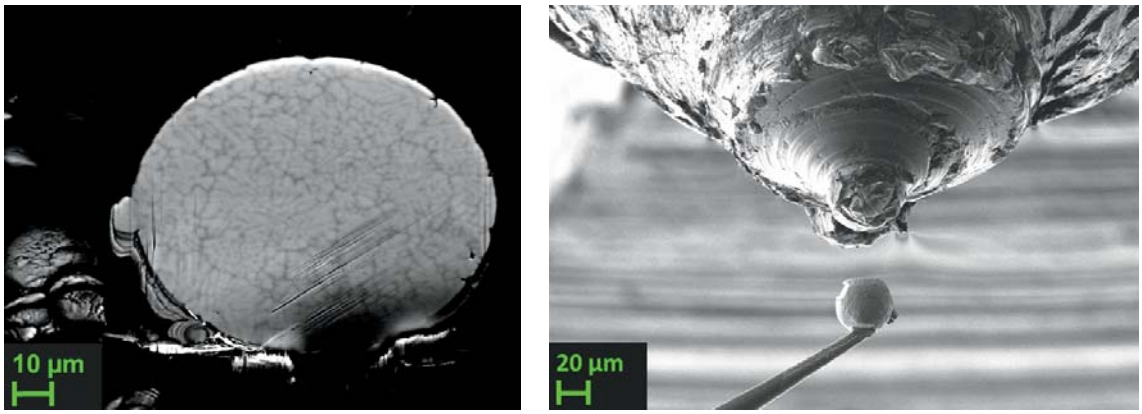


**(a)** FIB milled lamella from a 100 $\mu$ sized particle

**(b)** 40 $\mu$m sized particle

**Figure 7.9:** (a): FIB milled lamella from *Ti*-45*Al*-10*Nb* particle, with a thickness of about 5 $\mu$m on top, visualised by the BSE-detector at 20 kV $U_{EHT}$ and 10 mm WD. The diagonal stripes are curtaining residuals, directionally caused by the applied rocking stage technique. (b): 40 $\mu$m sized particle from 10*Nb* alloy attached to the manipulator, prepared to be attached on the IBL sample holder (FIB image (30 kV, 50 pA), 5 mm WD, SE2-detector).

The lamellae were transferred to respective IBL sample holders similar to the described FIB sample preparation method for IBL (subsection 3.3.2) and could be investigated in radiographic projections by the SRnCT setup. However, the inner material composition did not show enough contrast on the resulting image to clearly distinguish between optical artefacts and the dendritic structures (e.g. Figure 7.10).

In a second pre-testing of the *Ti*-45*Al*-10*Nb* powders for SRnCT, several particles were attached to IBL sample holders (Figure 7.9 part (b)), using the introduced FIB specimen preparation method. Those were now imaged by SR$\mu$CT at IBL due to the expected stronger contrast by this method, but the chemical variation in the particle interior was again not sufficient. The achieved contrast was in the range of the contrast of occurring ring artefacts and could not be filtered out by adequate software procedures. Therefore the samples are not suited to be imaged by SRnCT.

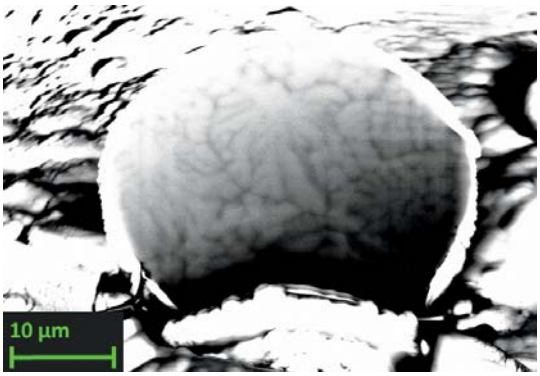


**(a)** FIB milled lamella from a 35$\mu$m sized particle

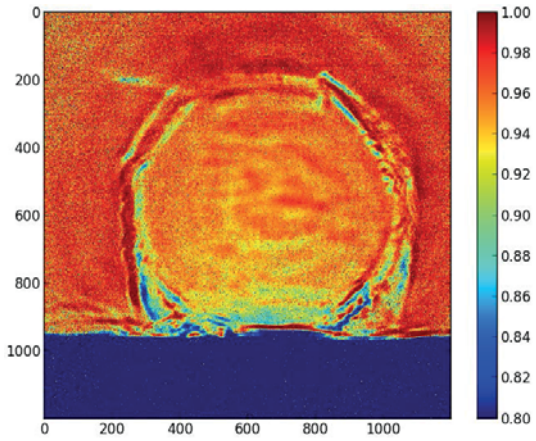


**(b)** Related radiographic by IBL with relative attenuation scale

**Figure 7.10:** (a): FIB milled lamella from *Ti*-45*Al*-5*Nb* particle, with a thickness of about 1,2 $\mu$m on top, visualised by the BSE-detector at 20 kV $U_{EHT}$ and 11,8 mm WD under an angle of 36° stage tilt. (b): attenuation image obtained by synchrotron radiography at the nanotomography experiment at IBL using x-rays with 13 keV.

## 7.6 Summary

The phase composition was determined by X-ray scattering at the HEMS side station (beamline P07b) at PETRA III, as well as by SEM, EDX, 2D and FIB based 3D EBSD measurements.
The *Ti* $\alpha$ phase is dominant fraction in almost every powder fraction that was investigated, except for the <20 $\mu$m fractions. Regarding the *Ti*-45*Al*-5*Nb* alloy one finds considerable amounts of the $\beta$ phase only in fractions smaller than 32 $\mu$m. For the *Ti*-45*Al*-10*Nb* alloy this was similar but for powder fractions smaller than approximately 45 $\mu$m. The total $\beta$ phase amount in 10*Nb* fractions was generally higher, as expected for a higher *Nb* content [22].
It was found that the dendritic cauliflower-like structures of bigger particles of *Ti*-45*Al*-10*Nb* are more pronounced than for the 5*Nb* alloy, and smaller particles contain in average less *Nb*. The presence of dendritic structures as well as the calculations in subsection 7.1.2 showed that the cooling rate during powder atomisation was still too low to reach the critical growth rate for absolute stability and thus a planar solidification. By the absence of preferred misorientation angles one finds that $\alpha$-grains are not formed out of already solidified $\beta$-grains according the Burgers relationship [19] by a solid state phase transformation.

Finally, initial $\beta$-grains were formed out of the melt during cooling, since the $\beta$-phase is generally preferred to be primarily formed [133]. The BSE detected cauliflower structure is giving proof that diffusion took place during solidification of the initial $\beta$-grain formation, even though there is no relation between the grains and the dendrite structure. Regarding the occurring, still extremely fast cooling

rates of $10^6$ K/s [113], the hexagonal-close-packed $\alpha$-phase is possibly originated by a martensitic phase transition from the body-centred-cubic $\beta$-phase. However, a significant orientation relationship of the $\alpha$-grains is missing.

Regarding SRnCT the specimen could be successfully prepared by the described FIB method, but the preliminary SRnCT and SR$\mu$CT experiments revealed an insufficient attenuation. However, this samples are also appropriate to perform phase contrast experiments at IBL in the future.

To enable a FIB tomography by BSE contrast the BSE-detector of the Auriga should be slightly modified by a wedge shaped cutout of the frame scaffold, if possible, to allow the *in situ* usage with the FIB. Otherwise a pneumatic BSE-detector would be needed to provide an automated detector insertion to enable this.

# Chapter 8

# Applications: Preparation of Norway spruce for X-ray investigation

Cellulose is the most frequent biological polymer in nature, often combined with an amorphous matrix. This composite material has outstanding mechanical properties, but is characterised by low material density. That is basically due to the hierarchical structure of cellulose from the molecular over the crystalline level to crystal cellulose chains, the microfibrils. For materials research it is of interest to understand their functionality to adapt this construction principle. X-rays are used to investigate the mechanical properties of these materials [127].

Although the molecular composition and the role of the microfibrils are already known [101], cellulose is still a topic of further investigation. While e.g. the cellulose structure of softwood cells, so called tracheids, is already well known, the mechanical functionality as well as the structure of the 50 - 100 nm thick transition layer between two main cell walls are still unknown [27; 107].
The investigation of this transition layer by position resolved X-ray scattering is hampered by two reasons. First it is recommended that the samples are cut perpendicular to the cell axis as precisely as possible to allow the determination of the cellulose orientations in the cell wall transition layer. Preparation attempts with bad alignment, as e.g. by an cryo-microtom, were not sufficient. Hence, the specimen preparation by the Auriga (section 3.2) is considered, featuring a detailed magnified image of the cell orientation, enabling the perpendicular cut by FIB milling. Furthermore the splintering by mechanical methods is avoided too.
On the other hand a beamline with a nano-sized X-ray beam is necessary to explore those thin transition layers. In the following the nanofocus endstation of the MiNaXS[1] beam line (P03) at PETRA III at DESY (Hamburg, Germany) and of the beamline ID13 at the ESRF (Grenoble, France) were used for this.
The disadvantage of a nanofocused X-ray beam is the increased radiation damage for biological samples, due to the drastically increased flux density. The main part

[1] introduced in subsection 2.5.2

of the X-ray energy deposited in the specimen originates from the photoelectric effect[2] and leads to the primary radiation damage. This is followed by the time dependent secondary radiation damage induced by resulting radiolytic products as free radicals and secondary electrons. This second radiation damage can be reduced by cryo-cooling [39].

## 8.1 Introduction to cellulose

In the plasma membranes of plant cells uridine-diphosphoglucose (UDP-glucose) is synthesised by the enzyme saccharose-synthase from the photosynthetic products. For upper plants UDP-glucose becomes then catalysed to cellulose chains by cellulose-synthase rosette complexes [71]. The catalytic subunits are coded in so called CesA-genes [51]. The rosette complex itself is made of six catalytic sub units which again consist of six cellulose-synthase units.
Therefore up to 36 cellulose chains are synthesised at once by a single rosette complex. Driven by van-der-Waals forces and hydrogen bonds this simultaneously synthesised chains form a semicrystalline microfibril. Dependent on the biological derivation those microfibrils are 3 - 5 nm wide and some $\mu$m long [100]. Besides few special cases, plants and bacteria synthesise these cellulose chains into two crystalline variations, triclinic cellulose $I_\alpha$ and monoclinic cellulose $I_\beta$. Both structure variations naturally occur even in a single microfibril in parallel [71].
The main difference between both crystalline cellulose types is the kind of displacement of the chain planes for the value of $\frac{c}{4}$ along the chain axis[3], which is alternating for $I_\alpha$ but continuously shifted for $I_\beta$ [101].

The microfibrils are usually twisted in parallel around the cell in direction of the cell axis (Figure 8.1). The microfibril angle $\mu$ is crucial for mechanical properties by determining e.g. the modulus of elasticity of the material [71].


**Figure 8.1:** Helical order of microfibrils in the cell wall by angle $\mu$ with respect to the cell axis [127].

By linking cellulose with the biological polymers hemicellulose, pectin and lignin the cell wall is stabilised and height growth is possible. Further extracts like fats,

[2] introduced in subsection 2.3.1
[3] $\vec{c}$ is the unit cell vector in chain direction.

pigments, starch etc. determine the characteristics of plants, like e.g. flammability and resistance against vermins [127].

## 8.2 Cellular structure of soft wood

In a thin cylinder jacket called cambium, located in between marrow and bark, wood cells are formed, growing in two directions. The ones growing to the inner direction are called xylem while that ones growing to the outer direction are called bast. Apart from the pith rays which are in charge of the water supply in radial direction, soft wood is build by only two different kinds of cells, the tracheids and the parenchyma cells. The tracheids occur with about 90 % and are in charge of water transport and consolidation, while the parenchyma cells are dedicated to nutrition supply.
Tracheids are needleshaped, long stretched cells, that are connected among themselves via bordered pits, as pictured in Figure 8.2. They measure about 1 - 4 mm in length with a transverse cross section of approximately 25 - 45 $\mu$m. The shape of the transverse cross section is varying, close to the marrow it is ring shaped while to the bark it is rectangular. The cell wall structure of the tracheids is produced successively by the biologically active part of the cell, the so called lumen [127].

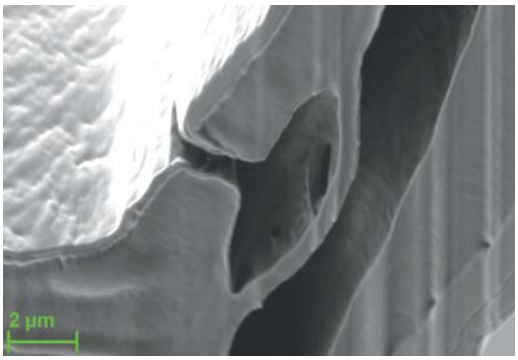


**Figure 8.2:** Bordered pit in the cell wall of a soft wood tracheid, connected to an interstice between the cells (2 kV $U_{EHT}$, 4.7 mm WD, SE2-detector).

Before cell growth ends, the secondary cell wall is going to be formed, which is usually separated in two layers which are characteristic in thickness, cellulose amount and alignment of the microfibrils. The first secondary (S1) wall is attached to the inner surface of the primary wall and has a thickness of about 200 nm. This cellular wall features for the first time ordered structures in the cell wall. The amount of the cellulose fibrils is about 35 %, and the microfibrils angle $\mu$ is between 70° and 90°. The second secondary (S2) wall has a thickness of 1 - 5 $\mu$m with a cellulose amount of about 60 %. The microfibrils angle $\mu$ is in the range of 1 - 59°, thus significantly smaller.
The crystal size of Norway spruce (*Picea abies*) wood is in $\vec{a}$ direction 3 nm and in $\vec{c}$ direction 35 - 36 nm [80].

## 8.3 Introduction to X-ray scattering on wood

Constructive interference patterns of fibres can be obtained by X-ray scattering if a fibre texture is given by any crystal axis which is aligned to the longitudinal axis of the fibre. In our case this is given by the $\vec{c}$ axis of the cellulose crystals. The other crystal axes are therefore rotationally directed to the main axis and are aligned in arbitrary directions. X-ray scattering on a fibre generates a typical fibre pattern which can be well illustrated by using the Ewald-construction [127].

To detect the orientation of the microfibrils in the cell wall layers it is recommended to align the longitudinal cell axis in parallel to the beam. By this the scattering signals of front- and backside-microfibrils of the cell do not superimpose [82]. The cylindrical microfibrils appear ringshaped in reciprocal space, tilted by the angle $\mu$. The diffraction reflexes are formed where the Ewald sphere cuts these rings. For details on the microfibrils diffraction patterns please refer to Paris and Müller [105].

### 8.3.1 Preliminary results by diffraction on wood

In order to elucidate the context of the FIB sample preparation presented here, first results of specimens prepared and measured in a similar way as planned here by S. Storm at the nanofocus endstation of the MiNaXS beam line (P03, DESY) are presented [127].

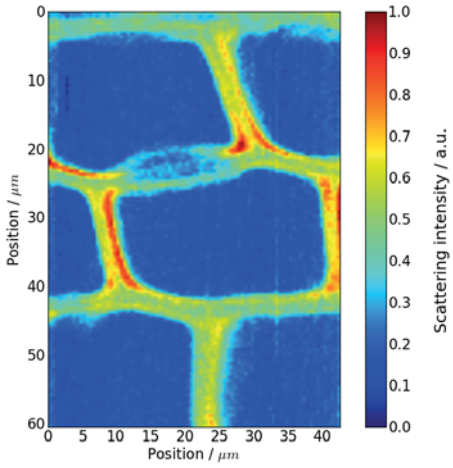


**Figure 8.3:** Normalised cellulose reflex intensity of mesh scan on wood in real space [127].

It was originally planned by Storm to attach a FIB processed wood lamella to a 50 nm silicon-nitride-membrane using the manipulator. This membrane is extremely sensitive to any touch, and even to interaction with the ion beam. That made it impossible to bring the sample to the membrane by the manipulator directly. Hence, a fixation on the membrane by GIS and FIB was not possible. Therefore Storm finally had to use *non*-FIB prepared samples for a first beam time at the MiNaXS endstation. Those samples had been already cut by the Finnish wood research institute *METLA*, by using a cryo-microtom, featuring a thickness of 25

$\mu$m. The annual ring of the sample was from the year 1987 while that of a second, not fertilised reference sample, was from 1986.
Nevertheless, the surfaces of the sample and its reference could be significantly improved by a FIB after-treatment and were thinned down to a thickness of 15 and 17 $\mu$m respectively. During the FIB treatment they were clamped on a sample holder and afterwards, due to their comparably big lateral size, the sample and its reference could be taken by tweezers to the diffraction sample holders, a copper slit and a silicon-nitride-membrane respectively. The normalised cellulose reflex intensity of a mesh scan on the reference wood sample is shown in Figure 8.3. A bordered pit is visible connecting the upper left and the middle tracheid, similar to the SEM image of a bordered pit in Figure 8.2. Most of the vertical S2 cell wall layers are nicely visible by strong scattering. Under the assumption of a beam parallel to the cell axis, the introduced vertical microfibril angle $\mu$ and the additional horizontal microfibrils orientation angle $\alpha$ could be calculated out of the obtained data (Figure 8.4).

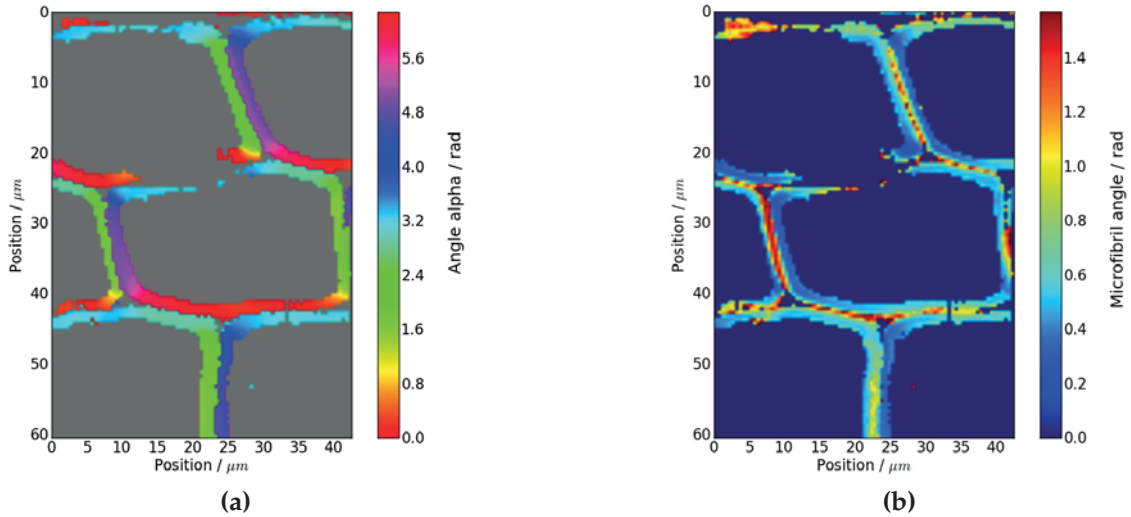


**Figure 8.4:** Local variation of $\alpha$ (a) and $\mu$ (b) determined by a mesh scan on the reference wood sample [127].

## 8.4 Results by FIB sample preparation

In the following the FIB lamellae processing in the scope of this thesis is described. The samples were obtained from the Finnish wood research institute *METLA*, originating from a fertilisation experiment in southern Sweden. When the trees (*Picea abies*) were 14 years old they became fertilised and additionally watered for up to 16 years. However, the fertilisation experiment was no object of the following investigations. The obtained samples are tangentially cut and about 1 mm thick, taken from different annual rings. To investigate the transient

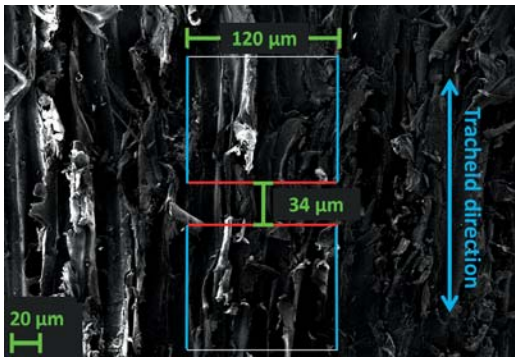


**(a)** Alignment along tracheids axes for FIB cutting (FIB image (30 kV, 50 pA), 5 mm WD, SE2-detector)

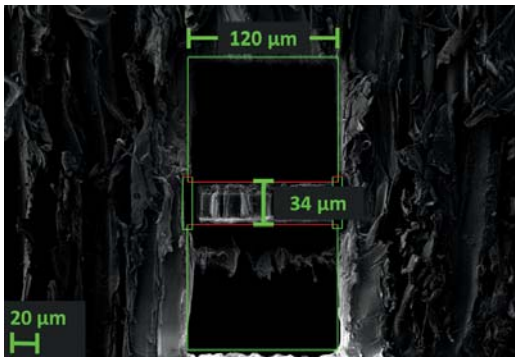


**(b)** Excavation of wood lamella (FIB image (30 kV, 50 pA), 5 mm WD, SE2-detector)

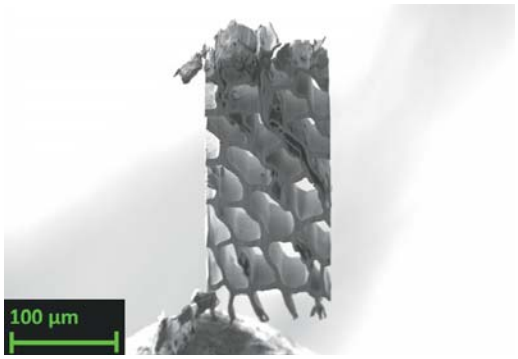


**(c)** Wood lamella on IBL sample holder (2 kV $U_{EHT}$, 4.8 mm WD, SE2-detector)

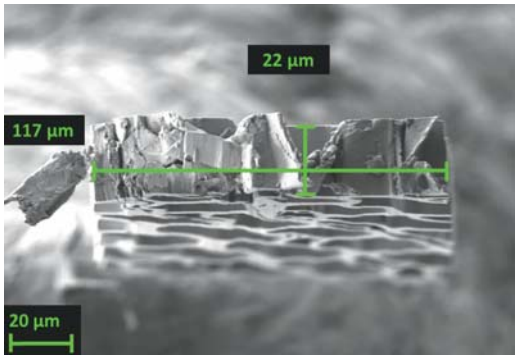


**(d)** Thickness of lamella (2 kV $U_{EHT}$, 4.8 mm WD, SE2-detector)

**Figure 8.5:** FIB specimen preparation from soft wood, sample A (*Picea abies*).

layer between the S1 and S2 cell wall by X-rays, the specimen have to be prepared with high accuracy regarding perpendicularity of the tracheids longitudinal axis to the cutting direction.
For the following experiments a sample from 1997 was chosen, that comes from a tree which got the fertilising treatment for ten years. The annual ring of the fertilised tree was grown comparably fast and is quite big. The original obtained samples were initially cut by a scalpel to 3 mm × 5 mm big pieces. These pieces were mounted with conductive silver glue onto the SEM sample holder. Regarding sample charging it was very useful to draw the conductive silver over the edges of the sample, and to chose a milling region close to such a conductive edge but still without silver contamination. The specimens were excavated by FIB to achieve the desired lamella structure, with a sample thickness of 10 $\mu$m - 22 $\mu$m.

Regarding the fixation on a sample holder, the sample preparation method described in subsection 8.3.1, was tried initially once more. By reducing the sucking tension of the SE2-detector and by using only the FIB for imaging during op-

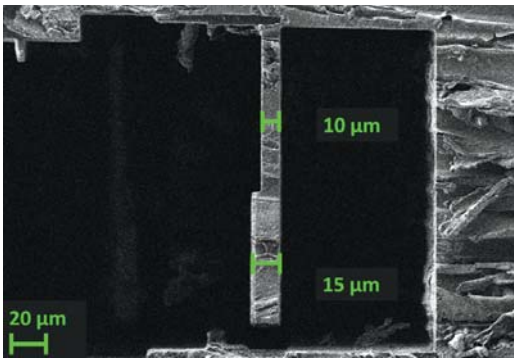


**(a)** Excavated lamella with varied thickness (FIB image (30 kV, 50 pA), 5.1 mm WD, SE2-detector)

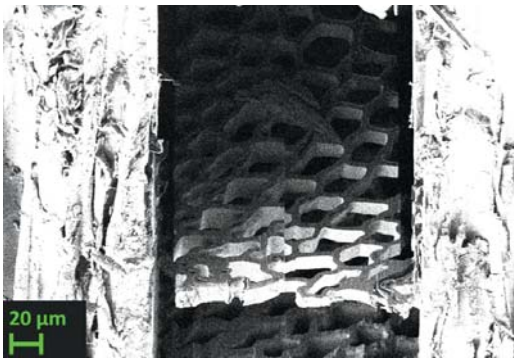


**(b)** Lamella before lift out (FIB image (30 kV, 50 pA), 5 mm WD, SE2-detector)

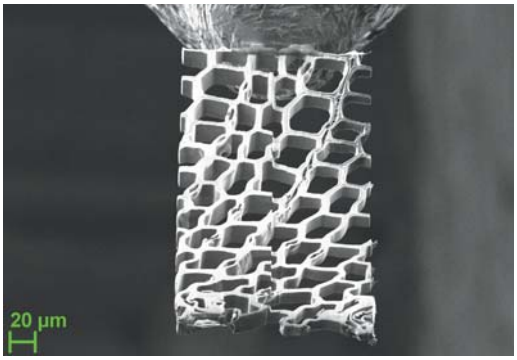


**(c)** Wood lamella on IBL sample holder (FIB image (30 kV, 50 pA), 5.1 mm WD, SE2-detector)

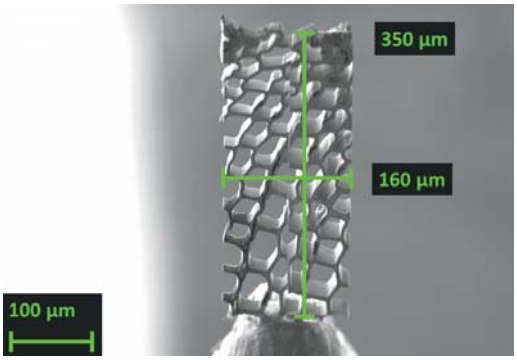


**(d)** Expansion, switched side in comparison to (c) (2 kV $U_{EHT}$, 4.6 mm WD, SE2-detector)

**Figure 8.6:** FIB specimen preparation from soft wood, sample B (*Picea abies*), with 10 and 15 $\mu$m thickness. Lamella size measured with tilt correction (d).

eration, two lamellae were put successfully to a silicon-nitride-membrane, only by cutting off the connection between manipulator and lamella using FIB whilst above the membrane. The lamellae should statically attach to the membrane. One of the lamellae finally laid at the very edge of the membrane, but by trying to move it the membrane was destroyed. The other lamella got lost in the specimen transport box before it could be delivered. Obviously it was not reliably attached to the membrane by only putting it on the membrane surface.

Finally the method was considered anew. As a result the IBL sample holder (Figure 2.14) was used in the following to attach the FIB processed lamella, providing transport and measurements. The whole procedure was identical to the sample preparation for nanotomography in subsection 3.3.2. Additionally, the wood lamellae must be attached very well to the IBL holder, due to the leverage forces caused by the increased size compared to 40 $\mu$m ranged pillars for nanotomography. The first successfully FIB processed wood lamella by this method (sample A) is shown in Figure 8.5. By accident this lamella was almost perfectly parallel

to the flat side of the IBL sample holder, which was significantly enhancing the alignment during the X-ray experiment.
The size of this lamella (sample A) with 238 $\mu$m × 119 $\mu$m × 22 $\mu$m is still small compared to the subsequently prepared one (sample B) in Figure 8.6, which also features two different thickness regions by 10 $\mu$m in the left and 15 $\mu$m in the right part of the lamella to enhance the variation possibilities during synchrotron measurement. In Figure 8.6 part (b) the lamella is prepared for manipulator lift out with only one connection point left (lower right edge). Figure part (c) shows the multiple attaching points between lamella and IBL holder, necessary for huge samples like those. Due to the general upside down scanning direction of the FIB, all objects, as now the wood lamella, appear upside down in FIB images at stage tilt angles of below 54°. Figure part (d) depicts the size of this lamella of 351 $\mu$m × 159 $\mu$m. The FIB processed specimen was so big that the depth of focus could only cover the centre of the image. Although the measured vertical value was taken at a stage tilt of 45° it is real because of the applied tilt correction, which is stretching the image in vertical direction with respect to the applied tilt correction angle of also 45°. The lower left part of the lamella Figure 8.6 (d) shows an irregular structure on the tracheids inner cell wall, which is supposed to be FIB damage.

The specimen on the IBL sample holders were safely transported to the respective beam lines between flexible membranes by commercial available transport boxes.

### 8.4.1 Tracheid preparation for SRnCT

A single tracheid was prepared partially to image its 3D features by SRnCT at IBL (Figure 8.7). The preparation of the single tracheid was done according to the FIB specimen processing method for IBL introduced in subsection 3.3.2.

The radius of this sample exceeds almost the limitations of the SRnCT experiment. Regarding the height of 150 $\mu$m the specimen can be imaged by several height steps (Figure 8.7 part (d)).
To increase the contrast of the tracheid it was laid in Iodine ($I$) solution. Unfortunately it got lost during this procedure. With its small structures, as the bordered pits, it was highly suitable for SRnCT. Such a sample should be processed anew, this time subsequently to the immersion in $I$.


**(a)** Attached to the manipulator (FIB image (30 kV, 50 pA), 5 mm WD, SE2-detector)

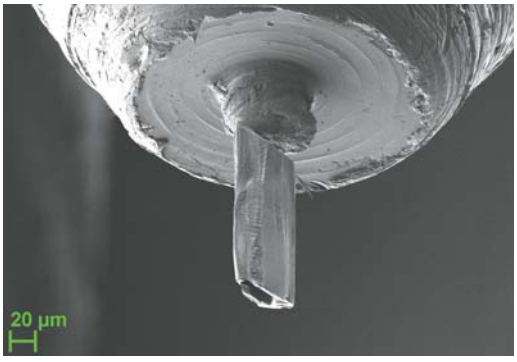


**(b)** Attached to the IBL holder (FIB image (30 kV, 50 pA), 5 mm WD, SE2-detector)

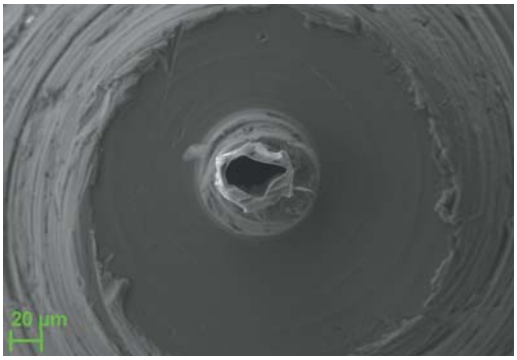


**(c)** Top view of tracheid (20 kV $U_{EHT}$, 4.8 mm WD, SE2-detector)

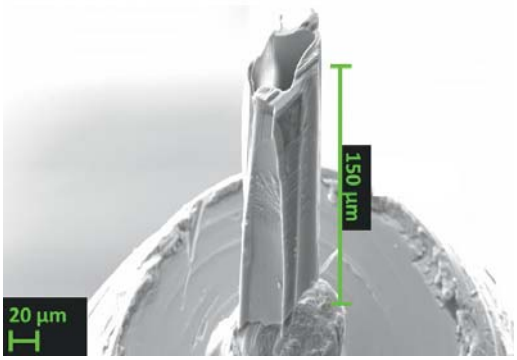


**(d)** Side view with tilt correction (20 kV $U_{EHT}$, 8.8 mm WD, SE2-detector)

**Figure 8.7:** Single tracheid pillar preparation with a length of about 150 $\mu$m.

## 8.5 Diffraction results and FIB damage

The first FIB prepared lamella (sample A) was investigated at the endstation of the beamline ID13 (ESRF). The mounting of the specimen was extremely precise and hardly no additional alignments were necessary.
The step size of this mesh scan was 200 nm × 400 nm[4], with a beam size of > 100 nm × 100 nm. At every scan step the sample was exposed for 0.5 s to the beam with an energy of 14.9 keV. As detector a FreLon Camera was used.
An image composed of single diffraction patterns obtained by a mesh scan on a cell wall of three adjacent tracheids is shown in Figure 8.8.

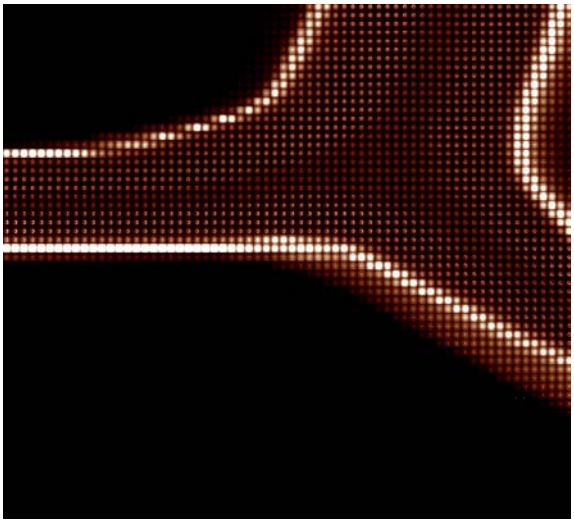

**Figure 8.8:** Image of a wood cell wall by composed diffraction patterns, obtained by nano focus X-ray scattering at the beamline ID13 (ESRF) on sample A.

A strong fluorescence signal is detected at the inner edges of the cell walls which is overexposing the cellulose diffraction. Only few images from the edge the fluorescence reach their maximum and the diffraction is invisible. Therefore the desired diffraction patterns of the thin S3 cell wall layer could not be obtained and became separated from the adjacent broader S2 layer which is also partially affected.
The emission lines of the main softwood elements *C*, *O* and *N* are absorbed efficiently for they are situated below 1 keV. Hence, the increased brightness of the diffraction images on the edges of the cell wall must be affected by incorporated *Ga* from the FIB milling during specimen processing. Since this is visible on all inner cell walls it is probably vaporised *Ga* redepositing during the FIB processing on all surfaces like an environmental effect. Regarding the maximum position of the *Ga* fluorescence the ions seem to be incorporated in a depth of about 1 $\mu$m [128].
The second FIB prepared lamella (sample B), featuring two thickness regions, was investigated by line scans in vertical direction at the nanofocus endstation of the MiNaXS beam line (P03, DESY). The step size in the first 10 $\mu$m thick scanning

[4]horizontal × vertical

region was 333 nm × 333 nm[5] and the one in the second 15 $\mu$m thick region it was 200 nm × 1.5 $\mu$m, with a beam size of 250 nm × 350 nm. Due to the lower flux compared to the previous measurement at ESRF the exposition time had to be increased. At every scan step the sample was exposed to the beam for either 10 s regarding the 10 $\mu$m thick region, or for 4 s regarding the 15 $\mu$m thick region. The beam energy was set to 14.7 keV. The scattered signal was measured by a PILATUS-detector using an energy threshold of 12 keV. To avoid secondary radiation damage it was tried to cryo-cool the sample, but this failed due to vibrations induced by the cryo-stream. In Figure 8.9 two scatter images of the sample B are shown. Figure part (a) shows the *Ga* fluorescence caused by the incorporated FIB ions. Again, the depth of implemented *Ga* ions is about 1 $\mu$m.

The absence of diffraction patterns in the *Ga* affected region could be caused by two reasons. On the one hand the crystal structure of the cellulose chains is possibly destroyed by the disruption of the weak hydrogen and van-der-Waals bonds. On the other hand the applied energy gives rise to enhanced radiation damage. Regarding the primary radiation damage by a 160 times higher photoabsorbtion of *Ga* compared to *C*, and by the *Ga* K shell fluorescence lines in the range of 10 keV regarding the secondary.
By [60] it is reported that wood becomes brittle by an electron beam, which may explain in combination with long milling times the so far not reported penetration depth and high concentration of implemented *Ga*. More details on the corresponding radiation damage are given in a jointly published paper by S. Storm *et al.* [128].

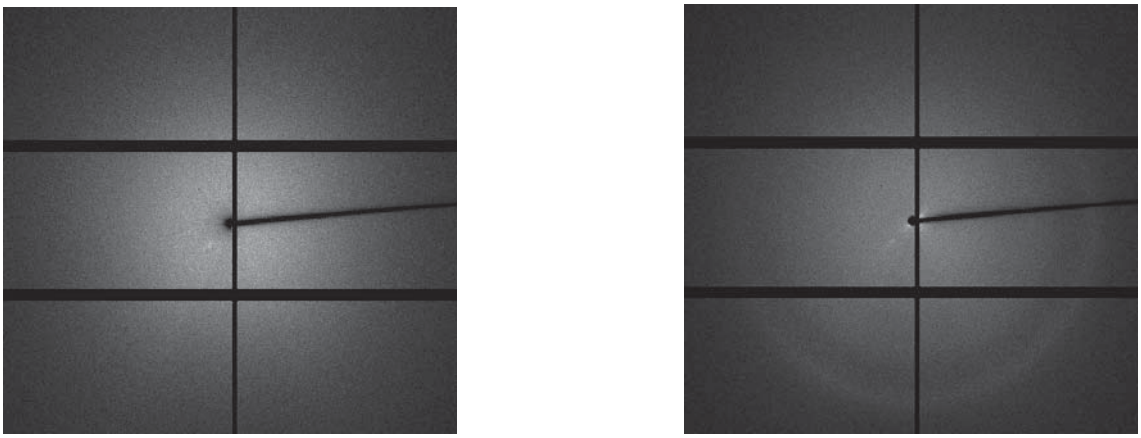

**(a)** *Ga* fluorescence

**(b)** *Ga* fluorescence with diffraction

**Figure 8.9:** *Ga* fluorescence on FIB processed wood lamella.

[5]horizontal × vertical

## 8.6 Summary

The jointly published paper [128] reports for the first time the investigation of a FIB-processed biological sample by scanning X-ray nanodiffraction.
The introduced FIB specimen processing method for IBL (subsection 3.3.2) was successfully applied to the wood lamella preparation. The perpendicular orientation of the tracheids in the wood lamellae could be precisely achieved by this sample preparation method. The ability of the Auriga workstation to image less conductive material at low voltages was a benefit too. The parallel orientation of a lamella to the flat side of the IBL sample holder, as experienced for sample A, should be applied in future to enhance the alignment procedure during the subsequent X-ray experiment.

At the measured energies the obtained diffraction images prove a strong *Ga* incorporation on the inner edges of the cell walls by a strong fluorescence signal. Even though the FIB milling enabled a very defined cross sectioning and surface preparation of the FIB-processed specimen, the *Ga* incorporation hindered the investigation of the affected cell wall layer S3.
To lower the penetration depth of *Ga* the milling process could be performed at lower voltage or even be followed by subsequent polishing with an inert gas beam. Furthermore, the cryo-cooling should be enabled by appropriate sample fixation and connection to avoid secondary radiation damage.
Finally, despite the damage in the S3 and partially the S2 cell wall layer the remaining cell wall seems to be intact and this method can still be used nicely to investigate the S1 and main parts of the S2 layer.

# Chapter 9

# Applications: SRnCT on photonic glass

In the field of photonics novel materials are engineered by arranging an internal microstructure of a dielectric, effecting new optical properties which are unexpected for homogeneous media. One example are so called photonic crystals, where the dielectric function varies perfectly periodic on the length scale of the respective light wavelength, featuring anomalous refraction, super-refraction, small group velocity, and for certain structures even the opening of a complete photonic bandgap [37].

Using a dielectric sphere with a size comparable to the wavelength of light as building block, two extreme systems can be built: the mentioned ordered arrangement (a photonic crystal) or a completely random arrangement of spheres, a photonic glass. The most important property of both solid systems is the monodispersity of the building blocks that compose them, offering a new range of interesting phenomena [38].

Due to the resonant behaviour of the spheres there exist discrete light states and every sphere acts as a meta-atom for light. Interesting new optical phenomena have already been studied in random media such as coherent backscattering enhancement, Anderson localization of light and random lasing [37].

## 9.1 Photonic glass of zirconium dioxide spheres

Random packing of hard spheres was used as a model during the last decades to pack objects efficiently [10]. Via a currently advanced self-assembling technique disordered photonic glasses can be obtained [38]. These random materials are solid thin films, exhibiting rich novel light diffusion properties originated from the optical properties of their building blocks.

Particularly, a photonic glass sample made of 2 $\mu$m sized zirconium dioxide spheres was investigated. It was obtained from Jean do Rosario [67], affiliated

to the Institute of ceramic high-performance materials of the Technical University Hamburg-Harburg (TUHH) in the framework of SFB 986 [122]. This three dimensional system is composed by monodisperse ($ZrO_2$) spheres arranged in a completely disordered way.
This photonic glass provides almost total reflectivity in the infrared spectrum. It is considered to be used as thermal barrier coating to extend the functional lifetime of engineering materials, as e.g. turbine wheels.

The material characteristics of this photonic glass are determined by the filling fraction and dispersion of the $ZrO_2$ spheres. To compare the measurement with the theoretically obtained results, as well as to control the production process, the $ZrO_2$ sphere filling fraction has to be characterised. Since it is not known whether a vertical filling density gradient is present or not, a 3D measurement is necessary. The $ZrO_2$ spheres have a diameter of approximately 2 $\mu$m and are therefore ideally suited to be resolved by SRnCT. This was done in cooperation with M. Ogurreck [104] and is described in the following.

## 9.2 Specimen preparation by FIB

The $ZrO_2$ photonic glass was delivered on a glass substrate. The loosely arranged $ZrO_2$ spheres were initially fixed by a very low viscous superglue to guarantee a mechanical firm and stable order of the spheres during FIB sample preparation. The superglue was additionally thinned by solvant for conductive silver or silverglue, to ensure that the cavities between the small spheres were not sealed.

The sample preparation for SRnCT was exactly performed according the introduced FIB specimen processing method in subsection 3.3.2. Merely the optional preparing cut off from the back side was omitted, because of the already sufficient depth by circular excavation to perform only the final cut off.
The surface of the photonic glass made of $ZrO_2$ spheres is shown in Figure 9.1 part (a), during the excavation of the specimen pillar. In Figure 9.1 part (b) the specimen pillar is safely attached to the IBL sample holder. Figure parts (c) and (d) show the two attaching lines which are almost perpendicularly aligned to each other, and thus provide a stable fixation during the SRnCT measurement.
The sample was safely transported to the IBL at DESY in the transport box described in subsection 3.3.3.


**(a)** Excavation from the photonic glass (20 kV $U_{EHT}$, 5 mm WD, SE2-detector)

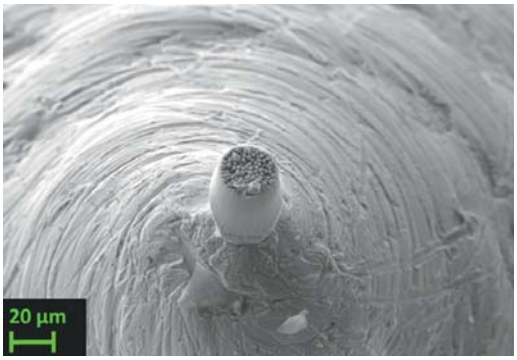


**(b)** On the IBL sample holder (20 kV $U_{EHT}$, 4.9 mm WD, SE2-detector)

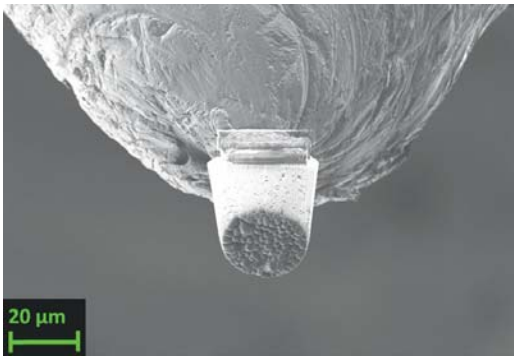


**(c)** First attaching line (FIB image (30 kV, 50 pA), 4.9 mm WD, SE2-detector)

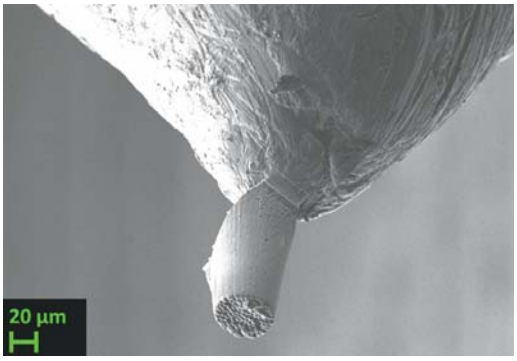


**(d)** Second attaching line (FIB image (30 kV, 50 pA), 4.9 mm WD, SE2-detector)

**Figure 9.1:** FIB sample pillar processed from *Zr* oxide spheres. Due to the general upside down scanning direction of the FIB, the pillar appears head-down in the FIB image.

## 9.3 SRnCT experiment at IBL

The specimen pillar was imaged by the nanotomography X-ray microscopy setup[1] at IBL by using an energy of 17.4 keV, while the working distance of the imaging lens was 100 mm.
Figure 9.2 part (a) shows a projection image of the sample, i.e. the X-ray image before the reconstruction by using a filtered backprojection algorithm. Contrast problems in the optics reduce the achievable resolution and density contrast [104]. In Figure part (b) the reconstructed vertical cross section of the $ZrO_2$ pillar is presented. The glass substrate wedge is nicely visible at the bottom of the pillar. It becomes visible that the platinum deposition is distributed over the whole area of the wedge profile in the lower right part of the pillar (compare the attaching line in Figure 9.1 part (c)), due to the angular limitations during FIB sample preparation. The approximately 2 $\mu$m sized $ZrO_2$ spheres are clearly resolved in this view. To enable a closer look, a reconstructed projection slice is given in Figure 9.3 part (a), and a magnified image of this in Figure part (b).

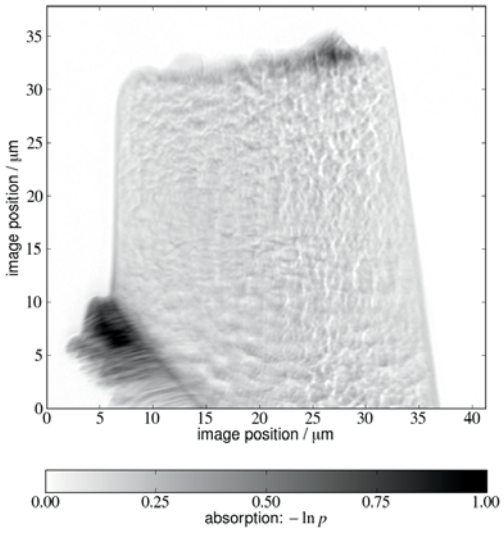


**(a)** Projection image of the $ZrO_2$ pillar.

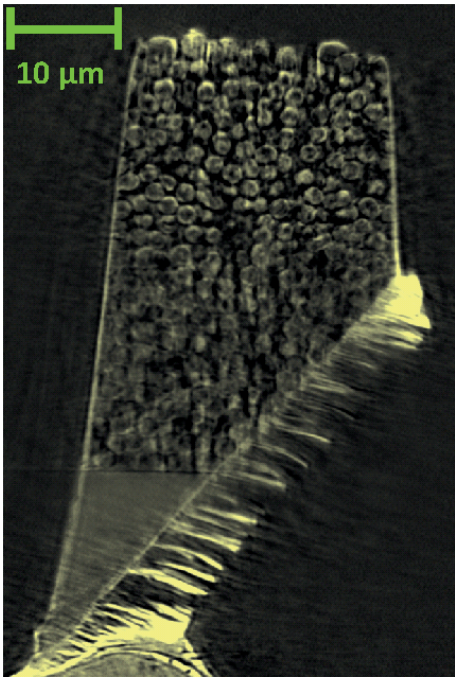


**(b)** Vertical cross section of the reconstructed tomographic image.

**Figure 9.2:** SRnCT images of a pillar composed of $ZrO_2$ spheres of approximately 2 $\mu$m diameter, obtained at IBL.

The SRnCT could possibly detect an inhomogeneous composition of single spheres,

[1] Introduced in section 2.4.4.

highlighted by the varying attenuation coefficient inside. However, artefacts caused by phase interference contribute to this appearance, which is a common problem for propagating coherent X-rays.
By comparison with a highly resolved FIB slice of the pillar in Figure 9.4 part (b), which was taken from the subsequently performed FIB tomography, it is clear that the small inner cavities of about 50 nm of the $ZrO_2$ spheres could not be resolved. It is assumed to be rather a local average of solid $ZrO_2$ matter and smaller or bigger cavities which results in this attenuation variation in Figure 9.3 part (a) & (b).
By this FIB tomography of the pillar, also bigger cavities in the $ZrO_2$ spheres were detected (Figure 9.4 part (a)). However, they occur comparably seldom and are therefore not suited to discuss the resolution. None of them could be doubtlessly identified on the SRnCT slices.

No reference objects on a suitable scale are present to distinguish doubtlessly which size can be still resolved or not. Therefore an indirect attempt is discussed in the following passage.
By comparison of Figure 9.4 part (b) by SRnCT and Figure 9.3 part (b) by SEM it can be assumed that the contact points between the spheres in the latter Figure are effected by optical blurring, since the protruding contact points are imaged only by SRnCT but are supposed to be usual spherical contact points or are not contacted as detected with SEM. Below a distance threshold of roughly 200 nm between the spheres they appear as contacted by SRnCT, while above this threshold the distance appears abruptly bigger. By SRnCT also the transverse diameter of the blurred contact points between the spheres is again about 200 nm or little less. One can assume that the interstice and the blurred contact points between adjacent particles are roughly determining the obtained SRnCT 3D resolution to be 200 nm.

Regarding the initial scientific question a homogeneous packing fraction could be determined throughout the sample depth by determining the packing fraction at different height steps. The obtained packing fraction $\eta = 0.542 \pm 0.008$ is consistent with the expected packing fraction for a force free sedimentation of spherical particles. It is obviously smaller than a random close packing with $\eta_{rcp} = 0.64$ [104].

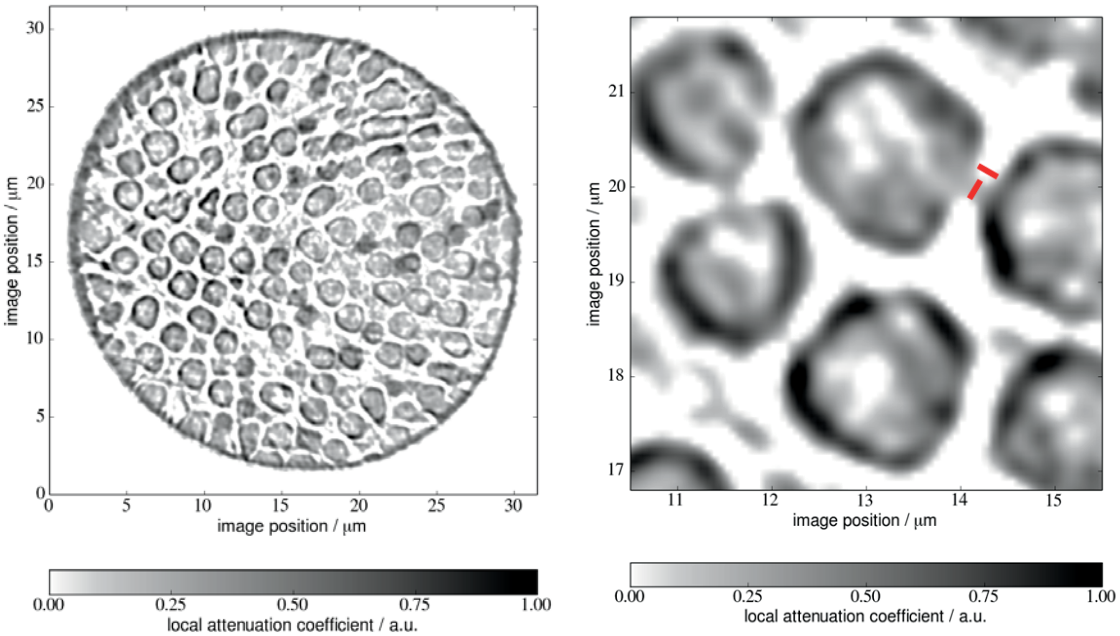


**(a)** Reconstructed projection slice of $ZrO_2$ pillar

**(b)** Zoom on (a), with two 200 nm scale bars in red

**Figure 9.3:** SRnCT slice, obtained on pillar of $ZrO_2$ spheres.

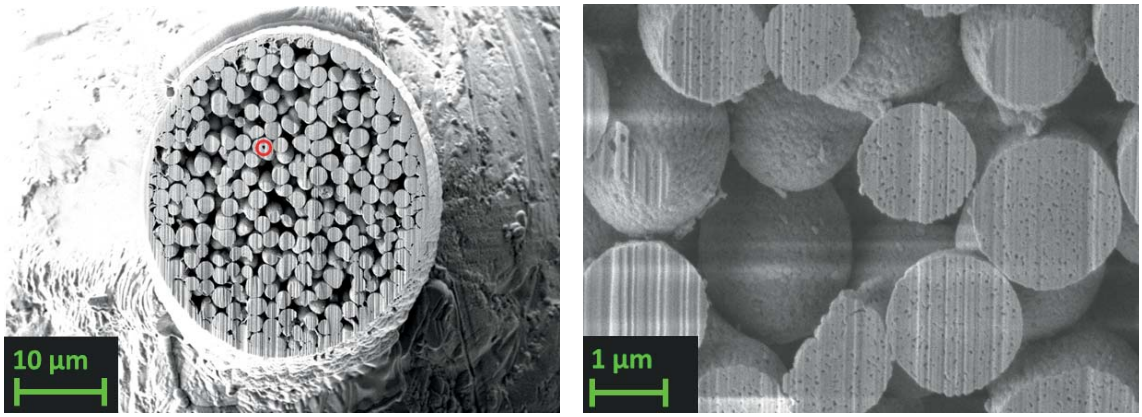


**(a)** FIB slice on $ZrO_2$ pillar with red encircled bigger cavity

**(b)** Inner cavities of the $ZrO_2$ spheres of about 50 nm

**Figure 9.4:** FIB slice of photonic glass made of $ZrO_2$ spheres.

## 9.4 FIB tomography on the photonic glass pillar

Subsequently to SRnCT at IBL the $ZrO_2$ pillar was milled by FIB for a serial sectioning or FIB tomography. Usually a FIB tomography is only performed in perpendicular alignment of the sample surface to the FIB (i.e. 54°), but for such a pillar this would cause dramatically increased curtaining and defocussing in the bottom part by the much longer cross section. Therefore this specimen pillar was tilted by the stage to the minimum value of -8°, in order to align the top surface of the pillar nearly parallel to the FIB slicing plane, which is at -36° regarding the stage position (Figure 9.5).

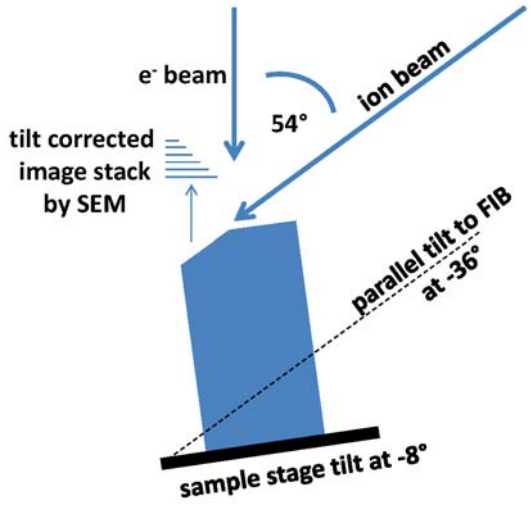


**Figure 9.5:** Pillar alignment of FIB tomography on the pillar of $ZrO_2$ spheres. The features on the cross section are projected on a tilt corrected (stretched) image slice by SEM.

The benefit of this slicing geometry is that the obtained slice images are less affected by curtaining.
The tilt correction is stretching a projected 2D surface to its calculated original length, and had to be set to 36° due to the general arrangement of the FIB with respect to the SEM column.

Between the stage tilt and the FIB slicing plane angle a difference of 28° results, predefined by the column alignment and the maximum range of the stage tilt of the Auriga. Therefore the stacking of the tilt corrected slices (Figure 9.5) leads to a distortion of the pillar in its 3D image (Figure 9.6). By this also the internal structures are distorted, and the round spheres appear elongated (Figure 9.7 part (b)). This could have only been avoided if the top surface of the pillar could have been arranged parallel to the FIB slicing plane, which is however restricted by the present tilt axis.

The SEM images were taken automatically by the so-called cut & slice feature of the Smart SEM software at 2 kV $U_{EHT}$ and obligatory 5 mm WD, using the SE2-detector with a resolution of 2048 × 1536 pixel at scan speed 8. Out of the used magnification a pixel size of 31 nm results. As the working distance is

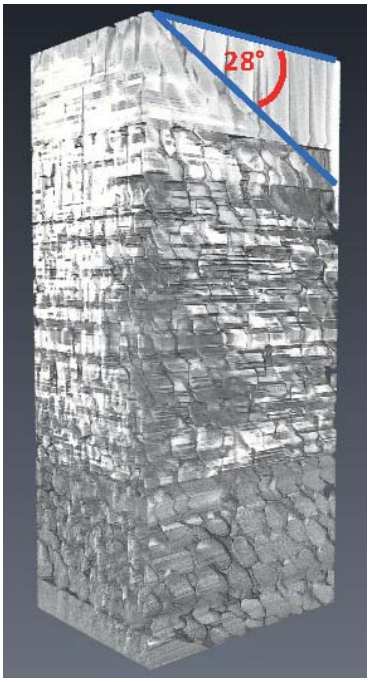


**Figure 9.6:** Cropped pillar from FIB tomography on $ZrO_2$ spheres. The surface of the pillar is distorted by an angle of 28°, caused by geometrical restrictions of the Auriga sample stage (see text). The contrast in the upper part is too strong to distinguish sphere surfaces and thus to obtain a homogenous tomography image.

not repositioned automatically during FIB slicing, the comparably small 30 $\mu$m aperture was used, providing an adequate focal depth. The FIB slicing current was set to 500 pA with a slicing thickness of 25 nm. Altogether 1823 slices were obtained by the serial sectioning on the $ZrO_2$ pillar.

For this FIB tomography the entire pillar and thus some necessary surroundings of it were imaged to allow a characterisation of the pillar as a whole and to make it comparable to the SRnCT data. However, as is typical by this technique a 3D image block is generated out of the obtained 2D features around the specimen pillar by stacking the slices. Therefore a cropped pillar is shown in Figure 9.6.
Initially the serial sectioning procedure was performed with increased contrast, since it was initially considered to binarise the data set subsequently by the present tomography software. Unfortunately the contrast increased during the experiment and produced the very bright lines in the tomographic image. Hence, it had to be readjusted, resulting in the contrast and brightness boundary in the lower part of Figure 9.6.
The usage of the automatic contrast and brightness feature on the whole pillar led to bad contrast and brightness adaption due to the additionally accounted surroundings of the pillar, and could not be applied.
The tomographic image was constructed by using the Avizo software from the *visualisation sciences group (VSG)* (Mérignac Cedex, France).

A general problem for FIB tomography is the curtaining effect. By the deflection of the ion beam, induced by heterogeneous internal or surface structures and also the normal defocussing behind the focal length, the material becomes laterally sputtered with varying intensity. This occurs especially at the edges of the cavernous substructures, which are deflecting the ion beam different. This generates

**(a)** Cropped SRnCT image

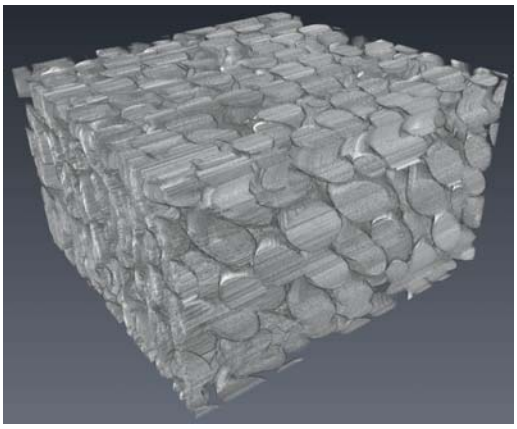

**(b)** Cropped FIB tomography image

**Figure 9.7:** Comparison between SRnCT and FIB tomography images. (a): By line structures in slicing direction FIB curtaining is apparent. The elongated particle shape on the front face is caused by the pillar tilt and the automatic slice alignment, as also by topographical SEM imaging effects on 2D images (see text). (b): the more reliable SRnCT provides less resolution.

a variation of trenches on the ideally obtained lateral 2D image slices (Figure 9.7 part (b)).

Another obstacle for FIB tomography is the 2D imaging of cavernous samples by a FIB produced slice. SEM images are taken on the lateral cutting face and not in projection, as done by X-rays. If the bottom of a cavern structure generates any signal to the SEM detector, this signal will be found on the respective image slice. The image content of a slice therefore includes signals from the material inside the cavern structures although this material was not contained in the lateral FIB cutting face. Therefor a segmentation had to be applied to the SEM images to obtain a clear 3D image. A well segmentation depends strongly on the contrast and brightness of every single sphere, and includes therefor an uncertainty in distinguishing pore and solid.

The obtained 3D pillar of $ZrO_2$ spheres was additionally distorted by randomly occurring sample stage drift in mainly vertical direction. This can be easily seen in the uppermost part of the 3D image in Figure 9.7 part (b) by the layer of vertically stretched spheres. This highlights no limit but a defect of the Auriga stage and has to be repaired.

As expected, a positive result of this FIB tomography is the high resolution by most of the 1823 slices, resolving the small cavities imaged in Figure 9.4 part (b). Compared to the FIB tomography which was previously performed with the

Auriga as a proof of principle on a glioblastoma cell (Appendix C), the higher contrast which could be successfully applied in that case suppressed a signal contribution by internal cavities that would distorted the 2D SEM image slices. Also sample stage drift was not detected for this FIB tomography.

## 9.5 Summary

Finally, after pillars from various materials could be successfully prepared by the FIB specimen processing method as a proof of principle, a pillar made of $ZrO_2$ spheres was successfully characterised for the first time by SRnCT at IBL. The interstice and the blurred contact points between the adjacent particles allow a rough estimate of the obtained SRnCT 3D resolution to be below 200 nm. Phase interference artefacts contribute to the projection, which is a common problem for propagating coherent X-rays. Progress in X-ray phase imaging will allow to handle these effects better in the future.

The subsequently performed FIB tomography was partially hampered by contrast problems and drift, while the angle of 28° between the maximum stage tilt and the FIB slicing plane leads to a distortion of the pillar in its 3D image. Due to this the round spheres appear elongated.
Wargo *et al.* compared nanotomography by X-rays and by FIB in a study on porous fuel cell materials using the nano-CT system UltraXRM-L200 (from *Xradia Inc.*, Pleasanton, California USA) and the FIB-SEM device FEI Strata$^{TM}$ DB 235. The problems which occurred by using the FIB/SEM method are similar, in particular the "erroneous segmentation due to SEM edge effects and uncertainty in distinguishing pore vs. solid, since the internal topography of the pore network is visible" [135]. However, the main disadvantage of FIB tomography is the destruction of the specimen.
Although a high resolution of several nm is obtained by FIB tomography, it is less reliable to arbitrary sample geometries than SRnCT. The construction of a further Auriga sample holder adapter for IBL holders is proposed to achieve the parallel alignment of the pillar top surface to the FIB slicing plane.

With respect to the scientific question which was the starting point of this study it was found that the $ZrO_2$ spheres are packed homogeneously by the packing fraction for a force free sedimentation of spherical particles with the packing fraction $\eta = 0.542 \pm 0.008$ [104]. Some of the spheres are solid but most of them contain homogeneously distributed cavities of about 50 nm diameter. Very seldom spheres with a big central cavity could be found.

# Chapter 10

# Summary and conclusions

The specimen processing method for region of interest SRnCT and nanodiffraction was achieved by selective FIB milling and the utilisation of a micromanipulator to take the excavated specimen from the bulk material and mount it by FIB/GIS attaching on a sample holder. The procedure was performed many times on various materials and complemented by the application of SEM techniques. To enable the adaption of the IBL sample holders the Auriga stage holder was improved by several modifications, without any resulting restrictions to the functionality of the entire cross beam device and its components.
After establishing this novel method several kinds of sample applications proposed for SRnCT were characterised by the cross beam workstation Auriga and X-ray techniques.

The 3D characterisation of a sintered *Ti*-6*Al*-4*V* material by a laboratory-CT device provided detailed knowledge on the porous network structure inside, and featured the pore size distribution by granulometry calculation. Regarding *in vivo* studies the detected 30% porosity of the material provides ideal conditions for tissue ingrowth. This study was jointly published by A. Deing *et al.* [25].
SEM imaging of the cell colonisation could successfully confirm the ingrowth of cells into the porous network. The applied phospholipid coating could be proved by SEM imaging and EDX on the edges of intended broken sample plates.
To enhance the attenuation of the colonised cell tissue for SRnCT staining by *Eu* and the incorporation of iron nanoparticles was applied and verified by EDX. The cell uptake was furthermore proved inside of two single cells by combined FIB/SEM techniques. Finally the cells were not visible in the *Ti*-6*Al*-4*V* matrix by performing SR$\mu$CT. The staining was insufficient and therefore the implementation of the tomographic phase contrast method is necessary at IBL, to provide suitable contrast for this kind of samples.

Selected applications of combined FIB/SEM techniques regarding the corrosion of *Mg* alloys developed as implant materials for medical purposes were presented. The SEM images showed that the different immersion solutions as well as the varied presence of proteins led to a unique crystalline growth on each sample.

The EDX mapping proved the co-localisation of the elements *Ca* and *P* as well as *C* and *O*. The results were jointly published by F. Feyerabend *et al.* [34].
In the framework of this thesis the Auriga was used frequently to prepare cross sections of different materials by FIB in order to analyse the inner structure and the elementary composition below the surface, as presented for the cooperatively published study of a $Mg - 10Dy$ alloy by L. Yang *et al.* [144]. It was found that the corrosion layer is enriched by *Dy*, which likely exists as a mixture of $Dy_2O_3$ and $Dy(OH)_3$. The content of *Ca* and *P* decreases gradually from the surface to the bottom of the corrosion layer. By using SEM the osteoblast morphology could be observed on all cultured samples and no cytotoxicity could be found.
The FIB/SEM cross sectioning method was furthermore applied to confirm a homogeneous dispersion of $MgH_2$ and $LiBH_4$ inside the carbon aerogel scaffold of a hydrogen storage system, which is highly suited to investigate the pore structure by SRnCT phase contrast in future experiments. Out of this cooperation five studies [47; 48; 46; 44; 45] were jointly published by R. Gosalawit-Utke *et al.*.
The phase composition of a spherical gas-atomised *Ti*-45*Al*- 5 and 10*Nb* powder alloy which was produced by the plasma melting induction guided gas atomisation (PIGA) technique at HZG was determined by X-ray scattering at the HEMS side station (beamline P07b) at PETRA III, as well as by 2D and FIB based 3D EBSD measurements. By SEM investigations it was found that the dendritic structures of bigger particles of *Ti*-45*Al*-10*Nb* are more pronounced than for the 5*Nb* fraction, while smaller particles contain in average less *Nb*. Due to the presence of dendritic structures the cooling rate during powder atomisation was still to low to reach the critical growth rate for absolute stability and thus a planar solidification.
Since the $\beta$-phase is primarily formed during solidification, the BSE detected cauliflower structure gave proof that diffusion took place during solidification of the initial $\beta$-grain formation, even though there is no relation between the grains and the dendrite structure. By the absence of preferred misorientation angles one finds that $\alpha$-grains are not formed out of already solidified $\beta$-grains according the Burgers relationship by a solid state phase transformation.
Regarding the occurring, still extremely fast cooling rates, the hexagonal-close-packed $\alpha$-phase is possibly originated by a martensitic phase transition from the body-centred-cubic $\beta$-phase.
Regarding SRnCT the *Ti*-45*Al*-10*Nb* specimen could successfully be prepared by the described FIB specimen processing method, but preliminary SR$\mu$CT experiments at IBL revealed too weak material contrast of the inner dendritic structures. Therefore the phase contrast technique is proposed for this material as soon as available at IBL.
To enable also a FIB tomography by using BSE contrast the BSE-detector of the Auriga should be slightly modified, if feasible, by a little cutout of the detector frame scaffold to allow the *in situ* usage with the FIB. Otherwise a commonly available pneumatic BSE-detector from *Zeiss* would be needed, providing an automated detector insertion, to enable this.
Scanning nanodiffraction at the MiNaXS endstation at PETRA III was enabled by

the developed specimen processing method. The FIB based sample preparation principle was successfully used in a slightly modified way to process required specimen geometries out of different sample types for nanodiffraction experiments, as for the presented wood lamellae which was investigated at the MiNaXS beamline (P03) at PETRA III at DESY. The perpendicular orientation of the tracheids in the wood lamellae was precisely achieved by this preparation method. The FIB milling enabled a very defined cross sectioning and surface preparation of the prepared specimen. The obtained diffraction images proved a strong *Ga* incorporation due to the FIB specimen processing, which hindered the acquisition of diffraction patterns from the S3 cell wall layer and partially from the S2 layer. Despite the damage in the S3 and partially the S2 cell wall layer the remaining cell wall seems to be intact and this method can still be used nicely to investigate the S1 and main parts of the S2 layer. The jointly published paper by S. Storm *et al.* [128] reports for the first time on the investigation of a FIB-processed biological sample by scanning X-ray nanodiffraction.

Several specimen pillars out of different materials were successfully processed by FIB for proposed SRnCT experiments and this method showed a high material versatility. Finally a FIB processed specimen pillar from a photonic glass sample composed of $ZrO_2$ spheres was investigated for the first time by SRnCT at IBL by M. Ogurreck [104] regarding its 3D-package homogeneity. The interstice and the blurred contact points between adjacent particles allow the rough determination of the obtained SRnCT resolution to be approximately 200 nm.
Regarding the scientific question of the investigated material it was found that the $ZrO_2$ spheres are packed homogeneously by the packing fraction for a force free sedimentation of spherical particles with the packing fraction $\eta = 0.542 \pm 0.008$ [104]. Some of the spheres are solid but most of them contain homogeneously distributed cavities of about 50 nm diameter. Very seldom spheres with a big central cavity could be found.
Subsequently a FIB tomography was performed on the $ZrO_2$ specimen pillar. This particular experiment was hindered by contrast and drift problems. The main disadvantage of FIB tomography is that it is a destructive method. Although a high resolution of several nm is obtained by FIB tomography, it is less reliable to arbitrary porosities than SRnCT.
For both tomography methods further improvement is needed: For SRnCT the resolution has to be improved by refinement of X-ray optics and by reducing the phase artefacts to enhance the resolution to below 100 nm while for the FIB tomography an additional adapter must be constructed for a proper sample alignment of pillar shaped SRnCT samples.

The SRnCT method offers reliable 3D imaging for materials which fit to the applicable X-ray energy range of the experiment whereas a complex sample preparation is necessary. The FIB tomography method provides a destructive 3D imaging which can also be applied without time consuming sample preparation, but the imaging by serial sectioning is more prone to erroneous data. In addition sputtering of a conductive coating could be necessary for non-conductive samples.

SRnCT requires X-ray contrast of the internal structures and FIB tomography demands materials providing contrast to the applicable SEM detectors.

Regarding the combination of FIB/SEM methods with the synchrotron utilisation as well as the material versatility the present work is one of the first in this field. Only few different publications with a similar intention were found. In the study of Wargo *et al.* [135] the differences of FIB tomography and X-ray nanotomography using a laboratory CT device are exemplified on a fuel cell material. Lombardo *et al.* [86] on the other hand investigated the feasibility of different specimen shapes by the FIB sample preparation for SRnCT at the *Advanced Photon Source* at the Argonne National Laboratory (Illinois, USA), without mentioning the achieved resolution of the final measurement. Again exclusively one fuel cell material is investigated. In both studies the discussion of the attachment requirements for different specimens and materials in varying shapes, especially for bigger ones, as well as the discussion of the specimen transport is missing. Beside of this, the described procedures are in general similar to those ones presented here.

Finally, the presented method of specimen processing that fits the criteria for X-ray nanotomography and nanodiffraction by selectively FIB-milling around a region of interest and the utilisation of a micromanipulator for taking the excavated sample from the bulk material and mounting it on a sample holder is of increasing importance for the ongoing development of nano X-ray techniques in common. Samples with multiple $\mu$m scaled shapes and sizes are demanded by synchrotron and laboratory X-ray experiments as well. The characterisation and sample preparation for synchrotron experiments presented in this work provides significant advances in a wide field of applications ranging from engineering materials science to soft tissue research.

# Appendix A

# Introduction to phase contrast imaging

The complex refractive index of a medium is given by Equation 2.22:

$$n = 1 - \delta + i\beta, \tag{A.1}$$

with the imaginary part $\beta$ linked to the absorption, or attenuation respectively, and the real part $\delta$ linked to the phase shift. Apart from the absorption, $1 - \delta$ together with the travel distance d of an electromagnetic wave, travelling through a medium, and its wavelength $\lambda$ determines the phase shift by

$$\Delta\Phi = \frac{2\pi\delta d}{\lambda}. \tag{A.2}$$

$\delta$ itself depends on the wavelength $\lambda$ and the density of the sample. Only indirect methods are possible to measure the phase shift, due to the fact that only intensities are accessible on images and the phase information is lost. Therefor interferometric methods are applied to attain this information. A review on the common phase contrast methods is given by Momose *et al.* [95]. Outlining this we can separate the methods in three main divisions, extracted from [56] and [7]:

- **Most direct** phase-contrast projections, measuring the phase shift with respect to the self reference beam (Bonse-Hart interferometer [13]). This technique is based on the principal of splitting a coherent beam by a crystal interferometer in two different paths. One path is used to ray the specimen, while the other stays unaffected or is shifted for a calculated value, to visualise the refractive information extracted by the first path in an interference pattern on the detector plane [94]. The Phase shift $\phi$ is given by

$$\phi \propto \frac{\sigma}{E}, \tag{A.3}$$

with the electron density $\sigma$ and the applied X-ray energy $E$. As only a narrow spectral width of the beam is used by the interferometer, a brilliant synchrotron source is mandatory to yield enough flux.

- **Differential** method, measuring the $1^{st}$ derivative of the phase shift. The specimen illuminated by a parallel monochromatised X-ray beam becomes imaged on a detector by an upstream analyser crystal. The image only contains information on that part of the transmitted and refracted beam that satisfies the Bragg condition of the analyser crystal. Scanning the analyser crystal angulary provides analysis of different refractive indexes as e.g. shown by Chapman *et al.* [21] or Dilmanian *et al.* [26]. Here again a brilliant synchrotron source is mandatory to yield enough flux, caused to the two monochromatising crystals. The monochromator and the analyser crystal can be exchanged by a beam-splitter grating and an analyser grating. This grating-based phase-contrast methods can also be applied on polychromatic sources, as done by Herzen *et al.* [57].

- Indirect phase-contrast projections are **Propagation based** methods, measuring the $2^{nd}$ derivative of the phase shift. By using spatially coherent illumination without any optical components Fresnel resp. Fraunhofer diffraction happens while the beam propagates to the detector after penetrating the specimen. This technique enables holotomography by varying the specimen-detector distance and gaining a complete phase map of the specimen, as Cloetens *et al.* presented [23]. By requiring a spatially coherent beam, this is only feasible at $3^{rd}$ generation synchrotron radiation sources.

# Appendix B

# Tables and procedures for sample preparation including cells

## B.1 Critical point drying

Subsequent to sample preparations with cells, the critical point drying (CPD) procedure using 2-propanol[1] and $CO_2$ with the Leica EM CPD030 from *Leica Mikrosysteme* (Wetzlar, Germany) device enables SEM and similar investigations without damaging the cell structure by drying. The CPD procedure dries without passing the phase boundary from fluid to gas, see Figure B.1.

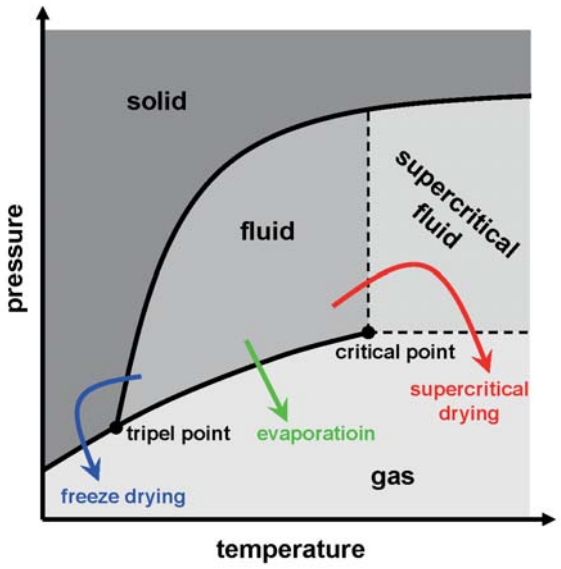


**Figure B.1:** The sample becomes dry by moving its state around the so called critical point, avoiding the phase transition. The critical point of $CO_2$ is at 73,9 bar 31.1 °C

[1] i.e. isopropanol

## The critical point drying procedure:[2]

### Fixation, staining and dehydration

1 Take samples out of culture, wash with PBS[3]
2 Immerse samples in 2.5 % glutaraldehyde solution in well plates, one sample per well for at least 2 hours - normally over night
3 Transfer sample to new well plate with 1 % osmium tetroxide, stain for 30 min.
4 Transfer sample to new well plate with 20 % 2-propanol, immerse for 1-2 hours
5 Transfer sample to new well plate with 40 % 2-propanol, immerse for 1-2 hours
6 Transfer sample to new well plate with 60 % 2-propanol, immerse for 1-2 hours
7 Transfer sample to new well plate with 80 % 2-propanol, immerse for 1-2 hours
8 Transfer sample to new well plate with 100 % 2-propanol, immerse for 1-2 hours
9 Store samples in 100 % 2-propanol by covering the plate with adhesive foil, storage of up to one week is possible. Make sure that the solvent is always covering the sample

### Critical point drying (CDP)

10 Put a proper critical point drying sample holder basket in beaker with 2-propanol, so the sample holder is fully covered.
11 Transfer samples from the well plate the sample holder basket.
12 Open the lid of the CDP sample chamber.
13 Make sure that the magnetic stir bar is in the sample chamber.
14 Fill it with 2-propanol to half level.
15 Transfer sample holder into sample chamber. Make sure that the cavity of the sample holder fits to the gas inlet tube.
16 Fill the chamber with 2-propanol up to the upper part of the viewing window.
17 Close the lid of the sample chamber tightly.
18 Make sure that the Metering valve is closed.
19 Press Buttons "Cooling" & "Stirrer".
20 Wait until the temperature has reached 4°C & open the valve of the CO2-bottle.

[2]applied in common for all samples with cells mentioned in this thesis
[3]phosphate buffered saline

21 Press Button "Medium out" until the fluid level is slightly beyond the top of the sample holder, then press button "Medium out" again to stop medium outlet.
22 Press button "Medium in" to fill the chamber with CO2, observe the mixture of solvent and CO2 (schlieren), press button "Medium in" again when the upper part of the viewing window is reached.
23 Repeat step 21 and 22 until no schlieren are visible anymore (at least 6 times).
24 During step 21 control that the outlet tube is not frozen.
25 After no schlieren are visible anymore, fill the sample chamber with CO2 to ¾ of the visible area, and close the valve of the CO2-bottle.
26 Press Button "Cooling" to stop the cooling process.
27 Press Button "Heating" to start the heating process. Heating should be performed up to 40°C - the sublimation point of CO2 is at 31°C at 75.5 Bar (observe the pressure meter!)
28 When 40°C are reached, press button "Stirrer" to stop stirring the medium
29 Press button "Gas out" and adjust the gas flow rate with the "Gas Metering valve", Flow rate should be adjusted to the scale of 1.5 (Maximum!) in the flow meter on top of the instrument
30 The degassing process may take up to 1.5 hours, if not observed. If the flow rate is kept constant, it takes about 30 minutes. The process is finished, when the pressure meter reaches "0" and the "Gas Metering valve" is fully open.
31 Press Button "Heating" to stop the heating process.
32 Open the lid of the sample chamber & Remove the sample holder from the CDP.
33 Remove samples from sample holders and mount it to SEM sample holders with carbon contact foils or use silver glue.
34 CPD samples can be stored for at least half a year in an appropriate environment (no humidity/desiccator or argon atmosphere) without quality loss.

## B.2 Phospholipid coating

**Phospholipid coating for samples with POPE:**

- Solve phospholipids POPE in a chloroform:methanol (80:20) solution to a final concentration of 1 mM[4], e.g.:
  - 40 ml chloroform
  - 10 ml methanol
  - 35.8998 mg POPE
- Put 50 $\mu$l of this solution on the top of the sample discs
- Let evaporate and dry for 30 min at room temperature
- Incubate for 2 h in cell culture medium

**Au-labeled headgroups, Au-DPPE**

- 0.1 to 1% Nanogold-DPPE (Au-DPPE) with an unlabeled lipid is usually appropriate to prepare labeled liposome, e.g.:

➤ For a 0.1% Nanogold-DPPE in 1mM POPE: 2$\mu$l Au-DPPE in 1980 $\mu$l POPE

➤ For a 1% Nanogold-DPPE in 1mM POPE: 2$\mu$l Au-DPPE in 198 $\mu$l POPE

## B.3 Sample preparation with different stainings for tomography

### Cell staining for tomography with europium

Goal: prepare porous titanium samples with different amount of cells (Saos-2; 50,000 and 100,000 cells) with different concentrations of europium (0 $\mu$M (control), 1 $\mu$M, 20 $\mu$M, and 50 $\mu$M).

- use *203254 Aldrich* Europium (III) chloride hexahydrate- 99.99% trace metals basis
  - ➤ Formula: $C_l3Eu \cdot 6H_2O$
  - ➤ Molecular weight: 366.41 g/mol
- Prepare a 1 mM stock-solution: Dissolve 3.66 mg in 10 ml dd$H_2O$. Filtrate with a 0.2 $\mu$m filter
- In 25 cm$^2$ cell culture flasks:
  - ➤ Seed 0.5 million Saos-2 cells in four flasks labelled "control", "1 $\mu$M", "20 *mu*M" and "50 $\mu$M" (n. b.: during the procedure, the media is always complemented with 10% FBS[5]).
- Cultivate them either with:

[4] mM = milli molar

[5] i.e. fetal bovine serum

➤ 12 mL media (flask labelled control)
➤ 12 mL media + 12 $\mu$l europium solution (flask labelled 1 $\mu$M)
➤ 12 mL media + 240 $\mu$l europium solution (flask labelled 20 $\mu$M)
➤ 12 mL media + 600 $\mu$l europium solution (flask labelled 50 $\mu$M)

•Incubate for two days

•After these two days, prepare from each flask (i.e., 16 samples in total):
➤ 2 porous-titanium plates with 50,000 cells (duplicate)
➤ 2 porous-titanium plates with 100,000 cells (duplicate)

•Coat wells with 1% agarose; when the agar gets hard, place the titanium plates on.
•Prepare a 1 million cells/ml solution (media without europium).
•Deposit one drop of cell + media (50 $\mu$l: 50,000 cells or 100$\mu$l: 100,000 cells) on the top of the Ti-plate.
•Let the cells adhere for 45 min under the bench before complementing the well with the appropriate volume of media.

•Let the cells grow for two days and prepare them for SEM pre-characterisation and subsequent tomography with the critical point dryer technique.

## Cell staining for tomography with Fe-nanoparticles

Goal: prepare porous titanium samples with different amount of cells (Saos-2; 50,000 and 100,000 cells) with different concentrations of nanoparticles (NP-MA; 0.25 $\mu$l/ml and 0.5 $\mu$l/ml).

•In 25 $cm^2$ cell culture flasks: ➤ Seed 0.5 million Saos-2 cells in two flasks labelled "0.25" and "0.5" (n. b.: during the procedure the media is always complemented with 10% FBS).
•Cultivate them either with:
➤ 12 ml media + 3 $\mu$l NP-MA-Birte's solution (flask labelled 0.25)
➤ 12 mL media + 6 $\mu$l NP-MA-Birte's solution (flask labelled 0.5)

•Incubate for two days

•After these two days, prepare from each flask (i.e., 8 samples in total):
➤ 2 porous-titanium plates with 50,000 cells (duplicate)
➤ 2 porous-titanium plates with 100,000 cells (duplicate)

•Coat wells with 1% agarose; when the agar gets hard, place the titanium plates on.
•Prepare a 1 million cells/ml solution.
•Deposit one drop of cell + media (50 $\mu$l: 50,000 cells or 100$\mu$l: 100,000 cells) on the top of the Ti-plate.

•Let the cells adhere for 45 min under the bench before complementing the well with the appropriate volume of media.

•Let the cells grow for two days and prepare them for SEM pre-characterisation and subsequent tomography with the critical point dryer technique.

### B.3.1 Attenuation enhancing staining sample row with and without POPE coating

**Table B.6:** Sample row for SEM investigations with and without POPE and Saos-2 cells, treated with europium (Eu) or myristic-acid covered Fe-nanoparticles (NP) respectively.

| label | POPE | Cell amount | Incorporated material | Inc. mat. concentration | comments |
|---|---|---|---|---|---|
| #1 | no | 50000 | - | 0 | shortly mounted on the wrong side |
| #2 | no | 100000 | - | 0 | strange surface contamination |
| #3 | no | 50000 | Eu | 1 $\mu$M[6] | hardly cells |
| #4 | no | 50000 | Eu | 1 $\mu$M | |
| #5 | no | 100000 | Eu | 1 $\mu$M | |
| #6 | no | 100000 | Eu | 1 $\mu$M | |
| #7 | no | 50000 | Eu | 20 $\mu$M | investigation of backside too; broken for insight, cells everywhere |
| #8 | no | 50000 | Eu | 20 $\mu$M | hardly cells; strange surface contamination |
| #9 | no | 100000 | Eu | 20 $\mu$M | |
| #10 | no | 100000 | Eu | 20 $\mu$M | |
| #11 | no | 50000 | Eu | 50 $\mu$M | |
| #12 | no | 50000 | Eu | 50 $\mu$M | |
| #13 | no | 100000 | Eu | 50 $\mu$M | |
| #14 | no | 100000 | Eu | 50 $\mu$M | EDX; broken for insight, less cells in upper half |
| #15 | no | 50000 | - | 0 | |
| #16 | no | 100000 | - | 0 | |
| #17 | no | 50000 | NP | 0.25 $\mu$l/ml | |

continue next page ...

[6] $\mu$M = micro molar

| label | POPE | Cell amount | Incorporated material | Inc. mat. concentration | special comments |
|---|---|---|---|---|---|
| #18 | no | 50000 | NP | 0.25 $\mu$l/ml | |
| #19 | no | 100000 | NP | 0.25 $\mu$l/ml | |
| #20 | no | 100000 | NP | 0.25 $\mu$l/ml | |
| #21 | no | 50000 | NP | 0.5 $\mu$l/ml | |
| #22 | no | 50000 | NP | 0.5 $\mu$l/ml | |
| #23 | no | 100000 | NP | 0.5 $\mu$l/ml | EDX; FIB cross section on cell |
| #24 | no | 100000 | NP | 0.5 $\mu$l/ml | EDX |
| #25 | yes | 50000 | - | 0 | |
| #26 | yes | 100000 | - | 0 | |
| #27 | yes | 50000 | NP | 0.25 $\mu$l/ml | |
| #28 | yes | 50000 | NP | 0.25 $\mu$l/ml | |
| #29 | yes | 0 | NP | 0.25 $\mu$l/ml | |
| #30 | yes | 0 | NP | 0.25 $\mu$l/ml | |
| #31 | yes | 50000 | NP | 0.5 $\mu$l/ml | |
| #32 | yes | 50000 | NP | 0.5 $\mu$l/ml | EDX; hardly cells on top; broken for insight, POPE like, cracked covering in the upper middle |
| #33 | yes | 0 | NP | 0.5 $\mu$l/ml | |
| #34 | yes | 0 | NP | 0.5 $\mu$l/ml | EDX |
| #35 | yes | 50000 | Eu | 50 $\mu$M | |
| #36 | yes | 50000 | Eu | 50 $\mu$M | |
| #37 | yes | 100000 | Eu | 50 $\mu$M | EDX; hardly cells |
| #38 | yes | 100000 | Eu | 50 $\mu$M | no cells |
| #39 | yes | 50000 | - | 0 $\mu$M | |
| #40 | yes | 100000 | - | 0 $\mu$M | |
| #41 | yes | 50000 | Eu | 1 $\mu$M | |
| #42 | yes | 50000 | Eu | 1 $\mu$M | |
| #43 | yes | 100000 | Eu | 1 $\mu$M | |
| #44 | yes | 100000 | Eu | 1 $\mu$M | |
| #45 | yes | 50000 | Eu | 20 $\mu$M | |
| #46 | yes | 50000 | Eu | 20 $\mu$M | investigated only backside; no cells |
| #47 | yes | 100000 | Eu | 20 $\mu$M | EDX |

continue next page ...

| label | POPE | Cell amount | Incorporated material | Inc. mat. concentration | special comments |
|---|---|---|---|---|---|
| #48 | yes | 100000 | Eu | 20 $\mu$M | EDX; investigation of backside; broken for insight, cells mainly in lower half; POPE like, cracked covering mainly in upper half |

# Appendix C

# FIB tomography on glioblastoma cell

As a proof of principle on FIB tomography, a glioblastoma[1] cell was successively cut in 25 nm steps by a FIB current of 500 pA, while every evolved cross section became imaged by the SE2 detector. The cell was previously cultured in growth medium on a *Ti* substrate for 30 minutes before it got stabilised with $OsO_4$[2], dehydrated by an alcoholic row and supercritical dried[3], in order to maintain the cell natural shape and stability under vacuum conditions.
Previously to FIB slicing a protective *Pt* layer was deposited on the cell by FIB/GIS. The FIB slices were reworked to the tomography image (Figure C.1) by the mentioned Avizo software.

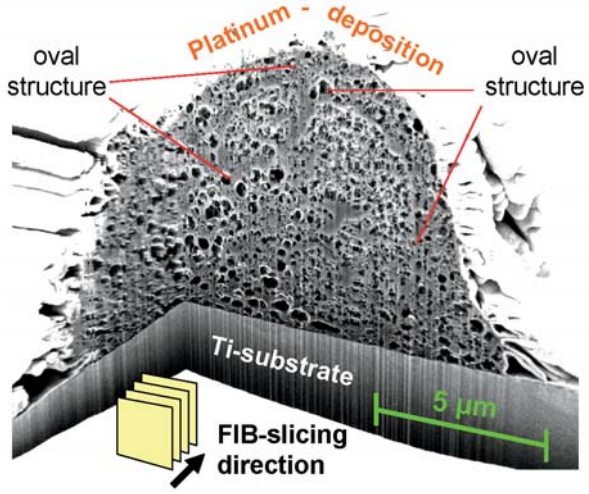


**Figure C.1:** FIB tomography of glioblastoma cell on a *Ti* substrate. SEM imaging was done at 3 kV $U_{EHT}$ and mandatory 5 mm WD (section 3.2) by the SE2-detector.

After few hours adherence cells usually spread out on a proper surface like *Ti*. Here, due to the short time of cell culture, the cell had little time for this and is still present in sphere shape, as it is generally in a solution. In slicing direction on the FIB cutting planes FIB curtaining is visible, caused by the edges of the

[1] Introduced in section 4.2.
[2] osmiumtetroxide
[3] for further information please view section B.1

cavernous substructure which is differentially deflecting the ion beam. The inner structure is too inhomogeneous, and effects additional curtaining besides that one generated by the surface edge. By another attempt it was also tried to perform a FIB tomography on an not coated cell. This revealed that the FIB *melts* the cell successively, ahead to the active slicing plane.
By scrolling through the tomographic slices of this cell different structures become visible. Unfortunately they could not be separated by contrast reworking on the tomographic slices, they are too strong connected by the intracellular network.

# Appendix D

# Powder diffraction data

The exact knowledge of the wavelength is necessary to rework the data, in our case by the fit2D software. To calculate the wavelength $\lambda$ by the applied energy $E = 87$ keV of the diffraction experiment, on has

$$c = \lambda \cdot \nu \qquad \text{and} \qquad E = \frac{h \cdot c}{\lambda}. \tag{D.1}$$

Out of this follows by using $h = 4,135667516 \cdot 10^{-15}$ eV·s and $c = 300000$ km/s

$$\lambda = \frac{h \cdot c}{E} = 0.14260922\text{Å}. \tag{D.2}$$

By this, and the additional diffraction measurement of two standard materials ($Al_2O_3$ and Zn powder), the data was calibrated. The measured two dimensional Debye-Scherrer Rings were integrated, resulting in a one dimensional intensity distribution which could then be analysed for each sample by using the powdercell software, as shown in Figure D.1.

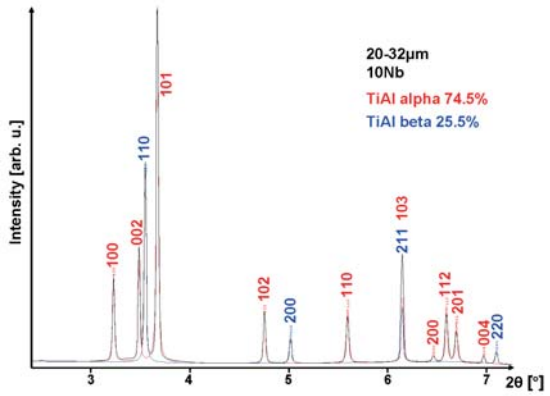


**Figure D.1:** Integrated diffraction pattern of the 20-32$\mu$m fraction of the 10*Nb* alloy, analysed and viewed by powdercell.

**Table D.1:** Powder fractions by diameter and related results gained by the diffraction experiment at HEMS-sidestation. The volume percentage of the respective phases are given in the table by $\alpha$ or $\beta$ respectively, while $a$ and $c$ describe the absolute value of the related basis vector of the unit cell.

| fraction[$\mu m$] | alloy | $\alpha$[%] | $a$[Å] | $c$[Å] | $\beta$[%] | $c$[Å] | exposure time[s] | rotated |
|---|---|---|---|---|---|---|---|---|
| <20 | 10Nb | 36 | 2.9213 | 4.871 | 64 | 3.2587 | 6 | |
| 20-32 | 10Nb | 75.9 | 2.9214 | 4.6906 | 24.1 | 3.2587 | 6 | |
| 32-45 | 10Nb | 91.3 | 2.9213 | 4.6910 | 8.7 | 3.2588 | 6 | |
| 45-63 | 10Nb | 96.2 | 2.9206 | 4.6907 | 3.8 | 3.2599 | 4 | |
| 63-90 | 10Nb | 98.3 | 2.9209 | 4.6919 | 1.7 | 3.2586 | 2 | |
| 90-125 | 10Nb | 98.9 | 2.9213 | 4.6902 | 1.1 | 3.2620 | 2 | |
| 125-180 | 10Nb | 99.4 | 2.9200 | 4.6902 | 0.6 | 3.2600 | 2 | |
| 180-250 | 10Nb | 99.4 | 2.9204 | 4.6912 | 0.6 | 3.2600 | 1 | |
| 250-355 | 10Nb | 99.3 | 2.9190 | 4.6893 | 0.7 | 3.2600 | 0.7 | |
| <20 | 10Nb | 35.6 | 2.9210 | 4.6877 | 64.4 | 3.2582 | 15 | yes |
| 20-32 | 10Nb | 74.5 | 2.9216 | 4.6908 | 25.5 | 3.2583 | 20 | yes |
| 32-45 | 10Nb | 92.1 | 2.9212 | 4.6910 | 7.9 | 3.2595 | 20 | yes |
| 45-63 | 10Nb | 96.9 | 2.9206 | 4.6906 | 3.1 | 3.2599 | 20 | yes |
| 63-90 | 10Nb | 98.3 | 2.9208 | 4.6914 | 1.7 | 3.2599 | 18 | yes |
| 90-125 | 10Nb | 99 | 2.9206 | 4.6914 | 1 | 3.2600 | 15 | yes |
| 125-180 | 10Nb | 99.3 | 2.9203 | 4.6914 | 0.7 | 3.2600 | 15 | yes |
| 180-250 | 10Nb | 99.4 | 2.9199 | 4.6914 | 0.6 | 3.2609 | 10 | yes |
| 250-355 | 10Nb | 99.2 | 2.9195 | 4.6911 | 0.8 | 3.2620 | 8 | yes |
| <20 | 5Nb | 74.5 | 2.9186 | 4.6864 | 25.5 | 3.2575 | 6 | |
| 20-32 | 5Nb | 96.2 | 2.9190 | 4.6880 | 3.8 | 3.2569 | 6 | |
| 32-45 | 5Nb | 98.7 | 2.9189 | 4.6882 | 1.3 | 3.2580 | 6 | |
| 45-63 | 5Nb | 99.2 | 2.9190 | 4.6886 | 0.8 | 3.2570 | 3 | |
| 63-90 | 5Nb | 99.6 | 2.9180 | 4.6874 | 0.4 | 3.2563 | 0.7 | |
| 90-125 | 5Nb | 99.7 | 2.9180 | 4.6885 | 0.3 | 3.2570 | 0.5 | |
| 125-180 | 5Nb | 99.7 | 2.9189 | 4.6875 | 0.3 | 3.2560 | 0.5 | |
| 180-250 | 5Nb | 99.9 | 2.9203 | 4.6879 | 0.1 | 3.2600 | 0.5 | |
| 250-355 | 5Nb | 100 | 2.9168 | 4.6871 | 0 | - | 0.3 | |
| <20 | 5Nb | 74.8 | 2.9185 | 4.6861 | 25.2 | 3.2574 | 20 | yes |
| 20-32 | 5Nb | 96.4 | 2.9189 | 4.6879 | 3.6 | 3.2581 | 20 | yes |
| 32-45 | 5Nb | 98.7 | 2.9189 | 4.6882 | 1.3 | 3.2570 | 20 | yes |
| 45-63 | 5Nb | 99.2 | 2.9185 | 4.6879 | 0.8 | 3.2560 | 20 | yes |
| 63-90 | 5Nb | 99.5 | 2.9182 | 4.6877 | 0.5 | 3.2560 | 18 | yes |
| 90-125 | 5Nb | 99.6 | 2.9184 | 4.6885 | 0.4 | 3.2551 | 15 | yes |
| 125-180 | 5Nb | 99.7 | 2.9183 | 4.6888 | 0.3 | 3.2570 | 15 | yes |
| 180-250 | 5Nb | 99.9 | 2.9179 | 4.6889 | 0.1 | 3.2600 | 5 | yes |
| 250-355 | 5Nb | 100 | 2.9178 | 4.6887 | 0 | - | 5 | yes |

# List of Figures

# Bibliography


[1] J. Als-Nielsen and D. McMorrow, *Elements of modern X-ray physics*, John Wiley & Sons, West Sussex, 2001.

[2] M. V. Avdeev, B. Mucha, K. Lamszus, L. Vekas, V. M. Garamus, A. V. Feoktystov, O. Marinica, R. Turcu, and R. Willumeit, *Structure and in Vitro Biological Testing of Water-Based Ferrofluids Stabilized by Monocarboxylic Acids*, Langmuir, 26 (2010), pp. 8503–8509.

[3] K. Balewski, W. Brefeld, W. Decking, H. Franz, R. Röhlsberger, and E. Weckert, *PETRA III: A Low Emittance Synchrotron Radiation Source*, Technical report, DESY, (2004).

[4] A. Bandyopadhyay, F. Espana, V. K. Balla, S. Bose, Y. Ohgami, and N. M. Davies, *Influence of porosity on mechanical properties and in vivo response of Ti6Al4V implants*, Acta Biomater, 6 (2010), pp. 1640–1648.

[5] E. Baril, L. P. Lefebvre, and S. A. Hacking, *Direct visualization and quantification of bone growth into porous titanium implants using micro computed tomography*, Journal of Materials Science-Materials in Medicine, 22 (2011), pp. 1321–1332.

[6] H. H. Barrett and W. Swindell, *Radiological Imaging; The Theory of Image Formation, Detection, and Processing*, Academic Press Inc., 1981.

[7] F. Beckmann, *Neutrons and Synchrotron Radiation in Engineering Materials Science - Neutron and Synchrotron-Radiation-Based Imaging for Applications in Materials Science - From Macro- to Nanotomography*, Wiley-VCH, 2008.

[8] D. Berger, *Skript zum SEM-Praktikum an der ZELMI der TU Berlin*, Zentraleinrichtung Elektronenmikroskopie, TU Berlin, (2009).

[9] L. Bergmann and C. Schaefer, *Experimentalphysik Band3, Optik*, De Gruyter, 2004.

[10] J. G. Berryman, *Random Close Packing of Hard-Spheres and Disks*, Physical Review A, 27 (1983), pp. 1053–1061.

[11] H. A. Bethe, *Handbuch der Physik, von Geiger und Scheel*, Springer Verlag, 1933.

[12] P. Bleuet, P. Cloetens, P. Gergaud, D. Mariolle, N. Chevalier, R. Tucoulou, J. Susini, and A. Chabli, *A hard x-ray nanoprobe for scanning and projection nanotomography*, Review of Scientific Instruments, 80 (2009).

[13] U. Bonse and M. Hart, *An X-Ray Interferometer*, Applied Physics Letters, 6 (1965), pp. 155–&.

[14] U. Bonse, Q. Johnson, M. Nichols, R. Nusshardt, S. Krasnicki, and J. Kinney, *High-Resolution Tomography with Chemical Specificity*, Nuclear Instruments & Methods in Physics Research Section a-Accelerators Spectrometers Detectors and Associated Equipment, 246 (1986), pp. 644–648.

[15] A. Borbely, P. Cloetens, E. Maire, and G. Requena, *Submicron Tomography Using High Energy Synchrotron Radiation*, Fabrication and Characterization in the Micro-Nano Range: New Trends for Two and Three Dimensional Structures, 10 (2011), pp. 151–170.

[16] U. Bosenberg, S. Doppiu, L. Mosegaard, G. Barkhordarian, N. Eigen, A. Borgschulte, T. R. Jensen, Y. Cerenius, O. Gutfleisch, T. Klassen, M. Dornheim, and R. Bormann, *Hydrogen sorption properties of MgH2-LiBH4 composites*, Acta Materialia, 55 (2007), pp. 3951–3958.

[17] B. D. Boyan, T. W. Hummert, D. D. Dean, and Z. Schwartz, *Role of material surfaces in regulating bone and cartilage cell response*, Biomaterials, 17 (1996), pp. 137–146.

[18] W. Brefeld, K. Balewski, W. Decking, Y. Li, and G. K. Sahoo, *Accelerator physical issues of PETRA III - A new low emittance light source*, Synchrotron Radiation Instrumentation, 705 (2004), pp. 101–104.

[19] W. G. burgers, *On the process of transition of the cubic-body-centered modification into the hexagonal-close-packed modification of zirconium*, Physica, 1 (1934), pp. 561–586.

[20] Y. S. Chang, M. Oka, M. Kobayashi, H. O. Gu, Z. L. Li, T. Nakamura, and Y. Ikada, *Significance of interstitial bone ingrowth under load-bearing conditions: A comparison between solid and porous implant materials*, Biomaterials, 17 (1996), pp. 1141–1148.

[21] D. Chapman, W. Thomlinson, R. E. Johnston, D. Washburn, E. Pisano, N. Gmur, Z. Zhong, R. Menk, F. Arfelli, and D. Sayers, *Diffraction enhanced x-ray imaging*, Physics in Medicine and Biology, 42 (1997), pp. 2015–2025.

[22] H. Clemens and S. Mayer, *Design, Processing, Microstructure, Properties, and Applications of Advanced Intermetallic TiAl Alloys*, Advanced Engineering Materials, 15 (2013), pp. 191–215.

[23] P. Cloetens, W. Ludwig, J. Baruchel, D. Van Dyck, J. Van Landuyt, J. P. Guigay, and M. Schlenker, *Holotomography: Quantitative phase tomography with micrometer resolution using hard synchrotron radiation x rays*, Applied Physics Letters, 75 (1999), pp. 2912–2914.

[24] A. M. Cormack, *My connection with the Radon transform*, 75 Years of Radon Transform, 4 (1994), pp. 32–35.

[25] A. Deing, B. Luthringer, D. Laipple, T. Ebel, and R. Willumeit, *A Porous TiAl6V4 Implant Material for Medical Application*, Int J Biomater, 2014 (2014), p. 904230.

[26] F. A. Dilmanian, Z. Zhong, B. Ren, X. Y. Wu, L. D. Chapman, I. Orion, and W. C. Thomlinson, *Computed tomography of x-ray index of refraction using the diffraction enhanced imaging method*, Physics in Medicine and Biology, 45 (2000), pp. 933–946.

[27] L. Donaldson and P. Xu, *Microfibril orientation across the secondary cell wall of Radiata pine tracheids*, Trees-Structure and Function, 19 (2005), pp. 644–653.

[28] T. Donath, *Quantitative X-ray Microtomography with Synchrotron Radiation*, PhD thesis; Department Physik, Universität Hamburg, 2007.

[29] A. Drynda, T. Hassel, R. Hoehn, A. Perz, F. W. Bach, and M. Peuster, *Development and biocompatibility of a novel corrodible fluoride-coated magnesium-calcium alloy with improved degradation kinetics and adequate mechanical properties for cardiovascular applications*, Journal of Biomedical Materials Research Part A, 93A (2010), pp. 763–775.

[30] T. Ebel, *Metal injection molding (MIM) of titanium and titanium alloys*, Handbook of Metal Injection Molding, (2012), pp. 415–445.

[31] J. Ellis, *The discovery of the gluon*, International Journal of Modern Physics A, 29 (2014).

[32] K. Emoto, H. Inadome, Y. Kanaho, S. Narumiya, and M. Umeda, *Local change in phospholipid composition at the cleavage furrow is essential for completion of cytokinesis*, Journal of Biological Chemistry, 280 (2005), pp. 37901–37907.

[33] L. A. Feldkamp, L. C. Davis, and J. W. Kress, *Practical Cone-Beam Algorithm*, Journal of the Optical Society of America A - Optics Image Science and Vision, 1 (1984), pp. 612–619.

[34] F. Feyerabend, H. Drucker, D. Laipple, C. Vogt, M. Stekker, N. Hort, and R. Willumeit, *Ion release from magnesium materials in physiological solutions under different oxygen tensions*, Journal of Materials Science-Materials in Medicine, 23 (2012), pp. 9–24.

[35] B. P. Flannery, H. W. Deckman, W. G. Roberge, and K. L. Damico, *3-Dimensional X-Ray Microtomography*, Science, 237 (1987), pp. 1439–1444.

[36] J. A. Gallagher, *Human osteoblast culture*, Methods Mol Med, 80 (2003), pp. 3–18.

[37] P. D. Garcia, R. Sapienza, A. Blanco, and C. Lopez, *Photonic glass: A novel random material for light*, Advanced Materials, 19 (2007), pp. 2597–+.

[38] P. D. Garcia, R. Sapienza, and C. Lopez, *Photonic Glasses: A Step Beyond White Paint*, Advanced Materials, 22 (2010), pp. 12–19.

[39] E. F. Garman and T. R. Schneider, *Macromolecular cryocrystallography*, Journal of Applied Crystallography, 30 (1997), pp. 211–237.

[40] R. Gerling, H. Clemens, and F. P. Schimansky, *Power metallurgical processing of intermetallic gamma titanium aluminides*, Advanced Engineering Materials, 6 (2004), pp. 23–38.

[41] N. Gey and M. Humbert, *Characterization of the variant selection occurring during the alpha ->beta ->alpha phase transformations of a cold rolled titanium sheet*, Acta Materialia, 50 (2002), pp. 277–287.

[42] L. A. Giannuzzi and F. A. Stevie, *Introduction to Focused Ion Beams*, Springer, 2005.

[43] R. Gordon, R. Bender, and G. T. Herman, *Algebraic Reconstruction Techniques (Art) for 3-Dimensional Electron Microscopy and X-Ray Photography*, Journal of Theoretical Biology, 29 (1970), pp. 471–&.

[44] R. Gosalawit-Utke, S. Meethom, C. Pistidda, C. Milanese, D. Laipple, T. Saisopa, A. Marini, T. Klassen, and M. Dornheim, *Destabilization of LiBH4 by nanoconfinement in PMMA-co-BM polymer matrix for reversible hydrogen storage*, International Journal of Hydrogen Energy, 39 (2014), pp. 5019–5029.

[45] R. Gosalawit-Utke, C. Milanese, P. Javadian, A. Girella, D. Laipple, J. Puszkiel, A. S. Cattaneo, C. Ferrara, J. Wittayakhun, J. Skibsted, T. R. Jensen, A. Marini, T. Klassen, and M. Dornheim, *2LiBH(4)-MgH2-0.13TiCl(4) confined in nanoporous structure of carbon aerogel scaffold for reversible hydrogen storage*, Journal of Alloys and Compounds, 599 (2014), pp. 78–86.

[46] R. Gosalawit-Utke, C. Milanese, P. Javadian, J. Jepsen, D. Laipple, F. Karmi, J. Puszkiel, T. R. Jensen, A. Marini, T. Klassen, and M. Dornheim, *Nanoconfined 2LiBH(4)-MgH2-TiCl3 in carbon aerogel scaffold for reversible hydrogen storage*, International Journal of Hydrogen Energy, 38 (2013), pp. 3275–3282.

[47] R. Gosalawit-Utke, T. K. Nielsen, I. Saldan, D. Laipple, Y. Cerenius, T. R. Jensen, T. Klassen, and M. Dornheim, *Nanoconfined 2LiBH(4)-MgH(2) Prepared by Direct Melt Infiltration into Nanoporous Materials*, Journal of Physical Chemistry C, 115 (2011), pp. 10903–10910.

[48] R. Gosalawit-Utke, T. K. Niesen, K. Pranzas, I. Saldan, C. Pistidda, F. Karimi, D. Laipple, J. Skibsted, T. R. Jensen, T. Klassen, and M. Dornheim, *2LiBH(4)-MgH2 in a Resorcinol-Furfural Carbon Aerogel Scaffold for Reversible Hydrogen Storage*, Journal of Physical Chemistry C, 116 (2012), pp. 1526–1534.

[49] L. Grodzins, *Optimum Energies for X-Ray Transmission Tomography of Small Samples - Applications of Synchrotron Radiation to Computerized-Tomography .1.*, Nuclear Instruments & Methods in Physics Research, 206 (1983), pp. 541–545.

[50] M. A. Groeber, B. K. Haley, M. D. Uchic, D. M. Dimiduk, and S. Ghosh, *3D reconstruction and characterization of polycrystalline microstructures using a FIB-SEM system*, Materials Characterization, 57 (2006), pp. 259–273.

[51] G. Guerriero, J. Fugelstad, and V. Bulone, *What Do We Really Know about Cellulose Biosynthesis in Higher Plants?*, Journal of Integrative Plant Biology, 52 (2010), pp. 161–175.

[52] A. Haibel, M. Ogurreck, F. Beckmann, T. Dose, F. Wilde, J. Herzen, M. Muller, A. Schreyer, V. Nazmov, M. Simon, A. Last, and J. Mohr, *Micro and Nano Tomography at the GKSS Imaging Beamline at PETRA III*, Developments in X-Ray Tomography Vii, 7804 (2010).

[53] U. Hecht, V. Witusiewicz, A. Drevermann, and J. Zollinger, *Grain refinement by low boron additions in niobium-rich TiAl-based alloys*, Intermetallics, 16 (2008), pp. 969–978.

[54] S. Heim, P. Guttmann, S. Rehbein, S. Werner, and G. Schneider, *Energy-tunable full-field x-ray microscopy: Cryo-tomography and nano-spectroscopy with the new BESSY TXM*, 9th International Conference on X-Ray Microscopy, 186 (2009).

[55] H. Hermawan, D. Dube, and D. Mantovani, *Developments in metallic biodegradable stents*, Acta Biomaterialia, 6 (2010), pp. 1693–1697.

[56] J. Herzen, *A grating interferometer for materials science imaging at a second-generation synchrotron radiation source*, PhD thesis; Department Physik, Universität Hamburg, 2010.

[57] J. Herzen, T. Donath, F. Pfeiffer, O. Bunk, C. Padeste, F. Beckmann, A. Schreyer, and C. David, *Quantitative phase-contrast tomography of a liquid phantom using a conventional x-ray tube source*, Optics Express, 17 (2009), pp. 10010–10018.

[58] P. W. Higgs, *Broken Symmetries, Massless Particles and Gauge Fields*, Physics Letters, 12 (1964), pp. 132–133.

[59] F. Hinterberger, *Physik der Teilchenbeschleuniger und Ionenoptik*, Springer, 2008.

[60] P. Hoffmeyer and R. B. Hanna, *Electron-Beam Damage during Testing of Wood in the Sem*, Wood Science and Technology, 23 (1989), pp. 211–214.

[61] L. Holzer, F. Indutnyi, P. H. Gasser, B. Munch, and M. Wegmann, *Three-dimensional analysis of porous BaTiO3 ceramics using FIB nanotomography*, Journal of Microscopy-Oxford, 216 (2004), pp. 84–95.

[62] L. Holzer, B. Muench, M. Wegmann, P. Gasser, and R. J. Flatt, *FIB-Nanotomography of particulate systems - Part I: Particle shape and topology of interfaces*, Journal of the American Ceramic Society, 89 (2006), pp. 2577–2585.

[63] G. N. Hounsfield, *Computerized transversial axial scanning (tomography): Part i. description of system.*, British Journal of Radiology, 46 (1973), pp. 1016–1022.

[64] T. Ishitani, H. Koike, T. Yaguchi, and T. Kamino, *Implanted gallium ion concentrations of focused-ion-beam prepared cross sections*, Journal of Vacuum Science & Technology B, 16 (1998), pp. 1907–1913.

[65] T. Ishitani, K. Umemura, T. Ohnishi, T. Yaguchi, and T. Kamino, *Improvements in performance of focused ion beam cross-sectioning: aspects of ion-sample interaction*, Journal of Electron Microscopy, 53 (2004), pp. 443–449.

[66] D. Iwanenko and I. Pomeranchuk, *On the maximal energy attainable in a betatron*, Phys. Rev., 65 (1944), p. 343.

[67] J. Jean do Rosario, *private communication*, Technical University Hamburg-Harburg, Institute of ceramic high-performance materials, (2013).

[68] A. C. Jones, C. H. Arns, A. P. Sheppard, D. W. Hutmacher, B. K. Milthorpe, and M. A. Knackstedt, *Assessment of bone ingrowth into porous biomaterials using MICRO-CT*, Biomaterials, 28 (2007), pp. 2491–2504.

[69] A. C. Kak and M. Slaney, *Principles of Computerized Tomography*, IEEE Press, New York, 1987.

[70] N. I. Kato, *Reducing focused ion beam damage to transmission electron microscopy samples*, Journal of Electron Microscopy, 53 (2004), pp. 451–458.

[71] K. Kölln, *Morphologie und mechanische Eigenschaften von Zellulosefasern - Untersuchung mit Röntgen- und Neutronenstreuung*, PhD thesis; Institut für Experimentelle und Angewandte Physik, Christian-Albrechts-Universität zu Kiel, 2004.

[72] M. Knoll, *Charge potential and secondary emissions of electron irradiated bodies*, Physikalische Zeitschrift, 36 (1935), pp. 861–869.

[73] M. Knoll and E. Ruska, *The Electron Microscope*, Zeitschrift Fur Physik, 78 (1932), pp. 318–339.

[74] A. Kochanowski, A. Hoene, M. Patrzyk, U. Walschus, B. Finke, B. Luthringer, F. Feyerabend, R. Willumeit, S. Lucke, and M. Schlosser, *Examination of the inflammatory response following implantation of titanium plates coated with phospholipids in rats*, Journal of Materials Science-Materials in Medicine, 22 (2011), pp. 1015–1026.

[75] W. Kurz and D. J. Fisher, *Fundamentals of Solidification*, Trans Tech Publications, 1986.

[76] J. Larmor, *On the theory of the magnetic influence on spectra; and on the radiation of moving ions*, Phil. Mag., 44 (1897), pp. 503–512.

[77] P. Lenard, *Über Kathodenstrahlen in Gasen von atmosphärischem Druck und im äußeren Vacuum*, Annalen der Physik und Chemie, 51 (1894), pp. 225–267.

[78] B. Lengeler, C. Schroer, J. Tummler, B. Benner, M. Richwin, A. Snigirev, I. Snigireva, and M. Drakopoulos, *Imaging by parabolic refractive lenses in the hard X-ray range*, Journal of Synchrotron Radiation, 6 (1999), pp. 1153–1167.

[79] B. Lengeler, J. Tummler, A. Snigirev, I. Snigireva, and C. Raven, *Transmission and gain of singly and doubly focusing refractive x-ray lenses*, Journal of Applied Physics, 84 (1998), pp. 5855–5861.

[80] K. Leppanen, S. Andersson, M. Torkkeli, M. Knaapila, N. Kotelnikova, and R. Serimaa, *Structure of cellulose and microcrystalline cellulose from various wood species, cotton and flax studied by X-ray scattering*, Cellulose, 16 (2009), pp. 999–1015.

[81] W. C. Li, A. H. Lu, C. Weidenthaler, and F. Schuth, *Hard-templating pathway to create mesoporous magnesium oxide*, Chemistry of Materials, 16 (2004), pp. 5676–5681.

[82] H. Lichtenegger, M. Muller, O. Paris, C. Riekel, and P. Fratzl, *Imaging of the helical arrangement of cellulose fibrils in wood by synchrotron X-ray microdiffraction*, Journal of Applied Crystallography, 32 (1999), pp. 1127–1133.

[83] A. Liénard, *Champ électrique et magnétique, produit par une charge électrique concentrée en un point et animée d'un mouvement quelconque*, L'Éclairage Élec., 16 (1898), pp. 5–14, 53–59, 106–112.

[84] N. C. Lindquist, P. Nagpal, K. M. McPeak, D. J. Norris, and S. H. Oh, *Engineering metallic nanostructures for plasmonics and nanophotonics*, Reports on Progress in Physics, 75 (2012).

[85] Y. C. Liu, G. C. Yang, and Y. H. Zhou, *High-velocity banding structure in the laser-resolidified hypoperitectic Ti47Al53 alloy*, Journal of Crystal Growth, 240 (2002), pp. 603–610.

[86] J. J. Lombardo, R. A. Ristau, W. M. Harris, and W. K. S. Chiu, *Focused ion beam preparation of samples for X-ray nanotomography*, Journal of Synchrotron Radiation, 19 (2012), pp. 789–796.

[87] G. Margaritondo, *Introduction to Synchrotron Radiation*, Oxford University Press, 1988.

[88] M. Mastrogiacomo, S. Scaglione, R. Martinetti, L. Dolcini, F. Beltrame, R. Cancedda, and R. Quarto, *Role of scaffold internal structure on in vivo bone formation in macroporous calcium phosphate bioceramics*, Biomaterials, 27 (2006), pp. 3230–3237.

[89] T. L. Matteson, S. W. Schwarz, E. C. Houge, B. W. Kempshall, and L. A. Giannuzzi, *Electron backscattering diffraction investigation of focused ion beam surfaces*, Journal of Electronic Materials, 31 (2002), pp. 33–39.

[90] C. Mccullough, J. J. Valencia, C. G. Levi, and R. Mehrabian, *Microstructural Analysis of Rapidly Solidified Ti-Al-X Powders*, Materials Science and Engineering a-Structural Materials Properties Microstructure and Processing, 124 (1990), pp. 83–101.

[91] D. McMullan, *Investigations relating to the design of electron microscopes*, PhD thesis, University of Cambridge, 1952.

[92] D. Mcmullan, J. Thewlis, A. W. Agar, D. Gabor, M. E. Haine, H. G. Lubszynski, R. Feinberg, and D. Mcmullan, *An Improved Scanning Electron Microscope for Opaque Specimens*, Proceedings of the Institution of Electrical Engineers-London, 100 (1953), pp. 245–259.

[93] MiNaXS-beamline, *photon-science.desy.de/facilities/petra_iii/beamlines/p03_ minaxs/index_eng.html*, (accessed Januar 8, 2015).

[94] A. Momose, *Phase-contrast X-ray imaging based on interferometry*, Journal of Synchrotron Radiation, 9 (2002), pp. 136–142.

[95] A. Momose, *Recent advances in X-ray phase imaging*, Japanese Journal of Applied Physics Part 1-Regular Papers Brief Communications & Review Papers, 44 (2005), pp. 6355–6367.

[96] B. Munch, P. Gasser, L. Holzer, and R. Flatt, *FIB-nanotomography of particulate systems - Part II: Particle recognition and effect of boundary truncation*, Journal of the American Ceramic Society, 89 (2006), pp. 2586–2595.

[97] F. Natterer, *The Mathematics of Computerized Tomography*, Soc. for Industrial & Applied Math, 2001.

[98] V. Nazmov, E. Reznikova, J. Mohr, V. Saile, L. Vincze, B. Vekemans, S. Bohic, and A. Somogyi, *Parabolic crossed planar polymeric x-ray lenses*, Journal of Micromechanics and Microengineering, 21 (2011).

[99] D. E. Newbury and D. B. Williams, *The electron microscope: The materials characterization tool of the millennium*, Acta Materialia, 48 (2000), pp. 323–346.

[100] Y. Nishiyama, *Structure and properties of the cellulose microfibril*, Journal of Wood Science, 55 (2009), pp. 241–249.

[101] Y. Nishiyama, J. Sugiyama, H. Chanzy, and P. Langan, *Crystal structure and hydrogen bonding system in cellulose 1(alpha), from synchrotron X-ray and neutron fiber diffraction*, Journal of the American Chemical Society, 125 (2003), pp. 14300–14306.

[102] C. W. Oatley, D. Mcmullan, and K. C. A. Smith, *The Development of the Scanning Electron-Microscope*, Advances in Imaging and Electron Physics, (1985), pp. 443–482.

[103] N. I. of Standards and Technology, *XCOM: Photon Cross Sections Database*, http://www.nist.gov/pml/data/xcom/index.cfm, (accessed September 23, 2014).

[104] M. Ogurreck, *Development and Implementation of a Nanotomography Setup at the PETRA III Beamline P05*, PhD thesis; Institut für Experimentelle und Angewandte Physik, Christian-Albrechts-Universität zu Kiel, 2014.

[105] O. Paris and M. Muller, *Scanning X-ray microdiffraction of complex materials: Diffraction geometry considerations*, Nuclear Instruments & Methods in Physics Research Section B-Beam Interactions with Materials and Atoms, 200 (2003), pp. 390–396.

[106] C. Pascual Garcia, A. D. Burchardt, R. N. Carvalho, D. Gilliland, C. A. D, F. Rossi, and T. Lettieri, *Detection of Silver Nanoparticles inside Marine Diatom Thalassiosira pseudonana by Electron Microscopy and Focused Ion Beam*, PLoS One, 9 (2014), p. e96078.

[107] M. Peura, M. Muller, U. Vainio, M. P. Saren, P. Saranpaa, and R. Serimaa, *X-ray microdiffraction reveals the orientation of cellulose microfibrils and the size of cellulose crystallites in single Norway spruce tracheids*, Trees-Structure and Function, 22 (2008), pp. 49–61.

[108] J. L. Provis, V. Rose, R. P. Winarski, and J. S. J. van Deventer, *Hard X-ray nanotomography of amorphous aluminosilicate cements*, Scripta Materialia, 65 (2011), pp. 316–319.

[109] J. Radon, *Über die Bestimmung von Funktionen durch ihre Integralwerte längs gewisser Mannigfaltigkeiten*, Berichte über die Verhandlungen der Königlich-Sächsischen Gesellschaft der Wissenschaften zu Leipzig Mathematisch-Physische Klasse, 69 (1917), pp. 262–277.

[110] J. Rehacek, Z. Hradil, M. Zawisky, W. Treimer, and M. Strobl, *Maximum-likelihood absorption tomography*, Europhysics Letters, 59 (2002), pp. 694–700.

[111] L. Reimer and G. Pfefferkorn, *Rasterelektronenmikroskopie*, Springer Verlag, 1973.

[112] W. Reimers, A. R. Pyzalla, A. Schreyer, and H. Clemens, *Neutrons and Synchrotron Radiation in Engineering Materials Science*, Wiley-VCH, 2008.

[113] F.-P. Schimansky, G. Müllauer, and R. Gerling, *Maßnahmen zur Erzielung großer Abkühlgeschwindigkeiten und kurzer Erstarrungszeiten in der Pulvermetallurgie*, GKSS-Forschungszentrum Geesthacht GmbH, 1993.

[114] L. Schlapbach and A. Zuttel, *Hydrogen-storage materials for mobile applications*, Nature, 414 (2001), pp. 353–358.

[115] G. Schneider, P. Guttmann, S. Heim, S. Rehbein, D. Eichert, and B. Niemann, *X-ray microscopy at BESSY: From nano-tomography to fs-imaging*, Synchrotron Radiation Instrumentation, Pts 1 and 2, 879 (2007), pp. 1291–1294.

[116] G. A. Schott, *On the radiation from groups of electrons*, Ann. Phys., 329 (1907), pp. 635–660.

[117] C. G. Schroer, O. Kurapova, J. Patommel, P. Boye, J. Feldkamp, B. Lengeler, M. Burghammer, C. Riekel, L. Vincze, A. van der Hart, and M. Kuchler, *Hard x-ray nanoprobe based on refractive x-ray lenses*, Applied Physics Letters, 87 (2005).

[118] C. G. Schroer and B. Lengeler, *Focusing hard X rays to nanometer dimensions by adiabatically focusing lenses*, Physical Review Letters, 94 (2005).

[119] H. Schumann and H. Oettel, *Metallographie*, Wiley-VCH, 2005.

[120] A. J. Schwartz, M. Kumar, and B. L. Adams, *Electron Backscatter Diffraction in Materials Science*, Kluwer Academic/Plenum Publishers, 2000.

[121] H. Seiler, Zeitschrift für Angewandte Physik, 22 (1967), p. 249.

[122] SFB-986, *www.tuhh.de/sfb986/home.html*, (accessed October 2, 2014), (2014).

[123] K. C. A. Smith, B. C. Breton, N. H. M. Caldwell, and D. McMullan, *IX. Bibliography of Scanning Electron Microscopy, cued, 1951-*, http://www2.eng.cam.ac.uk/ bcb/bibweb1.htm, (accessed March 21, 2013).

[124] K. C. A. Smith and C. W. Oatley, *The Scanning Electron Microscope and Its Fields of Application*, British Journal of Applied Physics, 6 (1955), pp. 391–399.

[125] E. D. Spoerke, N. G. Murray, H. L. Li, L. C. Brinson, D. C. Dunand, and S. I. Stupp, *A bioactive titanium foam scaffold for bone repair*, Acta Biomater, 1 (2005), pp. 523–533.

[126] A. Stark, *private communication*, Helmholtz-Zentrum Geesthacht, Institute of metal physics, (2015).

[127] S. Storm, *Strukturbestimmung an natürlicher Zellulose mit Synchrotron-Strahlung*, Master thesis; Institut für Experimentelle und Angewandte Physik, Christian-Albrechts-Universität Kiel, 2012.

[128] S. Storm, M. Ogurreck, D. Laipple, C. Krywka, M. Burghammer, E. Di Cola, and M. Muller, *On radiation damage in FIB-prepared softwood samples measured by scanning X-ray diffraction*, J Synchrotron Radiat, 22 (2015), pp. 267–72.

[129] M. Störmer, C. Michaelsen, J. Wiesmann, P. Ricardo, and R. Bormann, *The Dekker Encyclopedia of Nanoscience and Nanotechnology*, Marcel Dekker Inc., New York, 2006.

[130] M. Sugiyama and G. Sigesato, *A review of focused ion beam technology and its applications in transmission electron microscopy*, Journal of Electron Microscopy, 53 (2004), pp. 527–536.

[131] G. Taylor, *Disintegration of Water Drops in Electric Field*, Proceedings of the Royal Society of London Series A - Mathematical and Physical Sciences, 280 (1964), pp. 383–+.

[132] D. Tie, F. Feyerabend, N. Hort, R. Willumeit, and D. Hoeche, *XPS Studies of Magnesium Surfaces after Exposure to Dulbecco's Modified Eagle Medium, Hank's Buffered Salt Solution, and Simulated Body Fluid*, Advanced Engineering Materials, 12 (2010), pp. B699–B704.

[133] J. J. Valencia, C. Mccullough, C. G. Levi, and R. Mehrabian, *Solidification Microstructure of Supercooled Ti-Al Alloys Containing Intermetallic Phases*, Acta Metallurgica, 37 (1989), pp. 2517–2530.

[134] G. Wang, T. H. Lin, P. C. Cheng, and D. M. Shinozaki, *A General Cone-Beam Reconstruction Algorithm*, Ieee Transactions on Medical Imaging, 12 (1993), pp. 486–496.

[135] E. A. Wargo, T. Kotaka, Y. Tabuchi, and E. C. Kumbur, *Comparison of focused ion beam versus nano-scale X-ray computed tomography for resolving 3-D microstructures of porous fuel cell materials*, Journal of Power Sources, 241 (2013), pp. 608–618.

[136] O. C. Wells, *The construction of a scanning electron microscope and its application to the study of fibres*, PhD thesis, University of Cambridge, 1957.

[137] K. Wille, *Physik der Teilchenbeschleuniger und Synchrotronstrahlungsquellen*, Teubner, 1992.

[138] R. Willumeit, J. Fischer, F. Feyerabend, N. Hort, U. Bismayer, S. Heidrich, and B. Mihailova, *Chemical surface alteration of biodegradable magnesium exposed to corrosion media*, Acta Biomaterialia, 7 (2011), pp. 2704–2715.

[139] R. Willumeit, M. Schossig, H. Clemens, and F. Feyerabend, *In-vitro interactions of human chondrocytes and mesenchymal stem cells, and of mouse macrophages with phospholipid-covered metallic implant materials*, European Cells & Materials, 13 (2007), pp. 11–24.

[140] R. Willumeit, A. Schuster, P. Iliev, S. Linser, and F. Feyerabend, *Phospholipids as implant coatings*, Journal of Materials Science-Materials in Medicine, 18 (2007), pp. 367–380.

[141] R. P. Winarski, M. V. Holt, V. Rose, P. Fuesz, D. Carbaugh, C. Benson, D. M. Shu, D. Kline, G. B. Stephenson, I. McNulty, and J. Maser, *A hard X-ray nanoprobe beamline for nanoscale microscopy*, Journal of Synchrotron Radiation, 19 (2012), pp. 1056–1060.

[142] F. Witte, *The history of biodegradable magnesium implants: A review*, Acta Biomaterialia, 6 (2010), pp. 1680–1692.

[143] V. T. Witusiewicz, A. A. Bondar, U. Hecht, and T. Y. Velikanova, *The Al-B-Nb-Ti system. IV. Experimental study and thermodynamic re-evaluation of the binary Al-Nb and ternary Al-Nb-Ti systems*, Journal of Alloys and Compounds, 472 (2009), pp. 133–161.

[144] L. Yang, N. Hort, D. Laipple, D. Hoche, Y. Huang, K. U. Kainer, R. Willumeit, and F. Feyerabend, *Element distribution in the corrosion layer*

*and cytotoxicity of alloy Mg-10Dy during in vitro biodegradation*, Acta Biomater, (2012).

[145] L. Yang, Y. D. Huang, Q. M. Peng, F. Feyerabend, K. U. Kainer, R. Willumeit, and N. Hort, *Mechanical and corrosion properties of binary Mg-Dy alloys for medical applications*, Materials Science and Engineering B-Advanced Functional Solid-State Materials, 176 (2011), pp. 1827–1834.

[146] Zeiss, *Instruction manual AURIGA*, Carl Zeiss NTS GmbH, Oberkochen, Germany, 2009.

[147] Zeiss, *Instruction manual Zeiss multi GIS*, Carl Zeiss NTS GmbH, Oberkochen, Germany, 2009.

[148] E. Zolotoyabko, *Basic Concepts of X-Ray Diffraction*, Wiley-VCH, 2014.

# List of cooperated publications

A. Deing, B. Luthringer, D. Laipple, T. Ebel and R. Willumeit, *A Porous TiAl6V4 Implant Material for Medical Application*, Int J Biomater, (2014).
[25] (Refer to chapter 4)

F. Feyerabend, H. Drucker, D. Laipple, C. Vogt, M. Stekker, N. Hort, and R. Willumeit, *Ion release from magnesium materials in physiological solutions under different oxygen tensions*, Journal of Materials Science-Materials in Medicine, 23 (2012), pp. 9-24.
[34] (Refer to section 5.1)

R. Gosalawit-Utke, S. Meethom, C. Pistidda, C. Milanese, D. Laipple, T. Saisopa, A. Marini, T. Klassen, M. Dornheim, *Destabilization of LiBH4 by nanoconfinement in PMMA-co-BM polymer matrix for reversible hydrogen storage*, International Journal of Hydrogen Energy, 39 (2014), pp. 5019-5029.
[44] (Refer to chapter 6)

R. Gosalawit-Utke, C. Milanese, P. Javadian, A. Girella, D. Laipple, J. Puszkiel, A. S. Cattaneo, C. Ferrara, J. Wittayakhun, J. Skibsted, T. R. Jensen, A. Marini, T. Klassen, M. Dornheim, *2LiBH(4)-MgH2-0.13TiCl(4) confined in nanoporous structure of carbon aerogel scaffold for reversible hydrogen storage*, Journal of Alloys and Compounds, 599 (2014), pp. 78-86.
[45] (Refer to chapter 6)

R. Gosalawit-Utke, C. Milanese, P. Javadian, J. Jepsen, D. Laipple, F. Karmi, J. Puszkiel, T. R. and Jensen, A. Marini, T. Klassen, M. Dornheim, *Nanoconfined 2LiBH(4)-MgH2-TiCl3 in carbon aerogel scaffold for reversible hydrogen storage*, International Journal of Hydrogen Energy, 38 (2013), pp. 3275-3282.
[46] (Refer to chapter 6)

R. Gosalawit-Utke, T. K. Nielsen, I. Saldan, D. Laipple, Y. Cerenius, T. R. Jensen, T. Klassen, and M. Dornheim, *Nanoconfined 2LiBH(4)-MgH(2) Prepared by Direct Melt Infiltration into Nanoporous Materials*, Journal of Physical Chemistry C, 115 (2011), pp. 10903-10910.
[47] (Refer to chapter 6)

R. Gosalawit-Utke, T. K. Nielsen, K. Pranzas, I. Saldan, C. Pistidda, F. Karimi, D. Laipple, J. Skibsted, T. R. Jensen, T. Klassen, and M. Dornheim, *2LiBH(4)-MgH(2) in a Resorcinol-Furfural Carbon Aerogel Scaffold for Reversible Hydrogen Storage*, Journal of Physical Chemistry C, 116 (2012), pp. 1526-1534.
[48] (Refer to chapter 6)

S. Storm, M. Ogurreck, D. Laipple, C. Krywka, M. Burghammer, E. Di Cola, M. Muller, *On radiation damage in FIB-prepared softwood samples measured by scanning X-ray diffraction*, J Synchrotron Radiat, 22 (2015), pp. 267-272.
[128] (Refer to chapter 8)

L. Yang, N. Hort, D. Laipple, D. Hoche, Y. Huang, K. U. Kainer, R. Willumeit, and F. Feyerabend, *Element distribution in the corrosion layer and cytotoxicity of alloy Mg-10Dy during in vitro biodegradation*, Acta Biomater, 9 (2012), pp. 8475-8487.
[144] (Refer to section 5.2)

**Conferences**

D. Laipple, B. Luthringer, A. Deing, R. Willumeit, A. Schreyer, *Osteoblast-like cell ingrowth assessment by means of SEM techniques & Tomography*, **Poster**, Neue Horizonte für metallische Biomaterialien, Geesthacht (2011).
(Refer to chapter 4)

D. Laipple, B. Luthringer, A. Deing, T. Ebel, R. Willumeit, A. Schreyer, *Osteoblast-like cell ingrowth assessment by means of SEM techniques*, **Talk**, European Cross-Beam User Meeting, Stuttgart (2012).
(Refer to chapter 4)

D. Laipple, B. Luthringer, A. Deing, T. Ebel, R. Willumeit, A. Schreyer, *Localisation of cells in a porous Ti alloy by SEM techniques*, **Talk**, PNI[1] in-house research: 2nd Soft Matter & Life Science Workshop, Potsdam (2012).
(Refer to chapter 4)

D. Laipple, B. Luthringer, A. Deing, T. Ebel, R. Willumeit, A. Schreyer, *Localisation of cells in a porous Ti alloy by SEM techniques*, **Oral-Poster**, Materials Science and Engineering Conference (MSE), Darmstadt (2012).
(Refer to chapter 4)

[1]PNI = Photons, Neutrons and Ions

## Acknowledgement / Danksagung

Ich möchte hier meinen besonderen Dank aussprechen, bei meinem Betreuer Prof. Dr. Andreas Schreyer sowie bei meinem Abteilungsleiter Prof. Dr. Martin Müller für das interessante und vielseitige Thema meiner Doktorarbeit im Helmholtz-Zentrum Geesthacht sowie die gute Zusammenarbeit. Außerdem möchte ich mich bei Prof. Dr. Florian Pyczak bedanken, der mit seiner Abteilung WPM der Auriga einen Raum gab bis das EMSC[2] einmal am DESY steht, für alle Hilfen und Ideen zum Thema und das freundliche Arbeitsklima.
Weiterhin danke ich Prof. Dr. Regine Willumeit-Römer, die mit den biologischen Proben und Fragestellungen den ersten praktischen Teil dieser Arbeit maßgeblich motivierte. Bérengère Luthringer und Axel Deing gilt mein besonderer Dank für das Vorbereiten der Implantatwerkstoffe und die belebenden Gespräche. Mein Dank gilt hier auch Gabriele Salomon, die im Wesentlichen die umfangreiche Zellpräparation für diese Proben durchführte.
Frank Feyerabend und Lei Yang danke ich für die freundliche und fruchtbare Zusammenarbeit im Themenbereich abbaubarer Implantate, sowie Rapee Gosalawit-Utke im Bereich der Wasserstoffspeichermaterialien. Die ersten gemeinsamen Veröffentlichungen waren eine gute Motivation.
Bei Malte Ogurreck möchte ich mich für die Röntgentomographien und die prima Zusammenarbeit insgesamt bedanken. Vor allem aber auch dafür das zur Fertigstellung unserer beider Arbeiten schlussendlich die finale Nanotomographie gelang!
Ich danke Uwe Lorenz für die erstklassige freundschaftliche Betreuung und Unterstützung bei allen Fragen und Problemen rund um die Elektronenmikroskopie, sowie Selina Storm und Christina Krywka für die erfolgreiche Zusammenarbeit bezüglich der Holzproben und der Nanodiffraktion.
Bernd Schwebke danke ich für die Hilfe bei der Durchführung der Diffraktion an den Pulverfraktionen sowie Marcus Rackel für die Tips bei der Auswertung. Michael Oehring, Andreas Stark und Frank-Peter Schimansky danke ich diesbezüglich für die hilfreichen Diskussionen zur Interpretation der Messergebinsse.
Mein Dank gilt auch allen weiteren Kollegen in Geesthacht und an der Außenstelle am DESY die mir in freundschaftlicher Atmosphäre halfen und mich unterstützten!
Ganz besonders möchte ich meiner Familie danken, meiner Frau Marina, meinen Mädels Cecilia, Leora, Nediva und seit über einem Jahr auch dem kleinen Arkin, dass ihr hinter mir standet und mich unterstützt habt und ihr zu guter Letzt dank Gottes Liebe ein Teil meines Lebens seid!

[2]Engineering Materials Science Centre